Crystallographic Orientation-Dependent Performance of InGaN Blue Laser

By

Sourav Roy

A thesis submitted in partial fulfillment of the requirements for the degree of
Master of Engineering
in Electrical & Electronic Engineering

Khulna University of Engineering & Technology
Khulna 9203, Bangladesh
December 2017

Declaration

This is to certify that the thesis work entitled *"Crystallographic Orientation-Dependent Performance of InGaN Blue Laser"* has been carried out by *Sourav Roy* in the Department of *Electrical & Electronic Engineering*, Khulna University of Engineering & Technology, Khulna, Bangladesh. The above thesis work or any part of this work has not been submitted anywhere for the award of any degree or diploma.

Supervised By:
Dr. Md. Rafiqul Islam
Professor, Dept. of EEE, KUET

Submitted By:
Sourav Roy
Roll: 1503564

Signature of Supervisor

Signature of Candidate

December, 2017

Khulna University of Engineering and Technology (KUET)

Approval

This is to certify that the thesis work submitted by *Sourav Roy* entitled " *Crystallographic Orientation-Dependent Performance of InGaN Blue Laser*" has been approved by the board of examiners for the partial fulfillment of the requirements for the degree of *Master of Engineering* in the Department of *Electrical & Electronic Engineering*, Khulna University of Engineering & Technology, Khulna, Bangladesh in December, 2017.

BOARD OF EXAMINERS

1. ___________________ Chairman (Supervisor)
   Dr. Md. Rafiqul Islam
   Professor
   Department of Electrical & Electronic Engineering
   Khulna University of Engineering & Technology

2. ___________________ Member
   Head of the Department
   Department of Electrical & Electronic Engineering
   Khulna University of Engineering & Technology

3. ___________________ Member
   Dr. Ashraful Ghani Bhuiyan
   Professor
   Department of Electrical and Electronic Engineering
   Khulna University of Engineering & Technology

4. ___________________ Member
   Dr. Md. Mahbub Hasan
   Associate Professor
   Department of Electrical and Electronic Engineering
   Khulna University of Engineering & Technology

5. ___________________ Member (External)
   Dr. Anisul Haque
   Professor
   Department of Electrical and Electronic Engineering
   East West University

ACKNOWLEDGEMENT

I would like to express my deepest gratitude to my supervisor and motivator **Dr. Md. Rafiqul Islam,** Professor, Department of Electrical & Electronic Engineering, Khulna University of Engineering & Technology, Khulna for his constant inspiration, valuable guidance and kind co-operation and finally helping me for providing necessary materials and sources during the entire period of my research work.

I would also like to thank **Dr**. **Md. Tanvir Hasan**, Assistant Professor, Department of Electrical & Electronic Engineering, Jessore University of Science & Technology, Bangladesh, for his valuable suggestions on this thesis report.

Last but not the least; I would like to thank the authors of various research articles and books that are referred to.

ABSTRACT

This thesis attempts to address a comprehensive in-depth study on the crystal orientation and strain-dependent optoelectronic performance and frequency response of 445nm InGaN/GaN single quantum well (QW) Blue Laser operating at 300K by solving a six-band **k.p** Hamiltonian at the Brillouin zone center point using finite difference method. Here 8nm $In_{0.17}Ga_{0.83}N$ is used in the active layer and 10nm GaN is used in the guiding/barrier layer. The well is compressively strained due to lattice mismatch between well and barrier layer. The simulation is carried out in MATLAB/Simulink environment along (0001), $(10\bar{1}0)$, $(10\bar{1}2)$, $(11\bar{2}2)$ and $(10\bar{1}1)$ crystal orientations. Tensor rotation scheme is applied to modify the wave vector and Hamiltonian matrix from conventional (0001) crystal orientation. The compositions of well materials are selected as $In_{0.15}Ga_{0.85}N$, $In_{0.17}Ga_{0.83}N$, $In_{0.19}Ga_{0.81}N$ and $In_{0.21}Ga_{0.79}N$ for strain-dependent performance analysis along $(11\bar{2}2)$, $(10\bar{1}2)$ and (0001) crystal orientation. In crystal orientation-dependent analysis for 17% Indium composition, it is found that there is a substantial correlation of the energy band dispersion profile, momentum matrix, piezoelectric (PZ) field, peak gain and peak emission wavelength with change of crystal orientation. The PZ field is found to be zero in $(11\bar{2}2)$ and $(10\bar{1}0)$ crystal orientation (growth angle of 58.4° and 90° w.r.t z-axis). The optical gains are inspected as 3845, 4460, 4880, 4750 and 4178 cm^{-1} corresponding to peak emission wavelength of 447, 455, 446, 441 and 438nm at (0001), $(10\bar{1}2)$, $(11\bar{2}2)$, $(10\bar{1}1)$ and $(10\bar{1}0)$ orientations when the injection carrier density is of 3.5×10^{19} cm^{-3}. Moreover, the optical gain in $(11\bar{2}2)$ orientation is always higher than other orientation in any injection carrier density. During compressive strain-dependent performance evaluation, significant amount of optical gain and emission wavelength variations are found for the value of In composition from 15% to 21%. For example, in $(11\bar{2}2)$-oriented QW; optical gain changes from 4730 to 5190 cm^{-1} with a corresponding emission wavelength shifting from 452 to 430 nm for changing the indium composition from 15% to 21%. Output optical power characteristics are analyzed by developing a Simulink model with the help of 2-level rate equations and following the concept of signal-flow diagram. In $(11\bar{2}2)$, $(10\bar{1}2)$ and (0001)-oriented structure, higher optical power is found when the indium composition is 21%

in the active region. Among arbitrary crystal orientated structure, maximum optical power of 4.35mW and minimum threshold current of 0.74mA is obtained in $(11\bar{2}2)$ crystal orientation. A state-space model is formed for each (hkil)-orientated crystal structure in order to observe their frequency responses (Bode Plot) close to corner frequencies. The laser system for each orientation and indium composition is found to be stable as positive gain and phase margin is achieved. Highest magnitude (dB) response is obtained in semipolar $(11\bar{2}2)$ crystal orientation for 21% indium composition in well. This numerical result demonstrates that semipolar $(11\bar{2}2)$ crystal orientation is of special interest and can be incorporated into the active layer of blue laser in order to have best performance for high-speed lightwave communication technologies which can be used for medical & industrial purpose, precision measurement, military defence & security, thermal imaging, DVD and Blu-ray players etc.

Contents

	Title Page	i
	Declaration	ii
	Certificate of Research	iii
	Acknowledgement	iv
	Abstract	v
	Contents	vii
	List of Symbols	ix
	List of Tables	x
	List of Figures	xi
CHAPTER I	**Introduction**	
	1.1 Background of the Thesis	1
	1.1.1 Prospect of III-N Material for Optical Devices	2
	1.1.2 Significance of InGaN-based Blue Laser	2
	1.2 Present status of InGaN-based Blue Laser	3
	1.3 Research Motivation	4
	1.4 Specific Objectives	8
	1.5 Organization of This Thesis	9
CHAPTER II	**Fundamental Concepts of the Research**	
	2.1 Brief Overview on Semiconductor Laser	10
	2.1.1 Laser Types	11
	2.1.2 Application	12
	2.2 Basic Physics of QW Laser	12
	2.2.1 Quantum Well	12
	2.2.2 Density of States	14
	2.2.3 Electron Transition Mechanism	14
	2.2.4 Electron Transition Strength	16
	2.2.5 Lasing Condition	17
	2.2.6 Output Power	17
	2.3 Laser Cavities and Laser Cavity Modes	18
	2.3.1 Longitudinal modes in the laser cavity	18
	2.3.2 Waveguide modes	19
	2.3.3 Confinement factor	19
CHAPTER III	**Properties of InGaN Material**	
	3.1 Brief History on InGaN Development	20

3.2 Structural Properties of InGaN 22
3.2.1 Crystal Structure 22
3.2.2 Polarization Properties 25
3.3 Optical Properties of InGaN 26
3.3.1 Energy bandgap and refractive index 26
3.3.2 Strain induced QCSE 29
3.4 Electrical Properties of InGaN 32
3.4.1 n-type Doping 32
3.4.2 p-type Doping 33
3.4.3 p-n Junction 33
3.5 Overview on Polar, Non-polar and Semipolar Orientation 36

CHAPTER IV Proposed Laser Structure and Mathematical Model
4.1 Proposed QW Blue LD Structure 39
4.2 Modeling of Electronic Energy Bands 44
4.2.1 Conduction Band Dispersion Profile 40
4.2.2 Valence Band Dispersion Profile 42
4.2.3 Orientation-dependent Energy Band 44
4.2.4 Energy Band change due to Piezoelectric Field 46
4.3 Momentum Matrix Element and Optical Gain Profile 47
4.4 Output Power Characteristics 49
4.5 Frequency Response Analysis 53

CHAPTER V Simulation Results and Discussion
5.1 Crystal Orientation-dependent Strain and Polarization field 56
5.2 Energy Band Dispersion Profile in (hkil) Orientation 58
5.3 Momentum Matrix in (hkil) Orientation 60
5.4 Optical Emission Profile in (hkil) Orientation 62
5.5 Output Power Characteristics in (hkil) Orientation 64
5.6 Frequency Response Analysis in (hkil) Orientation 66
5.7 Model Verification 67
5.8 Strain-dependent Optoelectronic Performance in $(11\bar{2}2)$ Crystal Orientation 68

CHAPTER VI Conclusion
6.1 Contributions 74
6.2 Future Work 76

REFERENCES 77

LIST OF SYMBOLS

Symbol	Description
$\Psi(x)$	Wave function
H	Hamiltonian Matrix
ε_{ij}	Principal strain components
Δv_e	Conduction band offset
m_*^e	Electron effective mass
u_{nk}	Eigen Function
E_g	Energy Gap
k_t	Inplane wave vector
O_R	Rotation Matrix
$\hbar$	Reduced Plank Constant
θ	Growth angle
(hkil)	Miller Indices
η_i	Current-injection efficiency
N_W	No. of QW
V_{act}	Volume of one QW
Γ_c	Optical confinement factor (mean value)
η_c	Output power coupling coefficient
A_W	QW Unimolecular recombination rate coefficient
C_W	Auger recombination rate coefficient
A_b	SCH unimolecular recombination rate coefficient
ε	Phenomenological gain-saturation term
β_A	Unimolecular recombination coupling term
β_B	Radiative recombination coupling term
β_C	Auger recombination coupling term
V_{barr}	Volume of SCH
τ_{cap}	QW capture lifetime
τ_{em}	QW emission lifetime
L_c	Cavity length

LIST OF TABLES

Table No	Description	Page
1.1	Performance of InGaN/GaN-based lasers on c-plane GaN substrates	4
1.2	Recent development of InGaN/GaN-based lasers on m-plane GaN substrates	5
1.3	Recent development of InGaN/GaN-based laser on semipolar GaN substrates	6
4.1	Material parameters used for evaluating output optical power characteristics	51
4.2	Crystal orientation-dependent parameters from the rate equations	52
5.1	Material Parameters for Blue Laser	55
5.2	Orientation-dependent Energy Separation	60
5.3	Effect of PZ field in different crystal orientation	63
5.4	Operating point close to Threshold	65
5.5	Bandwidth of InGaN/GaN QW Blue LD in different crystal orientation	66
5.6	Strain-dependent Energy Separation for $(11\bar{2}2)$ crystal orientation	68
5.7	Bandwidth of InGaN/GaN QW Blue LD for different In composition	72

\

LIST OF FIGURES

Figure No	Description	Page
2.1	Simplified laser diode structure and schematic symbol	10
2.2	Band gap profile for (a) Single QW SCH (b) Multiple QW SCH (c) Graded index SCH Semiconductor Laser	11
2.3	Schematic representation of the potential energy profile of a 1-D QW	13
2.4	Electron transitions between conduction band (top) and valence band (bottom); a) spontaneous recombination, b) stimulated emission and c) non-radiative recombination	14
2.5	Relative band edge transition strengths for a quantum well, a) heavy-hole transition strength, b) light-hole transition strength and c) split-off transition strength	16
3.1	Wurtzite structure of III-nitride compounds for a polar (c-plane) and a non-polar (m- and a-plane) crystal orientations	22
3.2	The bandgap and lattice constants of Reputed WZ and ZB III-N	23
3.3	Schematic representation of a) separate InGaN epilayer and GaN bulk layers, b) a strained InGaN epilayer embedded between GaN bulk barrier layers	24
3.4	Optical confinement of light rays in a waveguide composed of media 1 and 2	28
3.5	Schematic band structure diagram of a single InGaN/GaN QW oriented along different crystal axes	30
3.6	Abrupt p-n junction in thermal equilibrium	34
3.7	Schematic Representation of some of the nonpolar, semipolar and polar planes for Wurtzite Crystal	37
4.1	Structure of proposed InGaN/GaN QW Blue Laser	39
4.2	Basis Function for the Hamiltonian	43
4.3	Configuration of the coordinate systems (x',y',z') in (hkil)-oriented crystals	45
4.4	Full operating region of Laser Diode	51
4.5	Simulink Model for Output Power-Current Response from InGaN Laser	53
5.1	Strain tensor components as function of crystal angle for 15%, 17%, 19% and 21% In	57
5.2	(a) Sum of the strain-induced PZ and SP polarizations normal with respect to the growth plane for the well and the barrier and (b) Internal field as a function of the angle θ between the growth direction and the *c*	58

	axis of $In_xGa_{1-x}N/GaN$ QW structure	
5.3	Energy Band Dispersion Profile in (a) (0001), (b) $(10\bar{1}0)$, (c) $(10\bar{1}2)$ (d) $(11\bar{2}2)$ and (e) $(10\bar{1}1)$ Crystal Orientation of InGaN/GaN QW Blue Laser	59
5.4	Interband optical momentum matrix elements at the band edges as a function of crystal orientation for the (a) TE and (b) TM polarizations of $In_{0.17}Ga_{0.83}$ N/GaN QW blue laser	60
5.5	Crystal orientation-dependent normalized momentum matrix element for (a) C-HH transition and (b) C-LH transition	61
5.6	Optical emission profiles of $In_{0.17}Ga_{0.83}N/GaN$ QW Blue Laser in different orientation for (a) TE Polarization and (b) TM polarization	62
5.7	Carrier density-dependent optical gain in different crystal orientations	63
5.8	Orientation-dependent Output Power Curve of InGaN/GaN QW Blue Laser Diode	64
5.9	Frequency Response of InGaN/GaN QW Blue LD in different crystal orientation using operating points from Table 5.5	65
5.10	Energy Band Dispersion Profile for InGaN/GaN QW blue laser in $(11\bar{2}2)$ crystal orientation for (a) 15% Indium (b) 17% Indium (c) 19% Indium (d) 21% Indium	67
5.11	Strain-dependent momentum matrix element for C-HH transition	69
5.12	Optical gain profile of InGaN/GaN QW blue laser for different values of compressive strain (a) TE Polarization (b) TM Polarization	69
5.13	Peak gain as a function of carrier concentrations for different compressive strained QWs	70
5.14	Output optical power-input current response for different compressive strained QWs	71
5.15	Frequency Response in $(11\bar{2}2)$ orientation for different compressive strained QW	72
5.16	Energy Band Dispersion Profile for InGaN/GaN QW blue laser in $(10\bar{1}2)$ crystal orientation for (a) 15% Indium (b) 17% Indium (c) 19% Indium (d) 21% Indium	73
5.17	Strain-dependent momentum matrix element for C-HH transition	74
5.18	Optical gain profile of InGaN/GaN QW blue laser for different values of compressive strain (a) TE Polarization (b) TM Polarization	74
5.19	Peak gain as a function of carrier concentrations for different compressive strained QWs	75
5.20	Output optical power-input current response for different compressive strained QWs	76
5.21	Frequency Response in $(10\bar{1}2)$ orientation for different compressive strained QW	76

CHAPTER I

Introduction

1.1 Background of the Thesis

Laser (Light Amplification by Stimulated Emission of Radiation) makes use of stimulated emission, and optical feedback provided by mirrors to increase or amplify light signals [1]. Townes and Schawlow introduced the concept of laser by extending the maser operating frequency to optical range [2]. Maser is a microwave amplifier which produces a coherent beam of microwaves. Townes and Schawlow both received Noble prizes for their work in this field in 1964 & 1981 respectively. In 1960, Theodore Maiman of Hughes Research Laboratories produced the first laser using ruby crystal as the laser medium and a flash lamp as the excitation source [3]. The first gas laser was developed in 1961 by A. Javan, W. Bennett, and D. Harriott of Bell Laboratories, using a mixture of helium and neon gases [4]. At the same Laboratories, L.F. Jonson et al demonstrated the first neodymium laser, which has since become one of the most reliable lasers available [5]. The first semiconductor laser was demonstrated by R. Hall at General Electric Research Laboratories in 1962 [6]. The early semiconductor laser was based on p-n homojunction structure. But the carrier and optical confinement level in homojunction structure is not satisfactory. Again, homojunction laser cannot be operated continuously at room temperature which is a major drawback [7]. The carrier and optical confinement can be effectively achieved by Quantum well (QW) double heterostructure. QW structures show quantized sub-bands and step-like densities of states. The density of states for a quasi-two dimensional structure has been used to reduce threshold current density and improve temperature stability. Energy quantization provides another degree of freedom to tune the lasing wavelength by varying the well width and the barrier height. In 1975, the first QW laser was made in GaAs by J. van der Ziel and co-workers at Bell Laboratories [8].Since then, ample investigations have been done on different structures and active channel material of QW lasers. First short-wavelength (λ<530 nm) QW laser diodes (lasers) were demonstrated on (Zn, Cd, Mg) (Se, S) II-VI materials in early 1990's [9, 10]. Research was first focused on II-VI compounds due to their same crystal structure and similar lattice constant to GaAs, which make the II-VI crystal growth with low defect density (10^3~10^4 cm^{-2}) on GaAs substrates straight forward. In 1998, II-VI

lasers' lifetime was increased to 400 hours under the CW-mode operation with an optical power of 1 mW [11]. But shortly, researchers found that it was very difficult to further increase the lifetime and output power to a commercial level due to the unstable and fragile II-VI materials.

1.1.1 Prospect of III-N material for Optical Devices

Recently, III-N materials (GaN, InN and AlN) have been emerged as highly attractive material for fabricating QW laser structure due to their spectacular properties like high electron mobility and saturation velocity, high breakdown field, high thermal conductivity, and high quantum efficiency. III-N materials with the WZ crystal structure have direct band gap (BG), so they are suitable for short-wavelength LEDs and lasers. With the combination of binary alloys GaN and InN, the ternary alloy InGaN is a promising candidate for high power and high-speed optoelectronics. The InGaN QWs are indispensable for light emitting devices because incorporation of small concentrations of In in the active GaN layer increases luminescence efficiency considerably. By adding proper amount of indium to form $In_xGa_{1-x}N$ QWs in the active region, InGaN/GaN-based lasers can effectively emit light in the wavelength ranges from 400 nm to 550 nm, where three wavelength regions are of considerable commercial importance: 400 nm ~ 420 nm (violet), 440 nm ~ 470 nm (blue), and 520 nm ~ 540 nm (green) [12,13].

1.1.2 Significance of InGaN-based Blue Laser

Blue-violet lasers based on strained wurtzite (WZ) $In_xGa_{1-x}N$/GaN QW structures have been realized recently with a lifetime of many thousand hours [14]. They're key devices in high-density optical storage systems, high-resolution laser printers, Phototherapy treatment, HR-endoscopy, telecommunications, environmental monitoring and magnetic devices, etc. A blue laser is capable to store and read two to four times the amount of data than red laser [15, 16]. The short lasing wavelength allows a small diffraction-limited spot size, which enhances the data density of optical storage systems and the resolution of printers. Being insensitive to infrared radiation, blue-laser sensors provide precise measurement with red-hot glowing metals. Compared to the light emitting diode (LED) lamp projectors, lasers provide high spectral purity, excellent color saturation, high resolution, high contrast ratio, and a practically unrestricted focus depth. For true blue emission, lasers oscillate at a wavelength of 445~450 nm is required.

Although blue laser is highly demanded from the application point of views, it was hard to have blue laser before 1990 due to difficulty in $In_xGa_{1-x}N$ growth. The large difference in interatomic spacing between GaN and InN and high nitrogen pressure over InN due to N volatility are the causes that give rise to a solid phase miscibility gap. To mitigate this problem, V/III ratios in excess of 20000, increasing with InN mole fraction, as well as reduced growth temperatures were employed, but at the expense of reduced quality. Efforts to increase the In concentration by raising the indium precursor temperature or the carrier gas flow rate resulted in the degradation of the structural and surface morphology so much that In droplets were formed on the surface. Another major problem in producing blue lasers was the difficulty in p-doping GaN with precision. Since InGaN is responsible for emission in the near-UV, violet, blue, and green colors of the optical spectrum, researchers like Akasaki and Amano, and separately Nakamura were trying to sort out the complexities in order to develop large, high-quality InGaN crystals [17,18].

1.2 Present Status of InGaN-based Blue Laser

Nakamura et al. [14] first earned one of the top blue laser breakthroughs in the 1992 by realizing high quality InGaN QW structures for blue emission experimentally. The first InGaN/GaN MQW violet laser was grown on sapphire substrates and demonstrated in 1995 by Nichia [19]. In 1996 and 1997, Toshiba, Cree, Fujitsu and UCSB successfully fabricated violet laser [20]. However, life time of the fabricated lasers was very poor due to unavailability of suitable substrate for InGaN active layer [21]. In 1998, Nichia demonstrated CW-mode violet lasers with a lifetime longer than 10,000 hours, and then the violet InGaN-based QW lasers progressed to commercialization. In 2000, the output power increased to 30 mW, which fulfilled the requirement of the high-density optical disk recording system. In the following years, all the major consumer electronics companies, such as Sony, Toshiba, Samsung, LG, Philips, Sharp, etc., made great efforts to develop violet-laser-based high-density optical storage systems for high-definition (HD) videos and huge amount of data storage. In March 2006 Toshiba released the first consumer-based HD DVD player in Japan (sailing stopped in March 2008), and three months later the famous Blu-ray Disc™ players were released by Sony. All of the lasers so far reported were realized on polar c-plane GaN substrates and listed in Table 1.1. But the design of InGaN/GaN-based lasers of c-plane (0001) crystal orientation has several challenges, such as the quantum-confined stark effect (QCSE), the efficiency drop issue, and the optical confinement

design optimization. So optoelectronic devices grown on non-polar and semi-polar planes are of special interest to scientific community and the industry [22].

Table 1.1. Performance of InGaN/GaN-based lasers on c-plane GaN substrates [23]

Group (year)	λ (nm)	Cavity Size (μm^2)	Slope Efficiency (W/A)	Optical Power (mW)	J_{th} (kA/cm^2)	Operation mode (lifetime)
Nichia (2005)	482.1	2.5×675	-	7	6.2	CW (3000 hrs)
Nichia (2006)	473	2.0×650	-	20	4.2	CW (10000 hrs)
Samsung (2007)	448	2.5×650	0.7	300	1.85	CW (5000 hrs)
Osram (2008)	441	1.5×600	1.0	60	2.78	-
Samsung (2008)	485	2.0×650	0.12	10	7.16	CW
Nichia (2008)	488	-	-	5	3.3	CW (10000 hrs)
Osram (2009)	500	-	0.65	70	8.2	Pulse
Nichia (2009)	445	-	-	1000	-	CW (30000 hrs)
Nichia (2009)	515	2.0×600	0.14	8	4.4	CW (5000 hrs)
Osram (2009)	515.9	11×600	0.13	50	9.0	Pulse
Osram (2010)	524	1.8×600	0.33	50	9.0	CW
UM (2013)	630	-	-	200	2.5	CW (5000 hrs)
Sinano (2016)	508	-	-	58	1.8	CW

1.3 Research Motivation

In spite of an enormous progress in the development of GaN-based lasers on c-plane substrates as seen in Table 1, these devices still have significantly lower efficiency and higher threshold currents. In comparison with GaAs-based QW's, WZ GaN-based QW's of c-plane (0001) crystal orientation need high carrier densities to produce optical gain [24]. This is due to the heavy effective masses in the valence and conduction bands and strong interaction between heavy-hole

(HH) and light-hole (LH) bands at the Γ point. For a WZ layer grown along the (0001) orientation, the strain shifts both the HH and LH bands by almost the same amount, and the in-plane effective masses remain almost the same as those in the unstrained case. WZ GaN is noncentrosymmetric, which lacks inversion symmetry, yielding large built-in spontaneous polarization P_{sp} in the (0001) c-direction which is nearly 1/3rd the values for typical perovskite ferroelectrics such as $BaTiO_3$ [25]. Stemming from the lattice mismatch of InN and GaN, InGaN QWs grown pseudomorphically on GaN substrates will become elastically strained as long as it is below the critical thickness for plastic relaxation. For c-plane GaN, this is a biaxially compressive stress that induces an additional piezoelectric polarization. For QW structures, the discontinuities in polarization cause a build-up of sheet charges at the interfaces, producing an electric field that bends the energy bands. This band bending directs the electron and hole wave functions in opposite directions, and the resulting spatial separation of confined carriers can reduce oscillator strength and recombination rates. Additionally, the band bending reduces the transition energy of the bound states which can red-shift the emission wavelength. This effect is termed as the quantum-confined stark effect (QCSE), that can have deleterious effects on optoelectronic devices and worsens for QWs with higher indium compositions ($x>0.14$) due to increased lattice mismatch, making it particularly detrimental for blue laser applications. Thus, for the realization of high-performance nitride-based optical devices, control of the internal fields in the strained layers is indispensable [26].

Over the past few years, several investigations have been carried out on InGaN/GaN QW lasers grown on non-polar and semipolar oriented GaN substrate in order to reduce PZ polarization-induced internal field as listed in Table 1.2 and 1.3.

Table 1.2. Recent development of InGaN/GaN-based lasers on m-plane GaN substrates [27]

Group (year)	λ (nm)	Cavity Size (μm^2)	Slope Efficiency (W/A)	Optical Power (mW)	J_{th} (kA/cm^2)	Operation mode (lifetime)
UCSB (2007)	404.3	1.9×600	-	25	6.8	CW (15 hrs)
ROHM (2007)	451.8	1.5×600	-	20	22.3	Pulse
ROHM (2008)	459	2.0×400	0.37	5	5.0	CW
Sharp (2008)	463	1.5×600	0.91	10	7.8	Pulse

ROHM (2008)	481	2.5×400	0.49	20	6.1	CW
UCSB (2009)	441.2	8.0×500	-	20	10.7	Pulse
UCSB (2009)	465	2.0×500	-	25	19	Pulse
UCSB (2009)	481	4.0×500	-	17	18	Pulse
ROHM (2009)	499.8	2.5×600	0.05	15	3.1	CW
UCSB (2010)	461	4.0×500	0.3	5	4.1	CW
SORAA (2013)	523	-	-	1.5	-	CW
Schmidt (2015)	450	300×300	-	23.7	3.5	Pulse

Table 1.3 Recent development of InGaN/GaN-based laser on semipolar GaN substrates [28]

Group (year)	λ (nm)	Cavity Size (μm^2)	Slope Efficiency (W/A)	Optical Power (mW)	J_{th} (kA/cm^2)	Operation mode (lifetime)
UCSB (2008)	426.9	2.0×1200	0.14	20	12.8	Pulse
Sumitomo (2009)	531	10×600	-	-	15.4	Pulse
Sumitomo (2009)	520	2.0×600	0.1	2.5	7.9	CW
UCSB (2009)	405.9	1.4×600	0.26	10	6.5	CW
UCSB (2010)	506.4	3.0×1500	-	13	19	Pulse
Sony (2013)	525	-	-	50	4.5	CW (>5000 hrs)
Sony (2015)	530	-	-	100	5	CW (>5000 hrs)

But a number of complications still exist. Around 17% ~20% In needs to be incorporated in InGaN QWs to realize true-blue lasing emission, which results into the formation of crystalline defects in semi-polar and nonpolar oriented GaN substrates in two aspects. Firstly, as a result of weak chemical bond of In–N, the growth temperature for InGaN needs to be lowered to incorporate enough In. Secondly, the ideal growth temperature for AlGaN cladding layer is as high as 1000°C to ensure low resistance. However, such high temperature is going to induce

serious thermal degradation of InGaN QWs which results into crystalline defects, fluctuation of In composition, and rough interface in InGaN QWs. This rough interface and high threading dislocation density (TDD) (>$10^5/cm^2$) reduce the radiative efficiency and shorten device lifetimes. Therefore, it is imperative to explore alternative approaches [29].

In recent years, it's apparent that optical gain and threshold current of strained WZ III-N laser is strongly correlated with crystallographic axes of QW. In favorable band structure for higher optical gain, the splitting between heavy hole (HH) and light hole (LH) is increased and effective mass of holes is reduced which in turn, can augment interband transition energies near the band edge and diminish PZ-field induced QCSE. The splitting between valence subbands and effective masses can be controlled by changing the crystal orientation of QW which leads to have the possibility of novel electro-optic devices. So, crystal orientation is a new parameter in the engineering of strain-induced band structure modifications to optimize QW performance [30].

Okuno investigated direct wafer bonding technique (Unites two semiconductor materials at high temperature, without interposing any adhesive) of an InGaAsP system in terms of lattice constants and surface orientation of active layer with sufficient mechanical strength, and low TDD. In 2012, M.M. Hasan reported crystallographic orientation-dependent optical properties of GaInSb mid-infrared QW laser on GaSb substrate using direct bonding where the crystal orientation in the QW was changed arbitrarily but all other layers were in (001) orientation [31,32].

In a recent study [33], the orientation-dependent optical emission profile of true-blue laser using direct bonding was reported by our group for cubic InGaN. Here, orientation-dependent P-I profile as well as frequency-dependent characteristics of the laser was not investigated. It is to be noted here that GaN with cubic structure is very difficult to realize experimentally and it is not a stable crystal structure [34]. That is why, practical lasers cannot be obtained in this crystal structure. Although a lot of researches were carried on non-polar and semipolar oriented GaN substrate as listed in Table 2 and Table 3, all of these are experimental findings. To explore the performance of blue lasers in arbitrary orientations in details, numerical modeling is necessary. Because, to set up experiment in arbitrary orientations, is very much difficult and not viable from the economical point of view. In this research, our main target is to propose a WZ InGaN-based

QW blue laser structure with direct bonding of (0001) GaN substrate in which active region will be arbitrary (hkil) oriented and hence to develop a numerical model to study the emission profile, P-I characteristics, and frequency characteristics as a function of different crystal orientations for the proposed laser structure.

1.4 Specific Objectives

Herein, we attempt to address a comprehensive in-depth study on the orientation-dependent optoelectronic performance of 445 nm InGaN/GaN QW laser. The specific objectives of this research are delineated as follows:

- To propose an orientation-dependent WZ $In_{0.17}Ga_{0.83}N$/GaN QWs laser structure and then to develop a numerical model for the laser using k.p method.
- To study the orientation-dependent emission profiles and P-I characteristics for the proposed laser.
- Study of orientation-dependent energy band dispersion profiles (E-k diagram) and momentum matrix elements for the underlying laser structure to explain the results obtained in the present research.
- Study the impact of piezoelectric field on the orientation-dependent gain and P-I characteristics.
- Frequency response (Bode Plot) characteristics will also be analyzed using state-space representation.

The study will be done for 445nm $In_{0.17}Ga_{0.83}N$/ GaN QW true blue laser along (0001) , $(10\bar{1}0)$, $(10\bar{1}2)$, $(11\bar{2}2)$ and $(10\bar{1}1)$ crystal orientations in MATLAB/Simulink environment using six-band Rashba-Sheka-Pikus (RSP) k.p Hamiltonian at Γ-point. Two-level rate equation which account for carriers in both active and barrier layer will be constructed in Simulink to find P-I response in different crystal orientation. In order to obtain the frequency response, the linearized rate equations will be utilized to establish a state-space model that allows the results of the P-I response to be used in simulating the frequency response. The compressive strain-dependent optoelectronic performance for this QW laser will also be analyzed.

1.5 Organization of the thesis

The layout of this thesis work is organized in six chapters.

In Chapter 1, background of the present work is explained. Present status and future prospect of the present work are described clearly in this chapter. Finally objectives of the present work are summarized in this chapter.

Chapter 2 starts with an overview of quantum well (QW), density of states, electron transition mechanism and a description of the fundamentals of LASERs. Further study will be concentrated on the working principle of QW laser where the lasing condition, cavity modes and output characteristics have discussed. Before conclusion, Two-level rate equation theory used in the simulation is also discussed.

In Chapter 3, a brief overview of the main structural, optical and electrical properties of InGaN is presented. Particular attention is devoted to the band structure and band profile of III-nitride heterostructures, especially with respect to the polarization mismatch of the different binary compounds. Then, the impact of the quantum confined Stark effect on the optical features is discussed. Finally, the modes of operation of a typical *p*-*n* junction implemented in a laser Diode are introduced.

Chapter 4 starts with the device structure that has been used in this thesis. Then, description of **k.p** method for band structure calculation and tensor rotation technique to represent the relationship of the general (hkil) coordinates system to the conventional (0001) crystal coordinate system is discussed. The formula for crystal orientation-dependent piezoelectric field and optical emission profile is demonstrated afterwards. Finally, a Simulink design and state-space model is presented in order to simulate the P-I response and bode-plot of the proposed laser structure.

In chapter 5, the results obtained based on mathematical modeling of the proposed laser structure are presented. The effect of stain and change in crystal orientation on conduction and valence bands and gain profiles are the main concern of this chapter. The effect of piezoelectric fields on energy band and optical gain are presented here. Finally, the output optical power-input current characteristics and frequency response (bode-plot) of the single InGaN QW blue laser are also shown for different values of strain and crystal orientations.

Chapter 6 provides the conclusion of the present research and the prospect for the future studies.

CHAPTER II

Fundamental Concepts of the Research

This chapter starts with description of basic working principle and application of laser diode. Next a brief discussion on optical emission from semiconductors is given which includes an overview on the fundamental operating principle, structure and the materials for QW laser.

2.1 Brief Overview on Semiconductor Laser

A Laser Diode is an electrically pumped semiconductor laser in which the active laser medium is formed by a p-n junction. There is a highly reflective surface at one end of the p-n junction and a partially reflective surface at the other end, forming a resonant cavity for the photons. The following figure shows simplified laser diode construction.

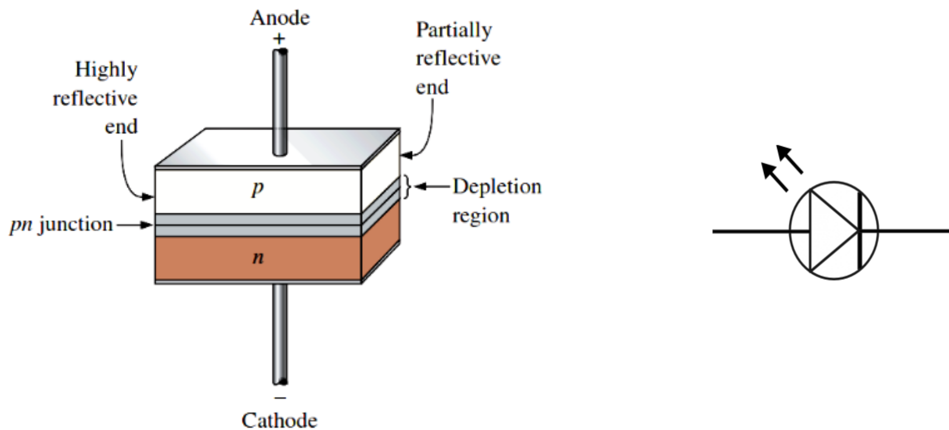

Fig 2.1: Simplified laser diode structure and schematic symbol

The LD is forward biased by an external voltage source. As electrons move through the junction, recombination occurs and photons are released. A released photon can strike an atom, causing another photon to be released. As the forward current is increased, more electrons enter the depletion region and cause more photons to be emitted. Eventually some of the photons that are randomly drifting within depletion region strike reflected surface causing avalanche multiplication, thus releasing additional photons. This process continues till a very intense beam of laser light is formed by the photons that pass through the partially reflective end of p-n junction. Photons, which are emitted into the waveguide, can travel back and forth in this

waveguide provided they are reflected at the mirrors. The distance between the two mirrors is the cavity length. Each photons produced in the process is identical in energy level, phase and frequency [35].

2.1.1 Laser Types

Lasers are grouped broadly into following five classes depending on the active medium construction. Brief details on QW laser is given later.

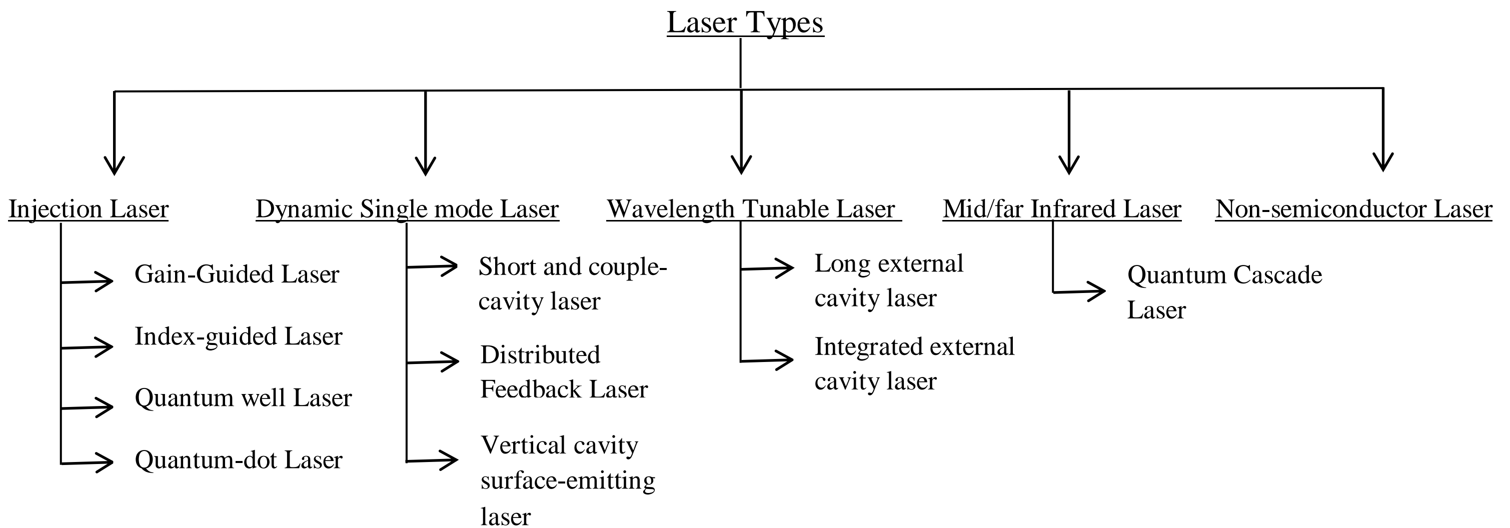

QW structures as shown in Fig. 2.2 have been used as the active layer of semiconductor laser diodes with reduced threshold current densities as compared with those for conventional double heterostructure (DH) semiconductor diode lasers. QW structures show quantized sub-bands and steplike densities of states. The density of states for a quasi-two dimensional structure has been used to reduce threshold current density and improve temperature stability [36].

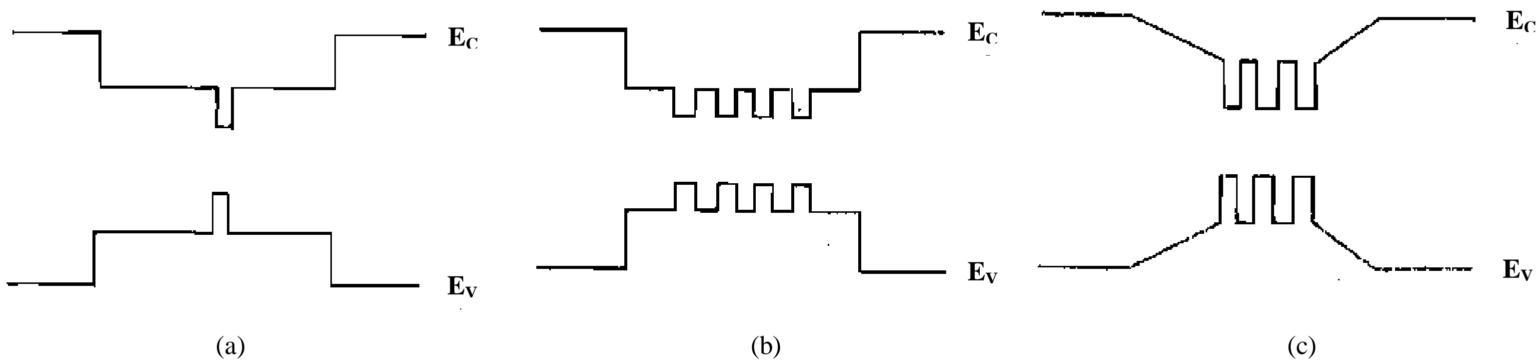

Fig. 2.2: Band gap profile for (a) Single QW SCH (b) Multiple QW SCH (c) Graded index SCH Semiconductor Laser

2.1.2 Applications of Laser Diode

Low power Lasers are used in an increasing number of familiar applications including CD and DVD players and recorders, bar code readers, security systems, optical communications and surgical instruments.

Industrial applications: Engraving, cutting, scribing, drilling, welding, etc.

Medical applications: Removing unwanted tissues, diagnostics of cancer cells using fluorescence, dental medication. In general, the results using lasers are better than the results using a surgical knife.

Laser Diodes used for Telecom: In the telecom field 1.3 μm and 1.55 μm band laser diodes used as the main light source for silica fiber lasers have a less transmission loss in the band. The laser diode with the different band is used for pumping source for optical amplification or for the short-distance optical link.

2.2 Basic Physics of QW Laser

2.2.1 Quantum Well

If a semiconductor with a bandgap, E_{g1}, is embedded in another semiconductor with a larger bandgap, $E_{g2} > E_{g1}$, a potential minimum or well is formed. If the thickness of the embedded semiconductor, L_z, is reduced to less than or equal to λ_d (the de Broglie wavelength) for an electron, quantum mechanical effects become significant and the embedded semiconductor is referred to as a quantum well (QW). The spatial confinement of electrons in the z-direction separates the continuum of energy levels associated with a bulk material within the QW [37]. To determine the quantized energy levels within a QW it is necessary to solve the time-independent part of Schrodinger's equation:

$$\frac{-\eta^2}{2m}\nabla^2\Psi + V\Psi = \mathrm{E}\Psi \qquad (2.1)$$

Where, m, Ψ and E are the particle's mass, wavefunction and energy, and V is the potential profile of the QW. The general solution for a uniform potential, such as a QW, may be expressed as the sum of two counter-propagating plane waves,

$$\Psi(r) = Ae^{ikz} + Be^{-ikz}; k^2 = \frac{2m}{\eta^2}(E - V) \qquad (2.2)$$

As an example, take a QW of width L_z and depth V_0, symmetrical about z=0, which may be split into three regions, as shown in Figure 2.3. For $E < V_0$, region II, the general solution, may be written as:

$$\Psi_{II} = \begin{cases} A\cos kz \\ A\sin kz \end{cases} \quad \text{where, } k^2 = \frac{2mE}{\hbar^2}$$

$$\Psi_{III} = Be^{-\gamma z}$$

For region III where $\gamma^2 = 2m(V_0 - E)/\hbar^2$. In region I Ψ_1=B$e^{\gamma z}$, however due to symmetry we only need to consider the single boundary at z=L_z/2. Assuming the particle mass is the same in all regions we can develop a complete wavefunction by requiring that the value and first derivative, of the constituent solutions, are equal at the boundaries. For the symmetric case this gives:

$$A\cos\left(\frac{kL_z}{2}\right) = B\exp\left(\frac{-\gamma L_z}{2}\right); Ak\sin\left(\frac{kL_z}{2}\right) = B\gamma\exp\left(\frac{-\gamma L_z}{2}\right) \quad (2.3)$$

Dividing above two equations leads to the characteristic equations

$$k\tan\left(\frac{kL_z}{2}\right) = \gamma \text{ (Symmetric solution)}$$

$$k\cot\left(\frac{kL_z}{2}\right) = \gamma \text{ (Anti-symmetric solution)}$$

The individual energy levels may be found by plotting *ktan(kL_z/2), kcot(kL_z/2)* and γ as a function of energy. Figure 2.3 shows the first few wavefunctions drawn schematically on their respective energy levels.

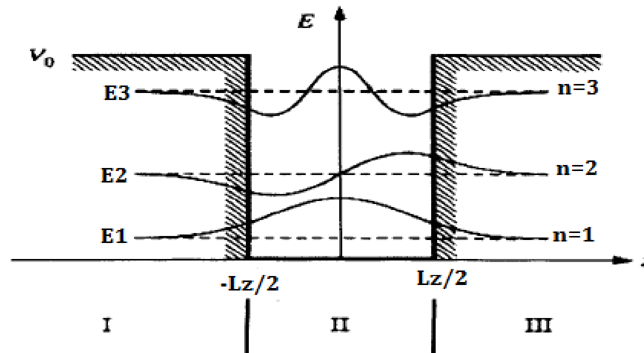

Fig. 2.3: Schematic representation of the potential energy profile of a 1-D QW

2.2.2 Density of States

To calculate semiconductor properties or analyze device behavior it is often necessary to know the carrier density, or the Fermi level energy needed to achieve a particular carrier density. The common method is to define a *density of states* (DOS), ρ which when integrated over some range gives the number of states, N_s, in that range:

$$N_s(E) = V \int_0^E \rho(E) dE \tag{2.4}$$

where E is the energy over which the number of states is to be calculated and V is the volume. So, DOS can be defined as:

$$\rho(E)dE = \frac{1}{V} dN_s(E) \tag{2.5}$$

The following standard procedure can then be used to determine $\rho(E)$: firstly determine the volume in state or n-space over which the integral is to be carried out; secondly solve for n in terms of E which resulting in the following definitions:

$$\rho(E) = \frac{1}{2\pi^2} [\frac{2m*}{\eta^2}]^{3/2} E^{1/2} \qquad \text{for bulk } (m^{-3})$$

$$\rho(E) = \frac{1}{L_z} \sum_i \frac{m*}{\pi\eta^2} \mathrm{H}(E - E_i) \qquad \text{for QW } (m^{-3})$$

where, $\mathrm{H}(E - E_i)$ is the Heaviside unit step function.

2.2.3 Electron Transition Mechanism

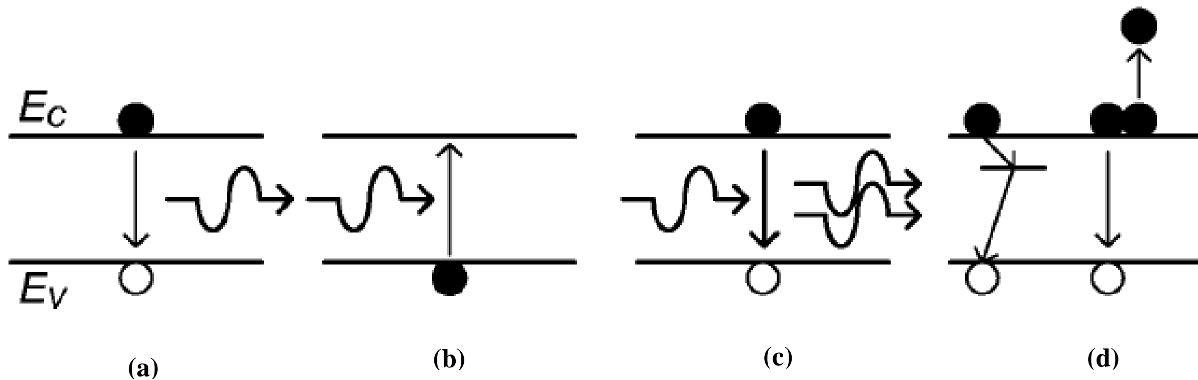

Fig 2.4: Carrier transition mechanisms between the conduction band and valence band in semiconductors: (a) spontaneous recombination, (b) stimulated generation, (c) stimulated recombination, and (d) non-radiative recombination

Figure 2.4 illustrates the four important electronic transitions possible within semiconductor devices: (a) spontaneous emission, (b) induced absorption, (c) stimulated emission and (d) non-radiative recombination.

Spontaneous emission occurs when an electron in the conduction band spontaneously recombines with a hole in the valence band emitting a photon. The direction, frequency and polarization of the emitted photon are random and thus spontaneous recombination does not produce a coherent radiation field. This is the predominant radiative mechanism in light-emitting diodes (LEDs), since photon feedback is not usually provided.

Induced absorption involves the absorption of a photon of light. The energy associated with the photon is transferred to the electron, which is excited from the valence band to the conduction band if the energy of the photon is greater than or equal to the transition energy.

Stimulated emission is similar to stimulated absorption only the position of the electron is reversed. The incident photon perturbs the system, stimulating an electron in the conduction band to recombine with a hole in the valence band. The energy the electron loses in the transition is emitted as a photon. This photon will have exactly the same frequency, polarization and be emitted in the same direction as the incident photon. Stimulated emission is the process which provides the coherent radiation field produced by lasers.

Finally non-radiative recombination involves an electron in the conduction band transferring to the valence band via localized defects, without producing any useful light. Since the capture of electrons and holes onto the defect state are independent processes the overall capture rate will be limited by the slowest capture process (either electron or hole capture) therefore the non-radiative recombination rate tends to be proportional to the carrier density. The equations describing the above electron transition mechanisms are given below:

$R_r = \int r_{sp}(h\nu)dh\nu,$ (which, within a Boltzmann approximation = Bnp)

$$R_{nr} = \frac{n}{\tau_{nr}}$$

Where, R_r is the total spontaneous radiative recombination rate, $r_{sp}(h\nu)$ is the radiative recombination rate at frequency ν, B is the radiative recombination coefficient, n and p are the

number of electrons and holes, R_{nr} is the total non-radiative recombination rate and τ_{nr} is the non-radiative lifetime [38].

2.2.4 Electron Transition Strength [39]

The probability of an electron transition between the conduction and valence band energy levels is determined by the transition matrix element, defined as:

$$|M_T|_v{}^2 = \frac{1}{2}\sum_{u_c\overline{u_c}}\sum_{u_v\overline{u_v}}|\langle u_c|\hat{e}.p|\rangle u_v|^2 \quad (2.6)$$

where the envelope function overlap integral has been set equal to unity, assuming the electron and hole wavefunctions overlap exactly. By replacing the dot product with the expansion $e_xp_x + e_yp_y + e_zp_z$, the above expression can be reduced to:

$$\frac{|M_T|_v{}^2}{|M|^2} = \begin{cases} \frac{1}{2}\left(e_x{}^2 + e_y{}^2\right) = \frac{1}{2}\left(1 - \left|\hat{\boldsymbol{k}}.\hat{\boldsymbol{e}}\right|^2\right) & \text{for HH band} \\ \frac{1}{6}\left(e_x{}^2 + e_y{}^2 + 4e_z{}^2\right) = \frac{1}{2}\left(\frac{1}{3} + \left|\hat{\boldsymbol{k}}.\hat{\boldsymbol{e}}\right|^2\right) & \text{for LH band} \\ \frac{1}{3}\left(e_x{}^2 + e_y{}^2 + e_z{}^2\right) = \frac{1}{3} & \text{for SO band} \end{cases}$$

In a QW, where all k-vectors point along the same axis due to quantum confinement, choosing the direction of confinement to correspond with the z-axis this equation leads to the following directional dependence of the transition strength, as illustrated in Figure 2.5 below.

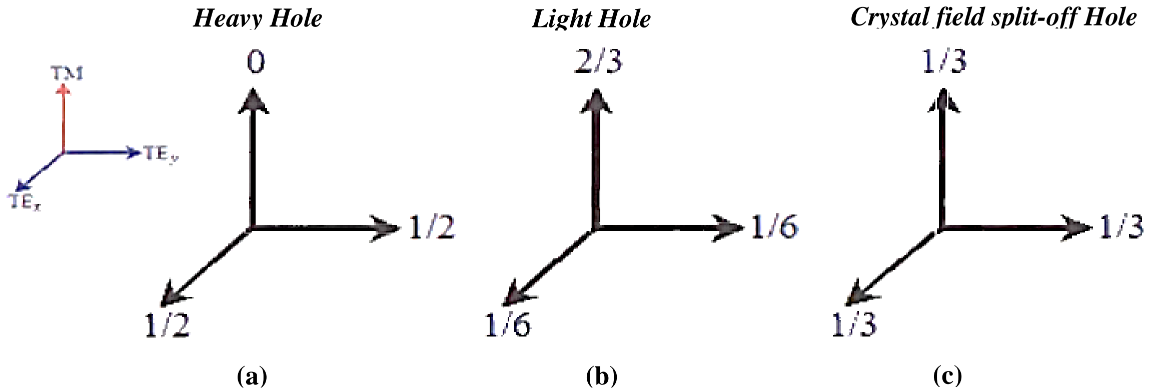

Fig 2.5: Relative band edge transition strengths for a quantum well, a) heavy-hole transition strength, b) light-hole transition strength and c) split-off transition strength

$|M_T|^2$ will also have a dependence on the envelope function overlap integral since in reality it is not equal to unity. However at the band edge the overlap integrals are close to unity (typically

within 5-10% and would be exactly equal to unity if the conduction and valence band effective masses were identical. Also the presence of piezoelectric fields within the QW, which cause the QW to be triangular rather than square, means the envelope function overlap integral will not be equal to unity and thus should be included in the determination$|M_T|^2$.

2.2.5 Lasing Condition

Combined with the waveguide losses, stimulated emission yields a net gain per unit length, g. The number of photons can therefore be maintained if the round-trip amplification in a cavity of length, L, including the partial reflection at the mirrors with reflectivity R_1 and R_2 equals unity. This yields the following lasing condition:

Roundtrip amplification= $e^{2gL} R_1R_2 = 1$

If the round-trip amplification is less than one then the number of photons steadily decreases. If the round-trip amplification is larger than one, the number of photons increases as the photons travel back and forth in the cavity and no steady state value would be obtained. The gain required for lasing therefore equals:

$$g = \frac{1}{2L} \ln \frac{1}{R_1R_2} = 1 \qquad (2.7)$$

Initially, the gain is negative if no current is applied to the laser diode as absorption dominates in the waveguide. As the laser current is increased, the absorption first decreases and the gain increase [40].

2.2.6 Output Power

The current for which the gain satisfies the lasing condition is the threshold current of the laser, I_{th}. Below the threshold current very little light is emitted by the laser structure. For an applied current larger than the threshold current, the output power, P_{out}, increases linearly with the applied current. The output power therefore equals:

$$P_{out} = \eta \frac{h\nu}{q} (I - I_{th}) \qquad (2.8)$$

where $h\nu$ is the energy per photon. The factor η indicates that only a fraction of the generated photons contribute to the output power of the laser as photons are partially lost through the other mirror and throughout the waveguide [36].

2.3 Laser Cavities and Laser Cavity Modes [41]

A laser diode consists of a cavity, defined as the region between two mirrors with reflectivity R_1 and R_2, and a gain medium, in our case a quantum well. The optical mode originates in spontaneous emission, which is confined to the cavity by the waveguide. This optical mode is amplified by the gain medium and partially reflected by the mirrors. The modal gain depends on the gain of the medium, multiplied with the overlap between the gain medium and the optical mode which we call the confinement factor, Γ, or:

Modal gain = g(N) Γ

Lasing occurs when the round trip optical gain equals the losses. For a laser with modal gain *g(N)*Γ and waveguide loss, α, this condition implies:

$$R_1 R_2 \exp[2(g(N) - \alpha)L] = 1 \qquad (2.9)$$

where *L* is the length of the cavity. The distributed loss of the mirrors is therefore:

Mirror loss = $\frac{1}{L} ln \frac{1}{\sqrt{R_1 R_2}}$; R_1 and R_2 = Mirror Reflectivity

2.3.1 Longitudinal modes in the laser cavity

Longitudinal modes in the laser cavity correspond to standing waves between the mirrors. If we assume total reflection at the mirrors, this wave contains *N*/2 periods where *N* is an integer. For a given wave length *l* and a corresponding effective index, n_{eff}, this yield:

$$N = \frac{2n_{eff} L}{\lambda}$$

Because of dispersion in the waveguide, a second order model should also include the wavelength dependence of the effective index. Ignoring such dispersion effects, we find the difference in wavelength between two adjacent longitudinal modes from:

$$N = \frac{2n_{eff} L}{\lambda_1}$$

$$N + 1 = \frac{2n_{eff} L}{\lambda_2}$$

$$\Delta\lambda = 2Ln_{eff}\left(\frac{1}{N} - \frac{1}{N+1}\right) \cong \frac{\lambda_1^2}{2Ln_{eff}}$$

Longer cavities therefore have closer spaced longitudinal modes. These wavelength differences can be converted to energy differences using $\Delta E = \frac{hc}{2Ln_{eff}} = E_{ph}\frac{\Delta\lambda}{\lambda^2}$

2.3.2 Waveguide modes [42]

The optical modes in the waveguide determine the effective index needed to calculate the longitudinal modes as well as the confinement factor. Starting from Maxwell's equations in the absence of sources and assuming a propagating wave in the *z*-direction and no variation in the

$$\overline{\nabla} \times \overline{\mathrm{H}} = \varepsilon_0 n^2(x, y, z)$$

$$\overline{\nabla} \times \overline{\mathrm{E}} = \mu_0 \frac{\partial \overline{\mathrm{H}}}{\partial t}$$

y-direction, we obtain the following one-dimensional reduced wave equation for a time harmonic field, $E = E_x \exp(j\omega t)$ of a TM mode:

$$\frac{d^2E_x}{dx^2} + (n^2(x)k^2 - \beta^2 E_x) = 0 \qquad (2.10)$$

Where, $\beta = \frac{\omega}{c} n_{eff}$ and $k = \frac{\omega}{c}$

The equation then becomes:

$$\frac{d^2E_x}{dx^2} + \left(n^2(x) - n^2{}_{eff}\right)E_x = 0 \qquad (2.11)$$

The energy eigenvalues can then be interpreted as minus the effective indices of the modes.

2.3.3 The confinement factor

The confinement factor is defined as the ratio of the modal gain to the gain in the active medium at the wavelength of interest:

$$\Gamma = \frac{\int_{-\infty}^{\infty} g(x)|E_x|^2 dx}{\int_{-\infty}^{\infty} |E_x|^2 dx} \qquad (2.12)$$

For a quantum well with width L_x, the confinement factor reduces to

$$\Gamma = \frac{\int_{-Lx/2}^{Lx/2} g(x)|E_x|^2 dx}{\int_{-\infty}^{\infty} |E_x|^2 dx} \cong \frac{D^2}{D^2+2} \qquad (2.13)$$

Here, $D = \frac{2\pi t}{\lambda}\sqrt{n_{well}^2 - n_{cladding}^2}$; t=thickness of active layer and n=refractive index

CHAPTER III

Properties of InGaN Material

Optoelectronic devices based on the InGaN system exhibit unique features that have to be taken into account during their design and fabrication. In this chapter, the main characteristics concerning structural, optical and electrical properties of InGaN are presented. First, the structural parameters and the subsequent polarization features of InN and GaN are discussed. The main optical parameters involved in the development of a semiconductor emitting structure such as the bandgap energy and the quantum confined Stark effect (QCSE) are introduced here. At last, a brief overview on polar, non-polar and semipolar crystal orientation is given.

3.1 Brief History on InGaN Development

InGaN has emerged as the leading material for fabricating high efficiency and high reliability short wavelength emitters ($\lambda<530$ nm). The growth of InGaN alloys has proven to be relatively more difficult. The large difference in interatomic spacing between GaN and InN and high nitrogen pressure over InN due to N volatility are the causes that give rise to a solid phase miscibility gap. To obtain electrical and optical characteristics compatible with optoelectronic devices, growth of high quality III-nitride heterostructures is necessary. Therefore, the thickness of layers in the active region has to be controlled down to the monolayer (ML) scale and hence sophisticated epitaxial growth methods are used. The early attempts for realizing single crystalline InGaN by OMVPE were made by Nagatomo et al. in 1989 and Matsuoka et al. again in 1989, and followed by Yoshimoto et al. in 1991 [43-45]. Since then, considerable work has been expended worldwide. Matsuoka et al. discovered that lowering the growth temperature to 500°C from nominal temperatures, such as 800°C, increased the In content in the layers, but at the expense of reduced quality. Efforts to increase the In concentration by raising the indium precursor temperature or the carrier gas flow rate resulted in degradation of the structural and surface morphology so much so that In droplets were formed on the surface, which is common to all the other growth methods, including sputtering[46]. In 1991 Nakamura et al. obtained high-quality GaN for the first time using a low temperature GaN buffer layer on a sapphire substrate [47]. Current technology primarily employs three kinds of reactors to grow group-III-nitride thin

films: hydride vapor phase epitaxy (HVPE), molecular beam epitaxy (MBE) and metal-organic vapor phase epitaxy (MOVPE). Large growth rates can be achieved with HVPE. This technique is usually exploited for the growth of thick InGaN epilayers as it allows for growth rates exceeding 500μm/h. Those thick InGaN layers are often used for preparing free-standing (FS) GaN substrates with low threading dislocation density (TDD). On the contrary, MBE is performed in an ultrahigh vacuum chamber and presents a relatively low growth rate (often less than 1 μm/h). The source materials are evaporated from effusion cells and directed toward the heated substrate. This technique allows monitoring the growth rate with a precision down to the ML thanks to in situ RHEED (reflection high energy electron diffraction) oscillations. Moreover, a primary advantage of plasma-assisted MBE for III-nitrides is the low temperature of growth that can be realized thanks to the use of an atomic nitrogen plasma source, which results in lower thermal stress upon cooling, less diffusion, and reduced alloy segregation. This low growth temperature is of high interest for the growth of indium rich InGaN alloys and for alloys with large thermal expansion coefficient mismatch. Another advantage of MBE is the absence of hydrogen passivation of as-grown p-In GaN films. LDs in the III-nitride materials system are commonly grown homoepitaxially by MOVPE on c-plane oriented FS GaN substrate. This technique allows an easy control of the growth parameters, a good reproducibility and is also well-suited for large scale production. MOVPE is a non-equilibrium growth technique (closer to thermodynamically equilibrium than MBE but less than HVPE), which consists in vapor transport of the precursors and subsequent reactions of group-III alkyls and group-V hydrides above a heated substrate [48-52]. Precursor materials are metal-organic compounds, such as, e.g., liquid trimethylgallium (TMGa) or solid trimethylindium (TMIn).

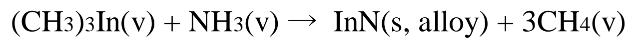

$$(CH_3)_3In(v) + NH_3(v) \rightarrow InN(s, alloy) + 3CH_4(v)$$

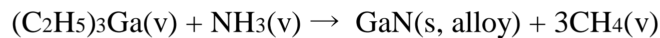

$$(C_2H_5)_3Ga(v) + NH_3(v) \rightarrow GaN(s, alloy) + 3CH_4(v)$$

where, InN(alloy) and GaN(alloy) stands for the binary compounds in the $In_xGa_{1-x}N$ alloy.

The crystal growth occurs after pyrolysis and catalysis of the compounds close to or on the substrate surface. The growth rate is typically higher than for MBE (1-10 μm/h). As the III-nitride material system is still in its developing stages, there are some technological challenges to be overcome. The challenges can be generalized under two main classifications: (1) material quality, and (2) device design. The issues concerning lack of suitable substrate, high dislocation density, thermodynamic non-equilibrium during growth, phase separation, and p-type doping

have a direct impact on material quality; while challenges pertaining to Ohmic contacts to p-type material and suitable transparent contact have additional consequences on device performance [53].

3.2 Structural Properties of InGaN

3.2.1 Crystal Structure

The natural thermodynamically stable structure for GaN, InN, AlN and its alloys is the hexagonal wurtzite form; however it is possible to grow stable GaN, InN and AIN in the zinc blende structure by utilizing cubic Si, MgO and GaAs as substrates and growing on the (011) plane. Although crystallographic properties of these two structures are very similar there are noticeable differences in their material parameters. A third state is also possible; under high external pressure wurtzite undergoes a phase transformation towards the rock-salt structure. In the present work, we will only focus on wurtzite structures grown along the c-axis, which satisfy the pseudomorphic condition. The wurtzite crystal is characterized by two lattice parameters *a* and *c*, and comprises alternating close-packed planes of Ga (In or Al) and N atoms in (0001) c-planes, forming an ABAB stacking sequence. By close-packed, it is meant that the two planes of adjacent layers are displaced horizontally such that the distance between these two planes is minimized. This stacking sequence forms an anisotropic crystal structure. As a result, the surfaces of the crystals are either of Group III element or N (N-face).

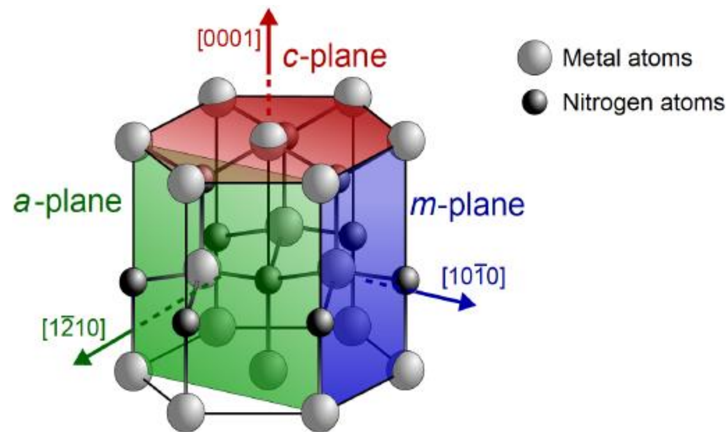

Fig 3.1: WZ structure of III-N compounds for a polar (c-plane) and a non-polar (m- and a-plane) crystal orientations [54]

Owing to its wurtzite hexagonal crystal structure featured by 6 fold rotation and 2 mirror planes, a primitive Bravis lattice containing only one lattice point in the unit cell, and screw 6_2 axis (two step, 60 degrees each) GaN belongs to the point group of 6mm and space group of C^4_{6v} in Hermann-Mauguin and $P6_3mc$ in Schoenflies notation. In Fig. 3.1, a schematic picture of wurtzite III-nitride crystal structure is shown. The c-plane corresponds to the (0001) orientation, the m-plane to the $(10\bar{1}0)$ one and the a-plane to the $(1\bar{2}10)$ one.

Together, the wurtzite III - Nitride materials form a continuous direct bandgap alloy system ranging from 0.9 to 6.2eV, thus allowing the fabrication of light emitting devices which stretch from the infrared, cover the entire visible spectrum and go far into the UV. This alloy system is illustrated in Figure 3.2.

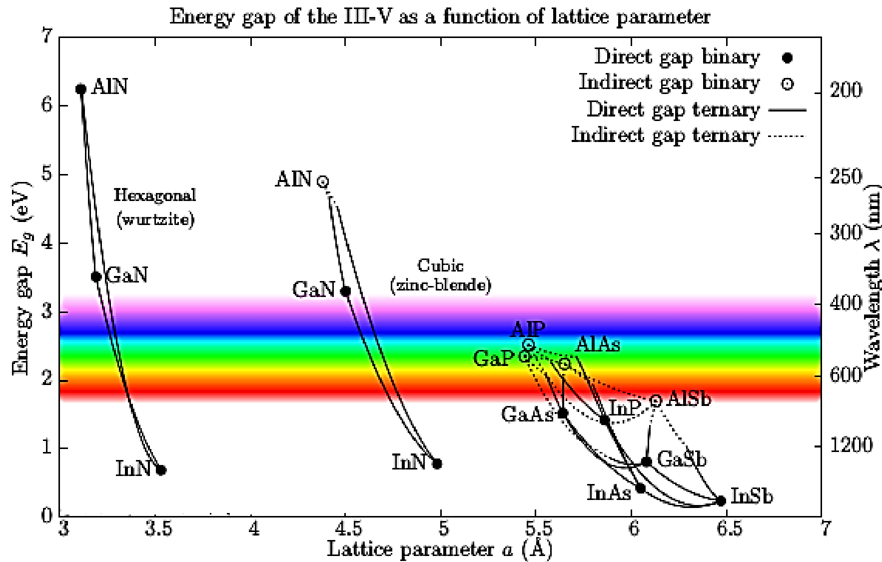

Fig 3.2: The bandgap and lattice constants of Reputed WZ and ZB III-N [55]

In the case of ternary alloys, the Vegard's law can be used to obtain the values of the lattice parameters for a given molar fraction x, i.e., from a simple linear interpolation of the crystal lattice parameter between the binary compounds [56].

$$lM_{1,x}M_{2,1-x}N = x.lM_1N + (1-x).lM_2N \quad (3.1)$$

Here, l is the lattice parameter (c or a) for binary and ternary compounds and M_i one of the different metal atom species amongst Al, Ga and In. This linear approximation is no longer valid when taking into account some structural imperfections of the crystal such as a different

electronegativity between species, a volume deformation in the band structure or even a structural relaxation of the alloys [56]. Therefore, a non-linear bowing term $bx(1 - x)$ should be subtracted to eq. 3.1, where b is known as the bowing parameter. Especially in the III-nitride-based structures, the laser performance is strongly affected by the composition of the individual layers due to issues induced by their unique materials properties. Indeed, the large lattice-mismatch between the different binary compounds (>10% between GaN and InN) and the lack of GaN native substrates produce a large strain through the heterostructure. We may take as an example a QW consisting of an InGaN epilayer embedded between two GaN barriers as shown in Fig 3.3. The QW is under biaxial compression such that its basal plane lattice constant, a, is forced to equal that of the GaN barriers.

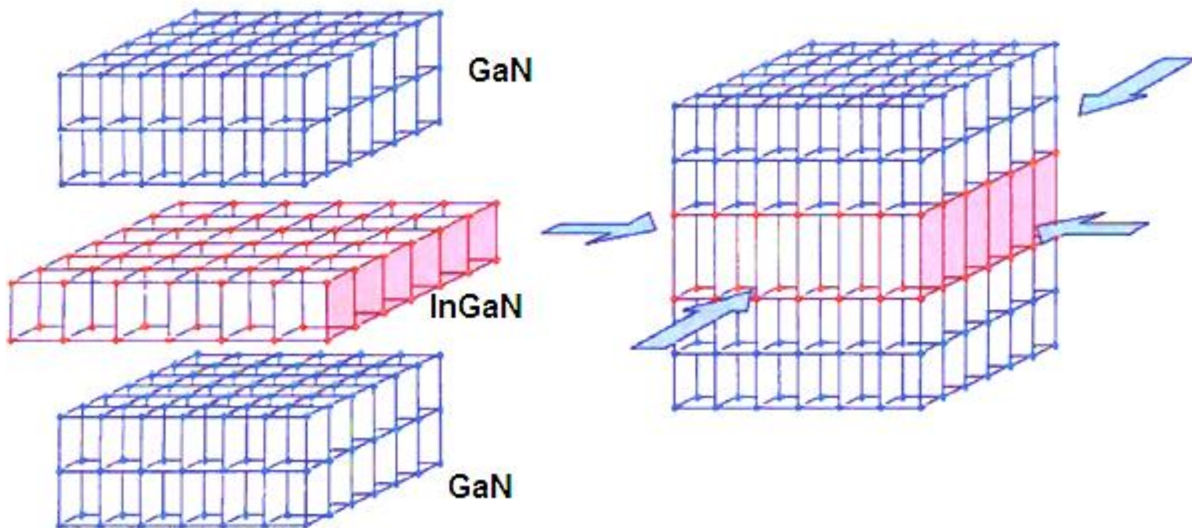

Figure 3.3: Schematic representation of a) separate InGaN epilayer and GaN bulk layers, b) a strained InGaN epilayer embedded between GaN bulk barrier layers

For a sufficiently thin QW it is reasonable to assume that almost all the strain is incorporated within the QW. As the thickness of the QW increases the energy stored per unit area, within the QW, increases at a linear rate [57, 58]. When the energy stored in the QW is equivalent to the energy required to break a line of bonds it will become energetically favorable for the QW to relieve the strain via dislocations. This intrinsic strain will impact the optical characteristics of the heterostructure but can also lead to the formation of a large number of cracks and/or dislocations, especially in the active region, which is detrimental for the performance of optoelectronic devices. Thus there exists a critical thickness below which the strained InGaN

QW can be considered to be dislocation-free and thermodynamically stable. However strain is not the only problem affecting InGaN layers. During growth In atoms are not incorporated in the epilayer swiftly but remain on the surface for long enough periods of time to travel sizable distances (~1 μm), during which time they are able to seek lower energy configuration. This results in composition fluctuations within the QW and the formation of indium rich quantum dots or quantum disks [59]. Strain also affects the valence band structure of the epilayer. The strain breaks the symmetry of the semiconductor and splits the degeneracy of the light hole (LH) and heavy hole (HH) states at the Γ-point. For an InGaN eplilayer under compression the mean energy gap increases and the splitting of the degeneracy at the Γ-point places the HH above the LH. If the epilayer is under tension the bandgap is reduced and the LH moves above the HH.

3.2.2 Polarization Properties

In the III-N system, one of the consequences of the crystal anisotropy discussed in Sec. 3.2.1 results in a static, relative shift of positive and negative charges in the unit cell. Along the c-plane, this asymmetry leads to the appearance of the spontaneous polarization P_{sp} through the crystal lattice, which exists even at equilibrium, i.e., without any external applied field. It is known as the pyroelectric effect. Thus, between the different crystal planes depicted in Fig. 3.1, the c-plane is referred to as the polar one and is generally the growth direction for InGaN-based optoelectronic devices as it is the more stable thermodynamically. In the specific case of ternary alloys, P_{sp} can be obtained by applying again Eq. 3.1 with a specific bowing parameter b [60]. In addition to this polarization effect, an external stress may cause atoms in the unit cell to shift with respect to each other. For example, applying a biaxial strain in the c-plane to any wurtzite III-nitride materials leads to a displacement of the atoms along (0001). Such a shift can lead to further internal polarization known as the piezoelectric effect. In general, the piezoelectric polarization P_{PZ} is coupled to the strain via the tensor e_{ijk} of the piezoelectric coefficients:

$$Ppz,i = \sum_{jk} eijk \cdot \sigma_{jk}, \qquad (3.2)$$

Here, σ_{jk} is the stress-field resulting from a deformation. The total internal polarization P_{int} can be obtained with a simple summation of these two contributions: $P_{int} = P_{sp} + P_{pz}$. In the absence of free charges and considering an infinite interface between the media, the polarization charge satisfies $\nabla \cdot (\varepsilon_r \varepsilon_0 E + P_{int}) = 0$ and is given by:

$$\sigma P = -(Pj - Pi) \cdot n_{ij} \tag{3.3}$$

Here n_{ij} is the surface normal vector pointing from medium i to medium j. The total electric field F in medium i can then be expressed by:

$$Fi = -\frac{\sigma P}{\varepsilon_r \varepsilon_o} n_{ij} \tag{3.4}$$

Here ε_0 is the vacuum permittivity and ε_r is the relative permittivity of medium i. Obviously, the electric field in medium j has the opposite direction. Typically, in a heterostructure the total polarization is not constant between the different constituents. Thus, at the heterointerfaces a charge density develops because of the polarization discontinuity. Free carriers can screen this built-in field in bulk materials but in heterostructures such as QWs this field can have a huge impact on the band structure. The consequences might be an increase in the radiative recombination carrier lifetime, corollary a decrease of the oscillator strength, and a redshift of the transition energies [61].

3.3 Optical Properties of InGaN

In this section, the main optical properties of nitrides are presented such as their energy bandgap and their refractive index. A particular attention will be paid to the QCSE and its impact on the radiative efficiency and transition energy.

3.3.1 Energy Bandgap and Refractive Index

The design of a heterostructure (a key element of any optoelectronic devices) consists in assembling crystalline materials with different bandgaps and refractive indices but with similar lattice constants in order to obtain a pseudomorphic growth. The energy bandgap E_g of III-nitride binary compounds and their alloys hold the interesting property to have a direct bandgap over a broad spectrum of frequency that covers the entire visible spectrum, the near IR, and the deep UV [see Fig. 3.2]. The bandgap is defined as “direct” if the crystal momentum of electrons and holes in the Brillouin zone is the same in both the conduction band and the valence band [e.g., at Γ point]. In direct bandgap semiconductors, band-to-band radiative transitions are highly favorable since momentum will be conserved upon radiative recombination. This means a higher quantum efficiency of the structure.

The direct bandgap of a semiconductor decreases with increasing the temperature and can be accounted for by the Varshni's semi-empirical law [62]:

$$Eg(T) = Eg(T = 0) - \frac{\alpha T^2}{T + \beta} \quad (3.6)$$

where α and β are empirical independent parameters proper to each compound. This behavior is related to the inter-atomic distance. Indeed, the presence of a harmonic potential induces an increase of the lattice constant when increasing the temperature.

The refractive index of wurtzite GaN is commonly measured via spectroscopic ellipsometry. The refractive index of alloys can be experimentally determined directly from the material optical properties. Nevertheless, the refractive index of ternary alloys such as AlGaN and InGaN can also be roughly estimated by shifting the energy scale of the refractive index of GaN, i.e., n GaN (E). The shift thus reads [63]:

$$n_y(E) = nGaN(E - [Eg(y) - Eg(GaN)]), \quad (3.7)$$

where y = $In_xGa_{1-x}N$ or $Al_xGa_{1-x}N$.

The refractive index value in nitrides as in other materials is very important to achieve a proper confinement of light in the active region of a semiconductor. Accurate refractive index values for InGaN and AlGaN materials are required to optimize the LD design by exploiting the approach shown in eq. 3.7. The simplest approach is to consider a model based on harmonic oscillators with Eigen frequencies ν_{eo} that can properly describe the absorption and the optical index of the ensemble of transitions between the valence and conduction bands. The first-order Sellmeier equation accounts for the dependency of the real part of the refractive index on the wavelength λ below the bandgap via [64]:

$$n^2(\lambda) = 1 + E\frac{E_{eo}E_d}{E_{eo}^2 - (h\nu)^2}, \quad (3.8)$$

where E_d is the dispersion energy and E_{eo} is the energy of a single effective oscillator transition with a resonant frequency ν_{eo}. Waves are confined within the waveguide due to total internal reflection occurring at the guide-cladding interfaces (Fig. 3.4) and according to the Snell-Descartes and Fresnel law (n_1- n_2) [65]:

$$n_1 \sin\theta_1 = n_2 \sin\theta_2. \tag{3.9}$$

Figure 3.4: Optical confinement of light rays in a waveguide composed of media 1 and 2

If $n_1 > n_2$, the lightwave in medium 1 is totally reflected for any incident angle lower than a critical angle θ_c. This condition is called total internal reflection and is given by $\theta_c = arc\sin\frac{n_1}{n_2}$.

Unfortunately, not all electromagnetic waves satisfying the later condition will be guided. Indeed, only the reflected waves that remain in phase with the waves produced by previous reflections (each reflection induces φ_r phase shift) can interfere constructively with themselves. This will occur provided that the phase shifts resulting from multiple reflections are integer multiples of 2π and whereby we obtain the self-consistent condition for a confined wave [66]:

$$\frac{2\pi n_1}{\lambda_0} 2d\sin\theta_1 - 2\varphi_r = 2\pi m, \tag{3.10}$$

where λ_0 is the vacuum wavelength of the electromagnetic wave, d is the thickness of the high refractive index material placed in the center of the waveguide and m is the number of multiple reflections. The main advantage of waveguides is to confine light where the materials experience gain.

3.3.2 Strain-induced Quantum Confined Stark Effect (QCSE)

The presence of an electric field in III-V nitride MQWs when grown along the c-axis causes a redshift of the transition energy, which is the so-called quantum confined Stark effect (QCSE). Surface charges σ_{ij} and σ_{ji} with opposite sign appear at the interface between a well of material i and a thick barrier of material j [67]. The resulting total internal field F_{int} in such a single QW reads:

$$F_{int} = \frac{\sigma_{ij} - \sigma_{ji}}{2\epsilon_r \epsilon_0} n_{ij} = \frac{\sigma_{ij}}{\varepsilon_r \varepsilon_0} n_{ij} = \frac{P_i - P_j}{\varepsilon_r \varepsilon_0}, \tag{3.11}$$

where ε_r is the relative permittivity in the well. This electric field F_{int} (in the order of MV/cm) tilts the QW band structure leading to a triangular potential shape. For the sake of illustration, in Fig. 3.5 taken from Ref. [68], the band profile of a single InGaN/GaN QW is shown for growth along the polar [Fig. 3.5 (a)] and non-polar [Fig. 3.5 (c) and (e)] axes. Growth along semi-polar axes offers interesting features as it combines the advantages of both polar and non-polar structures. For instance, depending on the alloy composition and the strain state, semi-polar orientations allow to reduce the internal polarization field F_{int} and so to get rid of the QCSE (similarly to non-polar ones). In addition, it allows for higher indium incorporation in the active region mandatory for applications in the green spectral range. Miller et al. in 1984 first reported on the large shift in optical absorption in GaAs/AlGaAs QWs while experiencing an electric field perpendicular to the layers. According to those authors, exciton resonances remain even for field values much higher than the classical ionization field because of the quantum confinement of carriers in thin semiconductor layers [69, 70]. In III-nitride heterostructures grown along the c-axis, part of the electric field is intrinsic but it can also come from a p-n or p-i-n junction. It is worth mentioning that Miller et al. in a subsequent paper succeeded in correlating the effects observed in the interband optical absorption to an extreme quantization of the so-called Franz-Keldysh effect. This phenomenon was thus described as the quantum confined Franz-Keldysh effect (QCFK). In the present work, quantum effects in the QWs will be mostly ascribed to the QCSE. In nitrides, the first effect of quantum confinement provided by QWs on the optical emission within a triangular-shaped potential concerns the Stark shift. Indeed, the electric field within the QW lowers the QW fundamental transition energy $E_{e_1-hh_1}$ of the electron-hole pairs by a value equal to $-qd_{QW} \| F_{int} \|$ [71]:

$$E_{e_1} - hh_1\left(\frac{h}{2\pi}\omega\right) = E_g + e_1 + hh_1 - E_X^b - qd_{QW}||F_{int}||, \quad (3.12)$$

where E_g is the bandgap energy, e_1 and hh_1 are the confinement energies of the electron and the hole, respectively, E_X^b is the exciton binding energy in a QW and d_{QW} is the QW width.

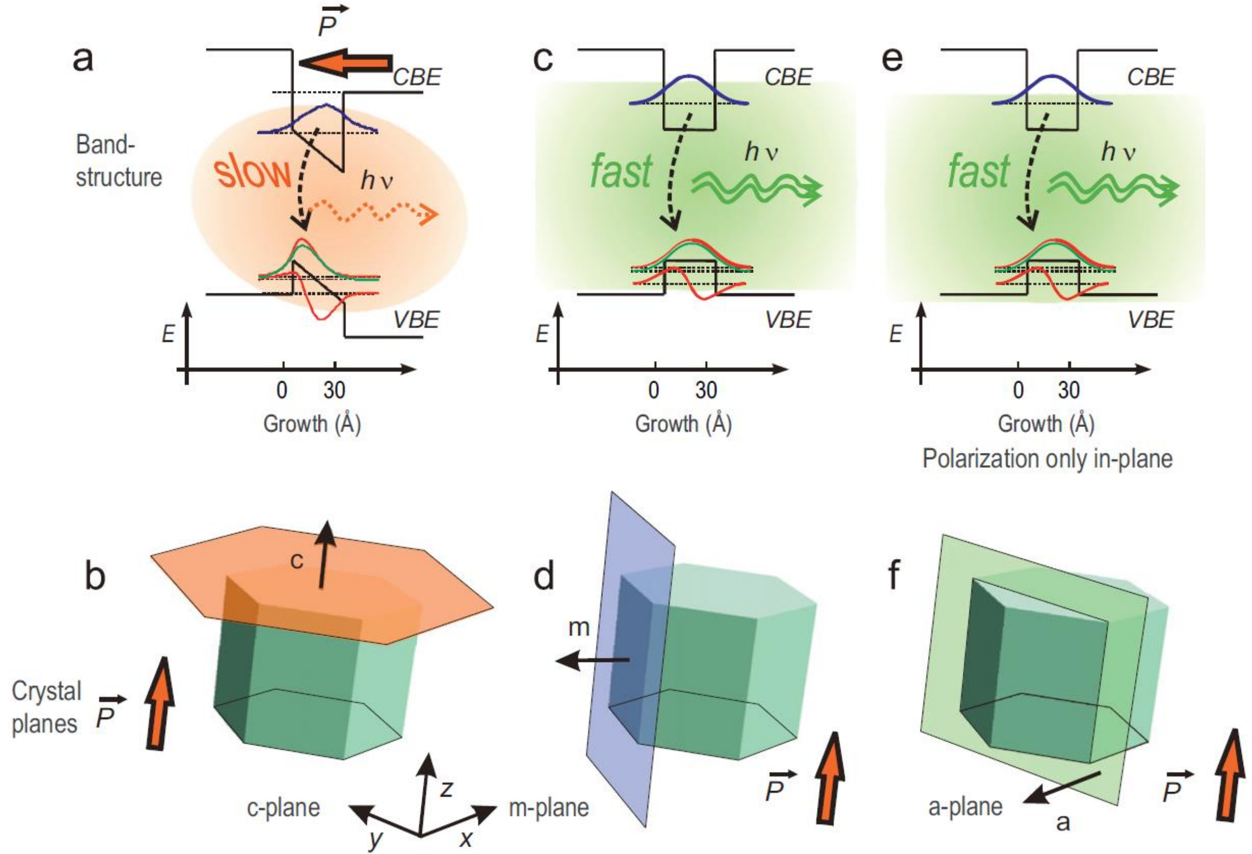

Figure 3.5: Schematic band structure diagram of a single InGaN/GaN QW oriented along different crystal axes (a, c, e). Sketch of QW plane in the hexagonal crystal structure (b, d, f). Situation of polar *c*-axis (a, b), non-polar *m*-axis (c, d), and non-polar *a*-axis growth (e, f). The acronyms CBE and VBE stand for conduction band energy and valence band energy, respectively.

Interestingly, these nitride native triangular-shaped QWs allow to potentially emit below the bulk material bandgap. As d_{QW} increases, the factor $-qd_{QW}$ $||F_{int}||$ further decreases the transition energy leading to $E_{e1}-hh_1< E_g$. For instance, Grandjean et al. reported an emission below the GaN excitonic bandgap emission (3.478 eV at 10 K) already for d_{QW}= 3 nm with F_{int}= 0.71 MV/cm for a GaN/AlGaN QW. Chichibu et al. have stressed how the ratio between the products $d_{QW}||F_{int}||$ and the confinement energy hh_1 (and e_1) for d_{QW} comparable to the Bohr radius a_B

could determine the magnitude of the QCSE on the emission mechanism in InGaN QWs. Furthermore, the triangular-shaped potential induces carrier separation on opposite sides of the well (Fig. 3.5). This translates into a reduction of the overlap between electron and hole wavefunction in the QWs, which induces a reduction in oscillator strength f_{osc} [72]:

$$f_{osc} = \frac{2m_e h w_{if}}{\frac{h^2}{2\pi}} |< i|r \cdot \varepsilon|f >|^2, \tag{3.13}$$

where m_e is the free electron mass , $\frac{h}{2\pi}\omega_{if}$ is the inter band transition energy $i \rightarrow f$ and $|<i|r \cdot \varepsilon|f>|$ $= d_{if}$ is the dipolar matrix element of the optical transition from the initial state $|i>$ to the final state $|f>$, r is the electron momentum operator and e is the unitary polarization vector. In the case of a QW, d_{if} is known to be proportional to the square modulus of the overlap integral between electron and hole wavefunctions f_e and f_h along the growth axis via $|d_{if}|^2 \propto |\int fe(z) fh(z)\, dz|^2$. Thus increasing the thickness of a QW causes a drastic decrease in the wavefunction overlap and therefore increased radiative lifetime τ_{rad} [73]:

$$\tau_{rad} = \frac{2\pi\varepsilon 0 mec3}{n_g q^2 w_{if}^2 f_{osc}}, \tag{3.14}$$

where n_g is the group refractive index. This process is depicted in Fig. 3.5 with the notation "slow" ("fast"). Note that the QW internal quantum efficiency η_i can be written as $\eta_i = \frac{\tau_{nrad}}{\tau_{nrad}+\tau_{rad}}$, i.e., the amount of injected carriers that recombine radiatively divided by the total carrier recombinations, where τ_{nrad} is the non-radiative carrier lifetime. In conclusion, the influence of the QCSE on a GaN-based QW depends on both the well width and the strength of the polarization field. On one side, quantum confinement in narrow QWs provides an efficient confinement for the carriers even in the presence of a high electric field across the heterostructure. On the other side, the existence of a built-in field F_{int} in polar structures implies triangular-shaped QWs. It will break the symmetry of the wavefunctions by pushing electrons and holes toward opposite sides of the well and as a consequence the radiative recombination efficiency will drop compared with non-polar structures (see Fig. 3.5). The thicker the QWs and the higher the internal field, the stronger the QCSE. It is therefore crucial to minimize the impact of the QCSE to achieve high performance optoelectronic devices.

3.4 Electrical Properties of InGaN

High electrical conductivity is essential for optoelectronic devices. Thus, one of the most important technological challenges in semiconductor technology is *doping*, i.e., the controlled incorporation of impurities in a pure intrinsic semiconductor to enhance its electrical conductivity. These impurities can have electronic energy levels within the forbidden gap of the bulk host material, preferably close to the band edges. Before recombining in the active region, carriers (electrons and holes) are injected on opposite sides of the device and pass through several layers. Transport of holes requires the layer to be *p*-type doped (i.e., doped with acceptors) whereas transport of electrons requires *n*-type doping (doping achieved with donors). Typical impurity concentrations used for doping range from 10^{15} to 10^{20} cm^{-3}. In this section, the main features of doping and *p-n* junction in InGaN are presented. In particular, the impact of an electric field (internal and/or external) is detailed.

3.4.1 n-type doping

If no special care is taken III-nitride epilayers exhibit a tendency to be n-type: the electron background concentration is about ~10^{17} cm^{-3}. Nowadays, the origin of non-intentionally doped (NID) InGaN layers is likely due to impurities such as oxygen or silicon rather than nitrogen vacancies or any other types of native defects [74, 75]. The most commonly used donor impurity for achieving intentional n-type doping of III-nitrides is silicon (noted GaN:Si) [76]. In MOVPE, silicon doping is achieved by flowing gaseous silane (SiH_4) during growth. The activation energy of Si in GaN is about 17 meV for a donor concentration $N_D = 3*10^{17}$ cm^{-3}. This means that all donor impurities are ionized at RT. When increasing the doping concentration beyond $N_D = 1*10^{20}$ cm^{-3}, a dramatic degradation in the crystal quality occurs and besides an impurity band may develop. Moreover, such high doping concentrations result in a degenerate system: electrons populate states within the conduction band which shift the Fermi level higher than the CBE. This is the so-called Burstein-Moss effect. In terms of electron mobility, the maximum value amounts to 1425 $cm^2V^{-1}s^{-1}$ for $N_D = 1.76*10^{16}$ cm^{-3} at RT.

Other possible donor sources for nitrides less often used are for example oxygen and germanium that exhibit an activation energy of 29 meV for $N_D = 1*10^{18}$ cm^{-3} and 19 meV for $N_D = 3*10^{17}$ cm^{-3}, respectively. In both cases, the ionization energy is sensitive to the concentration of the dopant [77].

3.4.2 p-type doping

The most common and efficient p-type dopant is currently magnesium. In MOVPE, magnesium doping is achieved by flowing a bis-cyclopentadieny magnesium precursor (Cp_2Mg) during growth. However, in III-nitrides p-type doping has always been difficult to achieve. An efficient acceptor should indeed possess three main characteristics: (i) stability against compensation by other configurations of the acceptor dopant (e.g., hydrogen passivation), (ii) high solubility and (iii) low ionization energy. Possible candidates are: Ca, Zn, Be and Mg. Magnesium is up to date the only acceptor which approaches all these criteria. Actually, in MOVPE-growth Mg-doped layers are highly resistive because of the formation of Mg-H complexes that are electrically inactive. A post-growth process that allows breaking Mg-H bonds and thus overcoming this hydrogen passivation is therefore required. Amano et al. in 1989 reported the first successful p-doping by using magnesium as dopant and applying an activation process based on low-energy electron-beam irradiation (LEEBI). Afterwards, Nakamura et al. demonstrated that a thermal annealing in N_2 ambient could also activate Mg impurities. The conductivity is the product of dopant concentration by their mobility but unfortunately obtaining both a high hole mobility and a high hole concentration is challenging. Indeed, a high hole concentration can be obtained but at the expense of a strong degradation of the mobility due to material defects and scattering (i.e., a high resistivity is observed). Indeed, the solubility limit of Mg in GaN is quite low (in the range of ~10^{19} cm^{-3}) [78, 79].

In conclusion, the limit of Mg acceptor concentration and the deep acceptor energy level of Mg dopants limit the conductivity of p-type GaN layers, which can hinder the performance of optoelectronic devices.

3.4.3 p-n junction:

Most of optoelectronic devices are based on semiconductor materials in which a p-n junction is included. Therefore, they are considered bipolar devices in contrast to unipolar ones like, e.g, the QW lasers. Thus, the junctions are commonly used as diodes: circuit elements that allow a flow of current in one direction but not in the opposite direction. The characteristics of an abrupt p-n junction at thermodynamic equilibrium are depicted in Fig. 3.6. A p-n junction is composed of a doped p-type semiconductor and a doped n-type semiconductor in contact. In the junction a depletion region (or also called space charge region) forms. The transport properties are

determined by the recombination of the minority carriers while the depletion region collapses. These minority charge carriers can be trapped in one or multiple thin layers with a lower bandgap than the surrounding material in order to enhance their recombination and increase their local density. In this subsection, the creation and the subsequent control of these charge carriers will be analyzed.

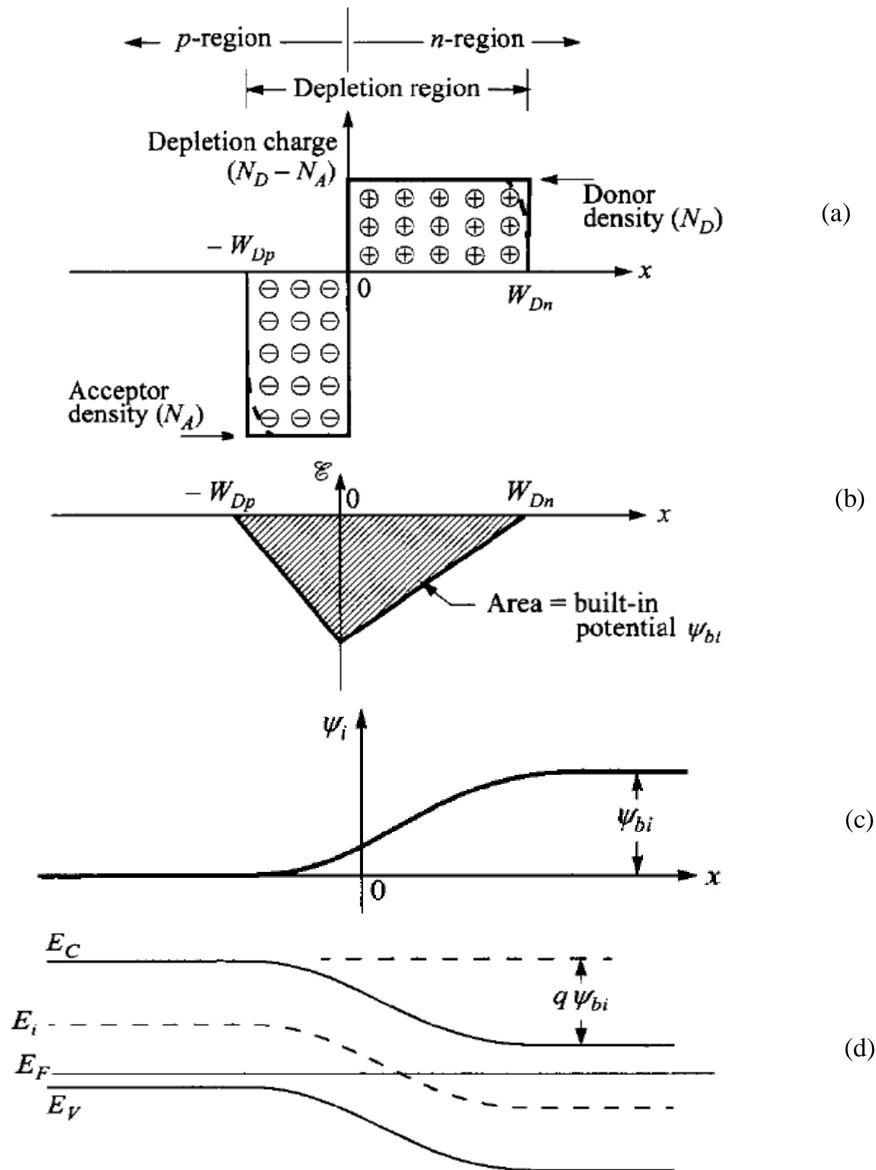

Figure 3.6: Abrupt p-n junction in thermal equilibrium adapted from Ref. [51]. (a) Space charge distribution. The dashed lines indicate corrections to the depletion approximation. (b) Electric field distribution. (c) Potential distribution where Ψ_{bi} is the built-in potential. (d) Energy band diagram. At equilibrium the Fermi level E_F is the same on both sides. However, by applying an external electric field, the Fermi level splits in two distinct quasi-Fermi levels.

An abrupt junction consists in a junction over which the doping changes from *n* to *p* over a very short distance. So, when contacting the doped layers, diffusion current appears due to the difference in charge carrier concentration. The electrons diffuse from the *n*-region to the *p*-one and conversely for the holes. The regions nearby the *p-n* interface lose their neutrality and become charged forming a *depletion region*, where the charge carrier concentration is orders of magnitude lower than the fixed charge concentration given by ionized acceptors and donors. At thermal equilibrium, the electric field is zero at the boundaries of the depletion region. Therefore, the electrostatic potential Ψ_{bi} created by this space charge region is opposed to the diffusion process for both electrons and holes and produces a drift electric field. The total drift and diffusion current is given by the equation [80, 81]:

$$J_i = \underbrace{q\ \mu_i\ i\ \mathbf{E}}_{drift} + \underbrace{q\ D_i\ \nabla i}_{diffusion} = \mu_i\ i\ \frac{dE_F}{dx} \tag{3.13}$$

At thermodynamic equilibrium, the drift current exactly compensates the diffusion current. This equilibrium leads to a well-defined space charge region $W_D = W_{Dn} + W_{Dp}$ across the junction, which extends mostly on the lowest doped region. Consequently, the charge separation implies the presence of a built-in potential Ψ_{bi}:

$$q\Psi_{bi} = E_g \ - \ k_B T \ln \frac{N_v N_c}{N_A N_D} \tag{3.14}$$

The width of the depletion layer W_D is given by:

$$W_D = \sqrt{\frac{2\varepsilon_r\varepsilon_0}{q}\frac{N_A+N_D}{N_A N_D}(\Psi_{bi} - V - d_{QW}F_{int})}$$

where F_{int} is the total internal polarization field.

In the specific case of a p-i-n junction (where a lightly doped region is placed within the junction) the depletion region width reads:

$$W_D = -d_u + \sqrt{d_u^2 \ + \ \frac{2\varepsilon_r\varepsilon_0}{q}\frac{N_A+N_D}{N_A N_D}(\Psi_{bi} - V - d_{QW}F_{int})} \quad ; d_u = \text{width of intrinsic region}$$

The application of an external bias V to this structure simply acts as a simple metal plate capacitor with a constant electric field in the intrinsic region:

$$F_{ext} = \frac{\Psi_{bi} - V - d_{QW} F_{int}}{d_u + W_D/2} \tag{3.15}$$

Total net-field applied across heterojunction: $F_{QW} = F_{ext} + F_{int}$

3.5 Overview on Polar, Non-polar and Semipolar Orientation

As known, the planes of a hexagonal lattice can be represented by four indices *h,k,i,l* as in (*h*, *k*, *i*, *l*). Having a constraint between indices *i.e.* $h + k + i = 0$, one can write each plane of (*h*,*k*,*i*,*l*) in hexagonal system as a unique (*h*,*k*,*i*) in a cubic system. There are certain relations governing these indices that define general properties of the corresponding planes. For instance, $h = k = i = 0$, $l \neq 0$ defines *c*-plane giving rise to sets of parallel planes with interplanar distance that is determined by index *l* only. As will be demonstrated later in this subsection, these planes are polar planes as a result of unequal numbers of N atoms and Ga atoms in the double monolayer plane. In case in addition to nonzero *l* index any of the *h* or *k* indices being nonzero, the plane is featured by reduced spontaneous and dubbed by convention as "semipolar". If $l = 0$, the plane is featured by zero polarization field and termed as a "nonpolar" plane. As examples for this general rule, planes (0001), $(10\bar{1}0)$, and $(10\bar{1}1)$ represent polar c-plane, nonpolar m-plane, and semipolar s-plane crystallographic planes, respectively.

The first attempts to grow GaN on its non-polar planes were not successful and it was impossible to achieve a working device performance due to their low crystal quality. Several substrate materials were studied to achieve high crystal quality non-polar GaN material. In one of the first successful attempts, Craven *et. al.* reported device-quality a-plane GaN on r-plane sapphire and a-plane SiC. However, the threading dislocation densities were still high (~10^{10} cm^{-2}). Among the proposed methods to further reduce the dislocation densities and improving materials quality were growing a thick (~100μm) buffer layer, epitaxial lateral overgrowth and using a high temperature nucleation layer. Although there are additional difficulties on the growth of such materials in their semipolar planes, LEDs and LDs based on semi-polar GaN have been successfully demonstrated.

It turns out that the characteristics are dependent on tilt angle of a plane with respect to polar axis. This inclination angle (θ) *i.e.* the angle between a plane of interest (*h*,*k*,*i*,*l*) and the *c*-plane can be determined from the four indices and lattice constants with the following relationship:

$$\theta = \cos^{-1}(\frac{\sqrt{3}al}{\sqrt{(4c^2(h^2+k^2+hk)+3a^2l^2)}})$$

Where *a* and *c* are in-plane and out of plane lattice parameters of the hexagonal structure, respectively. Some of the semipolar and nonpolar planes and the calculated value for the inclination angles are shown in Figure 3.7 [36, 37]. The distance between the parallel planes of a given orientation which can be calculated having *h*, *k* and *l* indices using a three- dimensional (3-D) geometrical method is unique for a certain orientation and so is the Bragg angle. Thus, XRD analysis using the following relation can be used to identify the orientations:

$$n\lambda = 2d\sin\Theta$$

Where, Θ is the Bragg angle, λ is the incident x-ray wavelength, *n* is an integer and *d* is the inter-planar distance in the orientation. Therefore, one to one correspondence of each set of plane with a certain inclination angle (θ) and corresponding Bragg angle (Θ) resolved by XRD could act as a fingerprint identifying the orientations of a film for a single or multiple phase layers.

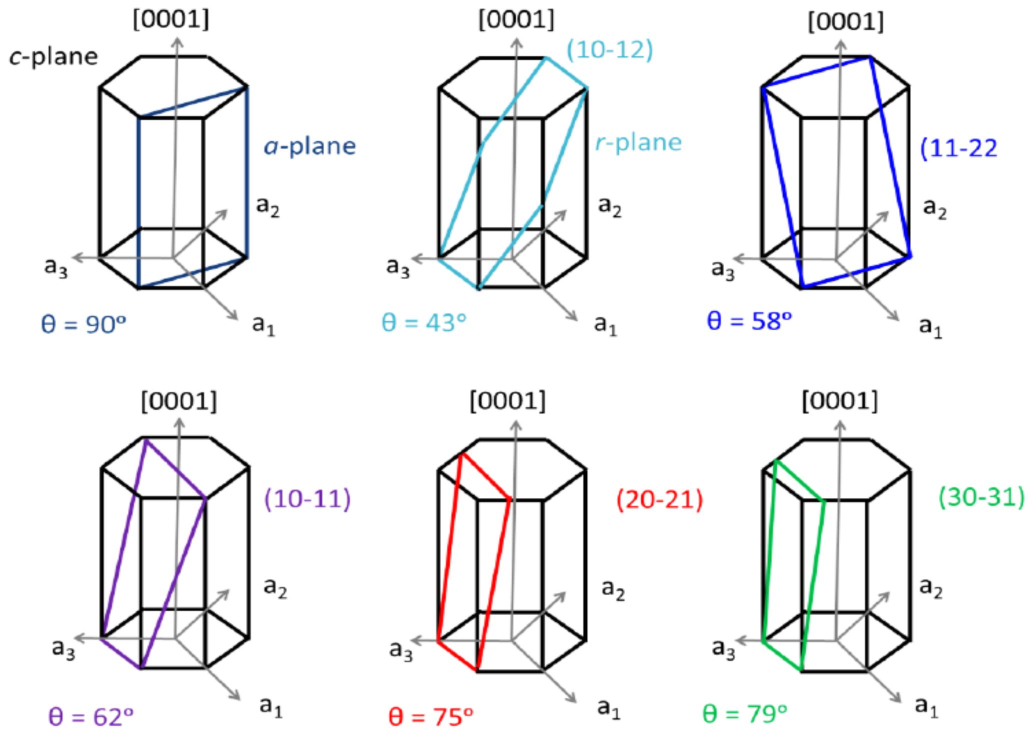

Fig 3.7: Schematic Representation of some of the nonpolar, semipolar and polar planes for Wurtzite Crystal

As seen above, for a crystallographic orientation of interest, the inclination angle important in identifying characteristics and the corresponding properties of the particular plane. The properties of heterostructures such as strain, polarization charge, carrier dynamics and transports, optical activities, impurity and alloy incorporations, etc. depend on their orientation. This means that the corresponding parameters for the properties are variable under rotation of epilayer orientation with respect to c-axis. Due to the reduced or eliminated polarization effect in their quantum heterostructures, optoelectronic devices grown on non- and semi-polar planes are of special interest to scientific community and the industry [82].

CHAPTER IV

Proposed Laser Structure and Mathematical Model

This section describes the physical structure and mathematical model of strain and crystal orientation dependent electrical and optical properties of InGaN/GaN Single QW blue laser. In order to analyze electronic band structure, one dimensional Schrödinger equations for conduction and valence bands are solved by finite difference method. A MATLAB/Simulink equivalent circuit model is discussed for the proposed QW laser structure in order to analyze output power characteristics and frequency response.

4.1 Proposed QW Blue LD Structure

Figure 4.1 shows the proposed QW LD structure used in the present study. The active layer of the device is an $In_{0.17}Ga_{0.83}N/GaN$ single QW (SQW) structure consisting of 10nm thick Si doped barriers and 8nm thick undoped well layers. The structure is also composed of n and

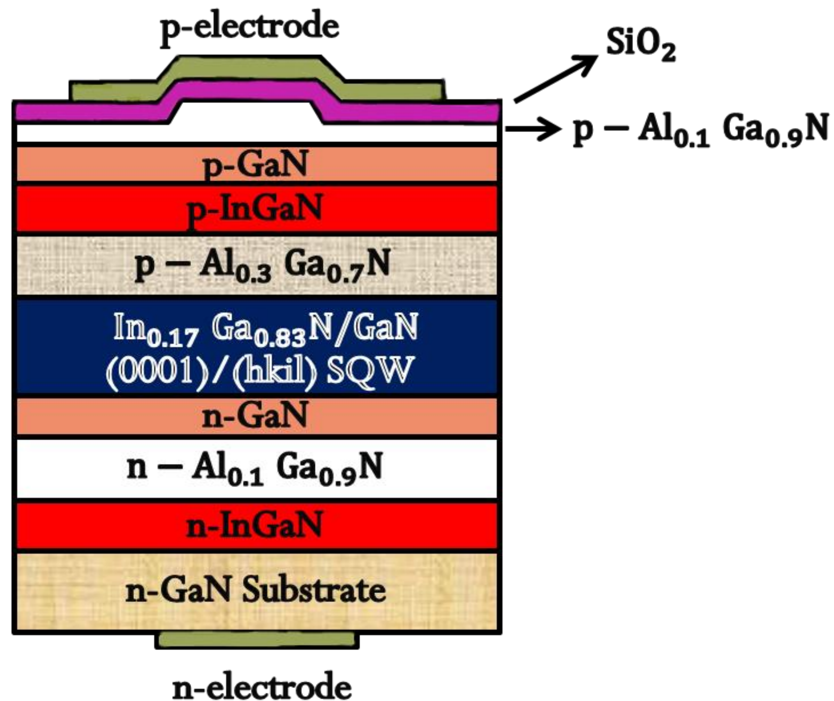

Fig. 4.1: Structure of proposed InGaN/GaN QW Blue Laser

p-type InGaN buffer layer with a view to maintain low spontaneous emission, n and p-type $Al_{0.1}Ga_{0.9}N$ top/bottom cladding layer to confine carrier spillover, n and p-type GaN top/bottom optical guiding layer and a p-type $Al_{0.3}Ga_{0.7}N$ evaporation-prevention layer. All the layers are grown on GaN substrate. Above the upper AlGaN layer, an oxide aperture is used for current and index confinement. Highly doped contact layers are grown at the top and the bottom of the surface for the formation of ohmic contact [83]. In arbitrary crystal orientated LD structure, the crystal orientation in the active region is changed arbitrarily but all other layers are in (0001) crystal orientation. The interface of (0001) and (hkil)-oriented layer is joined via wafer bonding technique [84].

4.2 Modeling of Electronic Energy Bands

To understand the optical properties of the proposed laser structure, we have to know the electronic energy bands dispersion profile. Strain, crystal orientations and piezoelectric field are the key parameters that can modify the electronic band structure. Mathematical formulations of energy band structure including the effect of strain, change in crystal orientations and piezoelectric field are given below.

4.2.1 Conduction band dispersion profile

Conduction band dispersion profile is assumed to be parabolic in our calculation. One dimension Schrödinger equation is used for finding discrete energy levels of QW LD [85]. The one dimension Schrödinger equation for conduction band is given below:

$$\left[\frac{-h^2}{2m^*_e}\frac{d^2}{dz^2} + v_e(z)\right]\psi_n(z) = E_e(k_t = 0)\psi_n(z) \tag{4.1}$$

where $\psi_n(z)$ conduction band wave function, $\hbar$ Planck's constant divided by 2π, m_e^* effective mass of the electron, E_e electron energy level, k_t inplane wave vector, and $v_e(z)$ is the conduction band potential which can be given by:

$$v_e = \begin{cases} a_{cz}\varepsilon_{zz} + a_{ct}(\varepsilon_{xx} + \varepsilon_{yy}) & |z| \le \frac{L_w}{2} \\ \Delta v_e & |z| \ge \frac{L_w}{2} \end{cases} \tag{4.2}$$

where, L_w is the QW length, a_{cz} and a_{ct} is the conduction band deformation potential along the c axis and perpendicular to the c axis, ε_{ij} are the principal strain components, Δv_e is the conduction band offset in barrier layer. We take $a_{cz} = a_{ct}$ for simplicity.

Finite difference discretization of equation (1) is

$$\frac{-h^2}{2m_e^*}\left(\frac{\psi_{i+1} - 2\psi_i + \psi_{i-1}}{\Delta z^2}\right) + v_i\psi_i = E_e(k_t = 0)\psi_i \tag{4.3}$$

In our analysis, total active region L is divided into number of sections for computational purpose. If the number of node is N, then spacing between nodes is determined by, $\Delta z = L/(N-1)$. The boundary condition in the present study is $\psi(z) = 0$ for outside the well and barrier regions. The index i can be varied from $i = 1$ to $i = N-1$. Equation (3) can be written as

$$\frac{-\hbar^2}{2m_e^*\Delta z^2}[\psi_2 - 2\psi_1 + \psi_0] + v_1\psi_1 = E_e\psi_1 \tag{4.4}$$

$$\frac{-\hbar^2}{2m_e^*\Delta z^2}[\psi_3 - 2\psi_2 + \psi_1] + v_2\psi_2 = E_e\psi_2, \tag{4.5}$$

and

$$\frac{-\hbar^2}{2m_e^*\Delta z^2}[\psi_N - 2\psi_{N-1} + \psi_{N-2}] + v_{N-1}\psi_{N-1} = E_e\psi_{N-1} \tag{4.6}$$

for $i = 1,2,....(N-1)$, respectively. Outside the well and barrier regions the wave functions ψ_0 and ψ_N are equal to zero. The resulting Hamiltonian matrix in the present case can be given by

$$H_c = \frac{-\hbar^2}{2m^*_e\Delta z^2}\begin{bmatrix} -2 & 1 & 0 & 0 & 0 & 0 & 0 \\ 1 & -2 & 1 & 0 & 0 & 0 & 0 \\ 0 & 1 & -2 & 1 & 0 & 0 & 0 \\ 0 & 0 & 1 & -2 & 1 & 0 & 0 \\ 0 & 0 & 0 & 1 & -2 & 1 & 0 \\ 0 & 0 & 0 & 0 & 1 & -2 & 1 \\ 0 & 0 & 0 & 0 & 0 & 1 & -2 \end{bmatrix} + \begin{bmatrix} v_1 & 0 & 0 & 0 & 0 & 0 & 0 \\ 0 & v_2 & 0 & 0 & 0 & 0 & 0 \\ 0 & 0 & v_3 & 0 & 0 & 0 & 0 \\ 0 & 0 & 0 & v_4 & 0 & 0 & 0 \\ 0 & 0 & 0 & 0 & v_5 & 0 & 0 \\ 0 & 0 & 0 & 0 & 0 & v_6 & 0 \\ 0 & 0 & 0 & 0 & 0 & 0 & v_{N-1} \end{bmatrix} \tag{4.7}$$

Conduction band energies and corresponding wave vectors are evaluated by finding the Eigen-values and Eigen-vectors of the Hamiltonian matrix. The conduction band energy dispersion relation can be written as [86]:

$$E(k) = \frac{\hbar^2}{2}\left(\frac{{k_x}^2+{k_y}^2}{{m_e}^t} + \frac{{k_z}^2}{{m_e}^z}\right) + {E_c}^0 \tag{4.8}$$

where the band-edge energy is given by:

$${E_c}^0 = \Delta_1 + \Delta_2 + E_g$$

Δ_1 is the crystal-field-split energy; Δ_2 and Δ_3 account for the spin-orbit interaction. The conduction-band wave function of a bulk wurtzite semiconductor is of the form:

$$\Psi(r) = \sum_{j=W,B} \exp(ik_\perp r)\, u_c^j(r) f_n(z)$$

Here, Wand B represent the well and barrier materials, $u_c^j(r)$ is the conduction-band zone-center Bloch wave function, $f_n(z)$ is a slowly varying envelope function, $k_\perp$ is the transverse (in-plane) wave vector, and the growth direction is along the z axis.

4.2.2 Valence band dispersion profile

The valence band structure for (0001) orientation is solved in the envelope approximation using a six-band RSP (Rashba-Sheka-Pikus) **k.p** Hamiltonian. The 6×6 Hamiltonian matrix H for (0001) WZ crystals can be asserted by [85]:

$$H\Psi_h(z) = E\Psi_h \tag{4.9}$$

The full Hamiltonian for can be written as:

$$H(k,\varepsilon) = \begin{bmatrix} F & -K* & -H* & 0 & 0 & 0 \\ -K & G & H & 0 & 0 & \Delta \\ -H & -H* & \lambda & 0 & \Delta & 0 \\ 0 & 0 & 0 & F & -K & H \\ 0 & 0 & \Delta & -K* & G & H \\ 0 & \Delta & 0 & H* & -H & \lambda \end{bmatrix} \begin{matrix} |u_1\rangle \\ |u_2\rangle \\ |u_3\rangle \\ |u_4\rangle \\ |u_5\rangle \\ |u_6\rangle \end{matrix} \tag{4.10}$$

$$\Psi_h(z) = \begin{bmatrix} \phi_{\frac{3}{2},\frac{3}{2}}(z) \\ \phi_{\frac{3}{2},\frac{1}{2}}(z) \\ \phi_{\frac{1}{2},\frac{1}{2}}(z) \\ \phi_{\frac{3}{2},\frac{-3}{2}}(z) \\ \phi_{\frac{3}{2},\frac{-1}{2}}(z) \\ \phi_{\frac{1}{2},\frac{-1}{2}}(z) \end{bmatrix} = \begin{bmatrix} g^{(1)}(z) \\ g^{(2)}(z) \\ g^{(3)}(z) \\ g^{(4)}(z) \\ g^{(5)}(z) \\ g^{(6)}(z) \end{bmatrix}$$

Where, ϕ_{j,m_j} or $g^{(j)}$ is the valence band wave function component [3/2, ±3/2 for Heavy Hole, 3/2, ±1/2 for light hole and 1/2, ±1/2 for spin-orbit split-off hole] and E is the energy of three valence bands.

The matrix elements are:

$F = \Delta_1 + \Delta_2 + \lambda + \theta$

$G = \Delta_1 - \Delta_2 + \lambda + \theta$

$\Delta = \sqrt{2}\,\Delta_3$

$\lambda = \frac{\hbar^2}{2m_0}[A_1 k_z^2 + A_2 (k_x^2 + k_y^2)] + D_1 \varepsilon_{zz} + D_2(\varepsilon_{xx} + \varepsilon_{yy})$

$\theta = \frac{\hbar^2}{2m_0}[A_3 k_z^2 + A_4 (k_x^2 + k_y^2)] + D_3 \varepsilon_{zz} + D_4(\varepsilon_{xx} + \varepsilon_{yy})$

$K = \frac{\hbar^2}{2m_0} A_5 (k_x + ik_y)^2 + D_5 (\varepsilon_{xx} - \varepsilon_{yy})$

$H = \frac{\hbar^2}{2m_0} A_6 (k_x + ik_y) k_z + D_6 (\varepsilon_{zx} + i\,\varepsilon_{yz})$

Here the Ai's are the valence-band effective-mass parameters, which are similar to the Luttinger parameters in a zinc blende crystal; the Di's are the deformation potentials for wurtzite crystals; k_i is the wave vector; ε_{ij} is the strain tensors; Δ_1 is the crystal-field-split energy; Δ_2 and Δ_3 account for the spin-orbit interaction. For $\Delta_1 > \Delta_2 > 0$, the three bands from top to bottom are labeled as HH, LH, and CH, respectively. The basis functions are shown in Fig. 4.2.

$$
\left.
\begin{aligned}
|u_1\rangle &= -\frac{1}{\sqrt{2}}\langle (X + iY)\uparrow\rangle \\
|u_2\rangle &= \frac{1}{\sqrt{2}}\langle (X - iY)\uparrow\rangle \\
|u_3\rangle &= \langle Z\uparrow\rangle \\
|u_4\rangle &= \frac{1}{\sqrt{2}}\langle (X - iY)\downarrow\rangle \\
|u_5\rangle &= -\frac{1}{\sqrt{2}}\langle (X + iY)\downarrow\rangle \\
|u_6\rangle &= \langle Z\downarrow\rangle
\end{aligned}
\right\}
$$

Here, |X>, |Y> and |Z> are the p_x, p_y and p_z wavefunctions at the Γ point with their dipoles along the c, a and m plane.

Fig. 4.2 Basis Function for the Hamiltonian

The energy dispersion profile along (0001) orientation is derived as a function of k for the six band **k.p** theory by diagonalizing the Hamiltonian of Eq. 4.9 using numerical finite difference scheme as discussed in previous section.

4.2.3 Orientation-dependent Energy Band

Conduction band in non-(0001) orientation is almost the same as in a c-plane QW because the electron effective mass is nearly isotropic and the angular momentum Eigen function of the electrons is the spherically symmetric *S*-function. On the other hand, the hole band parameters and the strain of WZ crystals are strongly anisotropic. Therefore, the crystal orientation has a major impact on the valence band structure of an InGaN quantum well.

If the active region is grown on arbitrary crystal orientation, the wave vectors on (0001) crystal can be obtained by the following expression [87]:

$$\begin{pmatrix} k_1 \\ k_2 \\ k_3 \end{pmatrix} = O_R \begin{pmatrix} k_x \\ k_y \\ k_z \end{pmatrix} \tag{4.11}$$

where, k_x, k_y, k_z are the wave vectors along *(hkil)* direction.

The following expression of the rotation matrix is used to obtain the Hamiltonian for arbitrary crystal orientation [88]:

$$O_R = \begin{pmatrix} cos\theta cos\emptyset & -sin\emptyset & sin\theta cos\emptyset \\ cos\theta sin\emptyset & cos\emptyset & sin\theta sin\emptyset \\ -sin\theta & 0 & cos\theta \end{pmatrix} \tag{4.12}$$

Where,

$$\theta = \cos^{-1}\left(\frac{\sqrt{3}al}{\sqrt{4c^2(h^2+k^2+hk)+3a^2l^2}}\right) \quad \text{and} \quad \emptyset = \tan^{-1}\frac{ik}{h}$$

Here, *a* and *c* are in-plane and out of plane lattice parameters of the hexagonal structure, respectively.

The rotation of the Euler angles θ and Ø transforms physical quantities from (x,y,z) coordinates to (x',y',z') coordinates. We consider only the inclination angle θ dependence of physical quantities in the following due to the hexagonal symmetry. The z axis corresponds to the c axis (0001), and the growth axis z' is normal to QW plane (hkil) as shown in Figure 4.3.

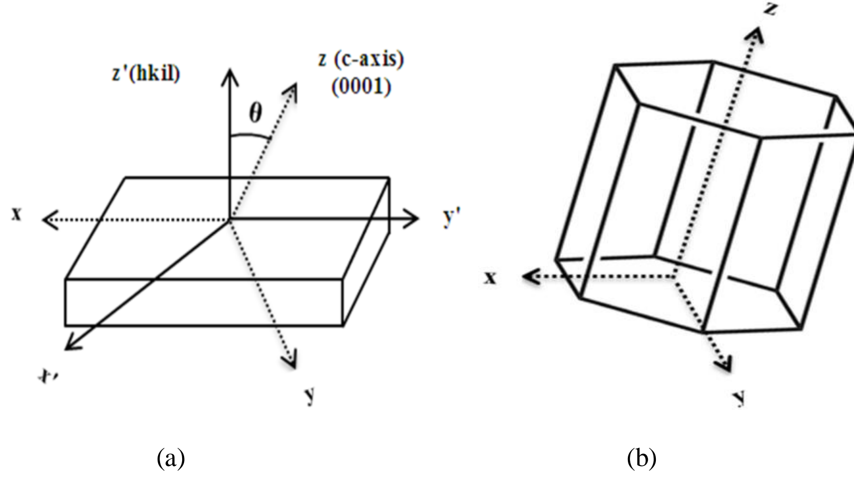

Fig. 4.3: (a) Configuration of the coordinate systems (x',y',z') in (hkil)-oriented crystals. (b) The coordinate system in a wurtzite primitive cell. The angle θ is defined as the angle between the growth direction z' and the c axis

The strain coefficients in the (x,y,z) coordinates for a general crystal orientation are determined from the condition that the layer is grown pseudomorphically, and these strain coefficients should minimize the strain energy of the layer simultaneously. The strain tensor ε depends on the inclination angle θ (crystal angle) of the growth plane to the c-plane as follows [89]:

$$\varepsilon_{xx} = \varepsilon_{xx}{}^{(0)} + \varepsilon_{xz} tan\theta$$

$$\varepsilon_{yy} = \varepsilon_{xx}{}^{(0)}$$

$$\varepsilon_{zz} = \varepsilon_{zz}{}^{(0)} + \varepsilon_{xz} cot\theta$$

$$\epsilon_{xz} = -\frac{\left(\left(c_{11} + c_{12} + c_{13}\frac{\epsilon_{zz}^{(0)}}{\epsilon_{xx}^{(0)}}\right)\sin^2\theta + \left(2c_{13} + c_{33}\frac{\epsilon_{zz}^{(0)}}{\epsilon_{xx}^{(0)}}\right)\cos^2\theta\right)\epsilon_{xx}^{(0)}\cos\theta\sin\theta}{c_{11}\sin^4\theta + 2(c_{13} + 2c_{44})\sin^2\theta\cos^2\theta + c_{33}\cos^4\theta} \tag{4.13}$$

with $\varepsilon_{xx}{}^{(0)} = \frac{a_{well} - a_{barrier}}{a_{barrier}}$ and $\varepsilon_{zz}{}^{(0)} = \frac{c_{well} - c_{barrier}}{c_{barrier}}$. The other strain coefficients are zero. Here, c_{ij} are the elastic stiffness constant of the strained layer.

Using the wave vector and strains in the (0001) crystal orientation, the Hamiltonian matrix for (0001) crystal orientation can be calculated according to previous section. Then the Hamiltonian matrix in *(hkil)* orientation can be calculated by the following equation [90]:

$$H^{(hkil)} = UH^{(0001)}U^* \tag{4.14}$$

The transformation matrix U is defined as [89]:

$$U = \begin{bmatrix} \alpha^* & 0 & 0 & \alpha & 0 & 0 \\ 0 & \beta & 0 & 0 & \beta^* & 0 \\ 0 & 0 & \beta^* & 0 & 0 & \beta \\ \alpha^* & 0 & 0 & -\alpha & 0 & 0 \\ 0 & \beta & 0 & 0 & -\beta^* & 0 \\ 0 & 0 & -\beta^* & 0 & 0 & \beta \end{bmatrix} \tag{4.15}$$

Here,

$\alpha = \frac{1}{\sqrt{2}} e^{i(3\pi/4)}$ and $\beta = \frac{1}{\sqrt{2}} e^{i(\pi/4)}$

Hence we obtain a 6×6 Hamiltonian in the (x',y',z') coordinates by substituting the transformation relations for the wave vector k and the strain coefficients for a general crystal orientation into the Hamiltonian (4.10) for the (0001) orientation.

4.2.4 Energy Band Change Due to Piezoelectric Field

The piezoelectric polarization in the (x,y,z) coordinates for a general crystal orientation is given by [91]:

$$\begin{pmatrix} P_x \\ P_y \\ P_z \end{pmatrix} = \begin{pmatrix} 0 & 0 & 0 & 0 & d_{15} & 0 \\ 0 & 0 & 0 & d_{15} & 0 & 0 \\ d_{31} & d_{31} & d_{33} & 0 & 0 & 0 \end{pmatrix} \begin{pmatrix} c_{11} & c_{12} & c_{13} & 0 & 0 & 0 \\ c_{12} & c_{11} & c_{13} & 0 & 0 & 0 \\ c_{13} & c_{13} & c_{33} & 0 & 0 & 0 \\ 0 & 0 & 0 & c_{44} & 0 & 0 \\ 0 & 0 & 0 & 0 & c_{44} & 0 \\ 0 & 0 & 0 & 0 & 0 & c_{66} \end{pmatrix} \begin{pmatrix} \varepsilon_{xx} \\ \varepsilon_{yy} \\ \varepsilon_{zz} \\ 0 \\ 2\varepsilon_{xz} \\ 0 \end{pmatrix} \tag{4.16}$$

where the strain coefficients in the (x,y,z) coordinate for a general crystal orientation is given in previous section. We then obtain the polarization components along *x, y*, and *z* axes:

$$P_x = 2d_{15}c_{44}\varepsilon_{xz}$$

$$P_y = 0$$

$$P_z = [d_{31}(c_{11} + c_{12}) + d_{33}c_{13}](\varepsilon_{xx} + \varepsilon_{yy}) + [2d_{31}c_{13} + d_{33}c_{33}]\varepsilon_{zz}$$

The normal polarization with respect to the growth plane (along the growth direction) can be obtained by taking the scalar product between the polarization vectors **P** in the (x,y,z) coordinates and the unit vector $\widehat{\boldsymbol{z}'}$ shown in Fig. 4.2 [92]:

$$P'_z = \mathbf{P}.\widehat{\boldsymbol{z}'} = P_x sin\theta + P_z cos\theta + (P_{SP}{}^{QW} - P_{SP}{}^{b})cos\theta \tag{4.17}$$

Similarly, we can obtain the parallel polarization on the growth plane:

$$P'_x = \mathbf{P}.\widehat{\boldsymbol{x}'} = P_x cos\theta - P_z sin\theta$$
$$P'_y = 0$$

Here, P_{SP} is the spontaneous polarization.

If there are no external charges, the electric field reduces to growth direction z only.

The internal electric fields in the barrier and QW can then be estimated by assuming appropriate boundary conditions and applying the Gauss law [93]:

$$\varepsilon^{QW} E_z^{QW} - \varepsilon^b E_z^b = -\frac{P'_z}{\varepsilon_0} \tag{4.18}$$

Here, ε_0 is the permittivity of vacuum; $\varepsilon^{(b)}$ and $\varepsilon^{(QW)}$ are the static dielectric constants for the barrier layers and the quantum well, respectively.

From the QCSE theory, the energy shift due to piezoelectric field for quantum well structure can be given by [94].

$$\Delta E = C \frac{m^* e^2 E_z^2 L^4}{\hbar^2} \quad ; C = \frac{1}{8}\left(\frac{1}{3} - \frac{2}{\pi^2}\right)^2 \tag{4.19}$$

where $L =$ Quantum well length and m^* is the mass of electron or hole.

Then the energy band profiles are changed due to piezoelectric field can be given by [94]

$E_c = E_c(E_z = 0) + \Delta E^c$ and $E_h = E_h(E_z = 0) + \Delta E^h$. Here, E_c and E_h are the energy of electron and hole respectively.

4.3 Momentum Matrix Element and Optical Gain Profile

The optical gain as a function of energy for quantum well structures can be expressed by [95]:

$$g(E) = \frac{2q^2\hbar}{n\mathcal{E}_0 c m_0{}^2 LE} \times \sum_{n,m} \int_0^\infty \frac{\frac{k_t M_{nm}(k_t)\Gamma}{2\pi}}{(E_{cn}(k_t) - E_{kpm}(k_t) - E)^2 + (\Gamma/2\pi)^2} (f_c{}^n - f_v{}^m) d\, k_t \tag{4.20}$$

Here, q is denoted as free electron charge, $\hbar$ is the reduced Planck constant, n is the index of refraction, $\mathcal{E}_0$ is the free space dielectric constant, c is the speed of light, E is the photon energy, E_{cn} is the conduction band energy, E_{kpm} is the mth valence sub-bands, and M_{nm} is the momentum matrix element in strained quantum well architecture. $\Gamma = \hbar/\tau$ where, τ is the photon relaxation

time. f_c and f_v are the Fermi levels of conduction and valence bands. Fermi functions for the conduction band and valence bands are [86]:

$$f_c^{\,n}(k_t) = \frac{1}{1 + \exp\{[\;E_c^{\,n}(k_t) + (m_r / m_e^{*})(E - (E_{cn}(k_t) - E_{kpm}(k_t))) - F_c\,]/KT\;\}} \tag{4.21}$$

$$f_v^{\,m}(k_t) = \frac{1}{1 + \exp\{[\;E_{kpm}(k_t) - (m_r / m_h^{*})(E - (E_{cn}(k_t) - E_{kpm}(k_t))) - F_v\,]/KT\;\}} \tag{4.22}$$

where F_c, F_v are the quasi-Fermi levels of conduction and valence bands. In carrier density-dependent quasi-Fermi levels calculation, it is considered that the injected carrier is electron. The expressions of quasi-Fermi levels can be given by [86]:

$$F_c = E_{c1}(k_t = 0) + KTIn\left(\frac{N_{inj} + n_i}{N_c}\right) \tag{4.23}$$

$$F_v = E_{kp1}(k_t = 0) - KTIn\left(\frac{N_{dop} + n_i}{N_v}\right) \tag{4.24}$$

where E_{c1} and E_{kp1} are the first conduction and valence band energy at band edge, N_{inj} is the injected carrier density, N_{dop} is the p-type doping density in the well, n_i is the intrinsic carrier density, N_c and N_v are the density of state of electron and hole for the QW material.

In a QW structure, the optical momentum matrix element will depend on the TE and TM polarization of the optical electromagnetic field. The momentum matrix element for TE and TM polarization can be written as [96]:

$$\mathrm{M_{nm}(k_t)[TE]} = \frac{3}{4}\left[\left\langle \Psi_{n(k_t=0)} \middle| g_m{}^{(1)} \right\rangle^2 + \frac{1}{3}\left\langle \Psi_{n(k_t=0)} \middle| g_m{}^{(2)} \right\rangle^2\right] \mathrm{M_b}^2 \tag{4.25}$$

$$\mathrm{M_{nm}(k_t)[TM]} = \left\langle \Psi_{n(k_t=0)} \middle| g_m{}^{(2)} \right\rangle^2 \mathrm{M_b}^2 \tag{4.26}$$

M_b is the bulk average crystal momentum matrix that can be noted by (E_g=band gap and Δ=split off band separation):

$$M_b = (\frac{m_0}{m_e^*} - 1)\frac{m_0 E_g (E_g + \Delta)}{6(E_g + \frac{2}{3}\Delta)} \quad (4.27)$$

Using the expressions for the band-edge wave functions and energy of the conduction and valence bands and transformation relations, the polarization-dependent interband momentum-matrix elements of (4.25) and (4.26) can be illustrated as follows [87]:

$$\mathrm{M_{nm}(k_t)[TE]} = -\frac{1}{\sqrt{2}} g^{(1)} \alpha^* cos\theta \left(\frac{m_0 P_2}{\hbar}\right) + \frac{1}{\sqrt{2}} g^{(2)} \beta cos\theta \left(\frac{m_0 P_2}{\hbar}\right) - g^{(3)} \beta^* cos\theta \left(\frac{m_0 P_1}{\hbar}\right) \quad (4.28)$$

$$\mathrm{M_{nm}(k_t)[TM]} = -\frac{1}{\sqrt{2}} g^{(1)} \alpha^* sin\theta \left(\frac{m_0 P_2}{\hbar}\right) + \frac{1}{\sqrt{2}} g^{(2)} \beta sin\theta \left(\frac{m_0 P_2}{\hbar}\right) + g^{(3)} \beta^* cos\theta \left(\frac{m_0 P_1}{\hbar}\right) \quad (4.29)$$

As seen, the above analytical results include the crystal orientation dependence. Here,

$$P_1^2 = \frac{\hbar^2}{2\mathrm{m_0}} (\frac{m_0}{m_e^*} - 1) \frac{(E_g + \Delta_1 + \Delta_2)(E_g + 2\Delta_2) - 2\Delta_3^2}{E_g + 2\Delta_2}$$

$$P_2^2 = \frac{\hbar^2}{2\mathrm{m_0}} (\frac{m_0}{m_e^*} - 1) \frac{E_g[(E_g + \Delta_1 + \Delta_2)(E_g + 2\Delta_2) - 2\Delta_3^2]}{(E_g + \Delta_1 + \Delta_2)(E_g + \Delta_2) - \Delta_3^2}$$

Substituting $E = E_1, E_2,$ and E_3, we can obtain moment matrix element for the interband optical transitions between the conduction band and the heavy hole, light hole, and crystal-field split-off hole bands, respectively.

4.4 Output Power Characteristics

When analyzing a Laser Diode in an application context, the first thing that comes to concern is the relationship between optical output power and the diode drive current. And this has been dictated by rate equations. Due to the variety in the category of laser diode and mathematical models, one could find many different forms of laser diode rate equations throughout the literatures. In this thesis, Two-level rate equations that account for carriers in the active and SCH, or barrier layers is applied to find P-I response in different crystal orientation.

This accounts for carriers in the SCH, or barrier, layers. A single nonnegative solution regime exists for nonnegative injection currents. The model equations, based on those found in [97], are

$$\frac{dN_b}{dt} = \frac{\eta_i I}{qV_{barr}} - R_b\,(N_b) - \frac{N_b}{\tau_{capt}} + \frac{N_w V_{act}}{V_{barr}} \frac{N}{\tau_{em}} \quad (4.30)$$

$$\frac{dN}{dt} = \frac{V_{barr}}{N_w V_{act}} \frac{N_b}{\tau_{capt}} - \frac{N}{\tau_{em}} - R_w(N) - \Gamma_c v_{gr} \frac{\alpha(N)}{\phi(S)} S \quad (4.31)$$

$$\frac{dS}{dt} = -\frac{S}{\tau_p} + N_w R_{w\beta}(N) + N_w \Gamma_c v_{gr} \frac{\alpha(N)}{\phi(S)} S \quad (4.32)$$

$$\frac{S}{P_f} = \frac{\lambda \tau_p}{\eta_c V_{act} hc} = \vartheta \quad (4.33)$$

Here, Equation (4.30) is the rate equation for carrier density N_b in the SCH (Separate Confinement-Heterostructure) layer and relates its rate of change to the injection current I, the SCH recombination rate, and the carrier exchange between the SCH layers and QW's, namely the rate of carrier capture and emission by the QW's. Equation (4.31) accounts for the carrier exchange between the SCH layers and QW's, with capture rate of carriers from the SCH layer and a new term N/τ_{em} for carrier emission from the QW's. Equations (4.32) and (4.33) are for photon density and power.

Carrier dependent gain $\alpha(N) = G_0 \ln(\frac{R_w(N)}{R_w(N_0)})$

Gain Saturation $\phi(S) == 1/(1 + \varepsilon \Gamma_c S)$

QW Recombination Rate $R_w(N) = AN + BN^2 + CN^3$

SCH Recombination Rate $R_b(N_b) = A_b N_b + B_b {N_b}^2 + C_b {N_b}^3$

Here, A, B and C are unimolecular, radiative and Auger recombination coefficient.

Photon lifetime is calculated using the expression: $\tau_p^{-1} = v_{gr}[\alpha_i + \frac{\ln(\frac{1}{R_m})}{L_c}]$ (4.34)

Here, α_i= internal cavity loss, R_m = mean reflectivity and L_C= cavity length

Output power coupling coefficient is determined using: $\eta_c = 0.5 \ln\left(\frac{1}{R_m}\right) / [\alpha_i L_c + \ln\left(\frac{1}{R_m}\right)$ (4.35)

This Laser Diode Model only simulates the first two operation regions of a Laser Diode, which are spontaneous emission of photons region and linear stimulated emission region as shown in Fig. 4.4. Material parameters used for evaluating output optical power characteristics are shown in table 4.1. Some of the parameters from rate equations have crystal orientation dependency which is shown in the table 4.2.

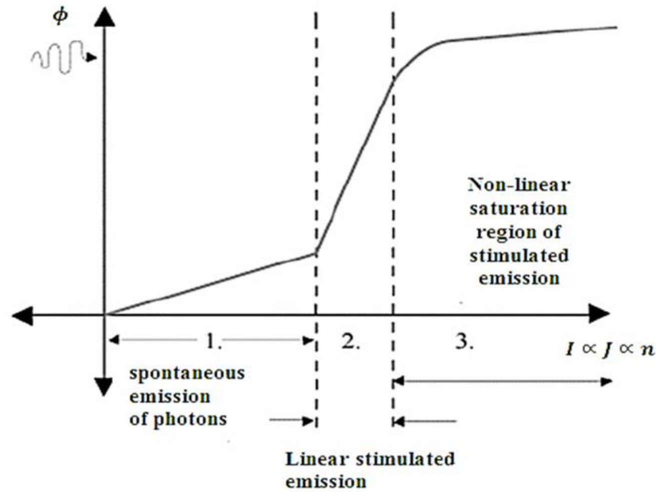

Fig 4.4: Full operating region of Laser Diode

Table 4.1

Material parameters used for evaluating output optical power characteristics [98-101]

Name	Symbol(unit)	Value
Current-injection efficiency	η_i	0.86
No. of QW	N_W	1
Volume of one QW	V_{act} (m^3)	$4*10^{-19}$
Optical confinement factor (mean value)	Γ_c	0.025
Output power coupling coefficient	η_c	0.51
QW Unimolecular recombination rate coefficient	A_W (s^{-1})	$1.0*10^8$
Auger recombination rate coefficient	C_W(cm^{-6} s^{-1})	$1.8*10^{-31}$
SCH unimolecular recombination rate coefficient	A_b (s^{-1})	$1.2*10^8$
Phenomenological gain-saturation term	ε	$5*10^{-17}$
Unimolecular recombination coupling term	β_A	0
Radiative recombination coupling term	β_B	$1*10^{-4}$
Auger recombination coupling term	β_C	0
Volume of SCH	V_{barr} (m^3)	$3*10^{-17}$
QW capture lifetime	τ_{cap} (ps)	1.1
QW emission lifetime	τ_{em} (ps)	6
Internal loss of the cavity	α_i	$42cm^{-1}$
Mean mirror reflectivity	R_m	0.995
Cavity length	L_c (μm)	200

Table 4.2

Crystal orientation-dependent parameters from the rate equations

Crystal Orientation-dependent Parameter	Comments
Lasing wavelength λ	Since energy band gap will change with crystal orientation, so does lasing wavelength $\lambda=1.24/E_g$
Gain coefficient G_o and optical transparency density N_o	The value of G_o and N_o will be evaluated from the carrier density-dependent optical gain and peak gain vs. Lasing wavelength λ curve in different crystal orientation
Group Velocity v_{gr}	Since $v_{gr} = \frac{3\times10^8}{N_g}$ and group index N_g depends on lasing wavelength λ, so it has orientation dependency.
Photon lifetime τ_p	From Equ. (4.34), it depends on v_{gr}. So photon lifetime has orientation dependency.

Two-level rate equations model is constructed in Simulink based on Ref. [102]. With I as input parameter from a signal generator and S, N, N_b, and P_f as output parameters. All the parameters in the rate equations can be modified before the simulation starts. The method used to transform the equations into a signal-flow diagram is borrowed from the field of analog computation – the equations were *mechanized* into a model that gives numerical solutions for arbitrary inputs and time scales that are of interest. The Simulink design is shown in Fig. 4.5.

The ramp input signal is applied to the first input of the sum on the top left corner. It sums up with the pumping current to form the electrical impulse of the Laser Diode. The components connected with the bigger sum in the upper part simulate the rate equation for carrier density in active and SCH layers. So we could capture the output of the carrier density from the end of these two blocks. Photon Density output comes from the output of the lower block connected with the lower bigger sum. It is also been converted to power output in watts.

The simulation was run over a time period that was several orders of magnitude longer than the turn-on transient effects that happen near threshold, to avoid the oscillatory behavior in both $N(t)$ and $S(t)$ in this region. All simulations used a standard 4th-order Runge-Kutta algorithm with a fixed step size of 1ps as an equation solver.

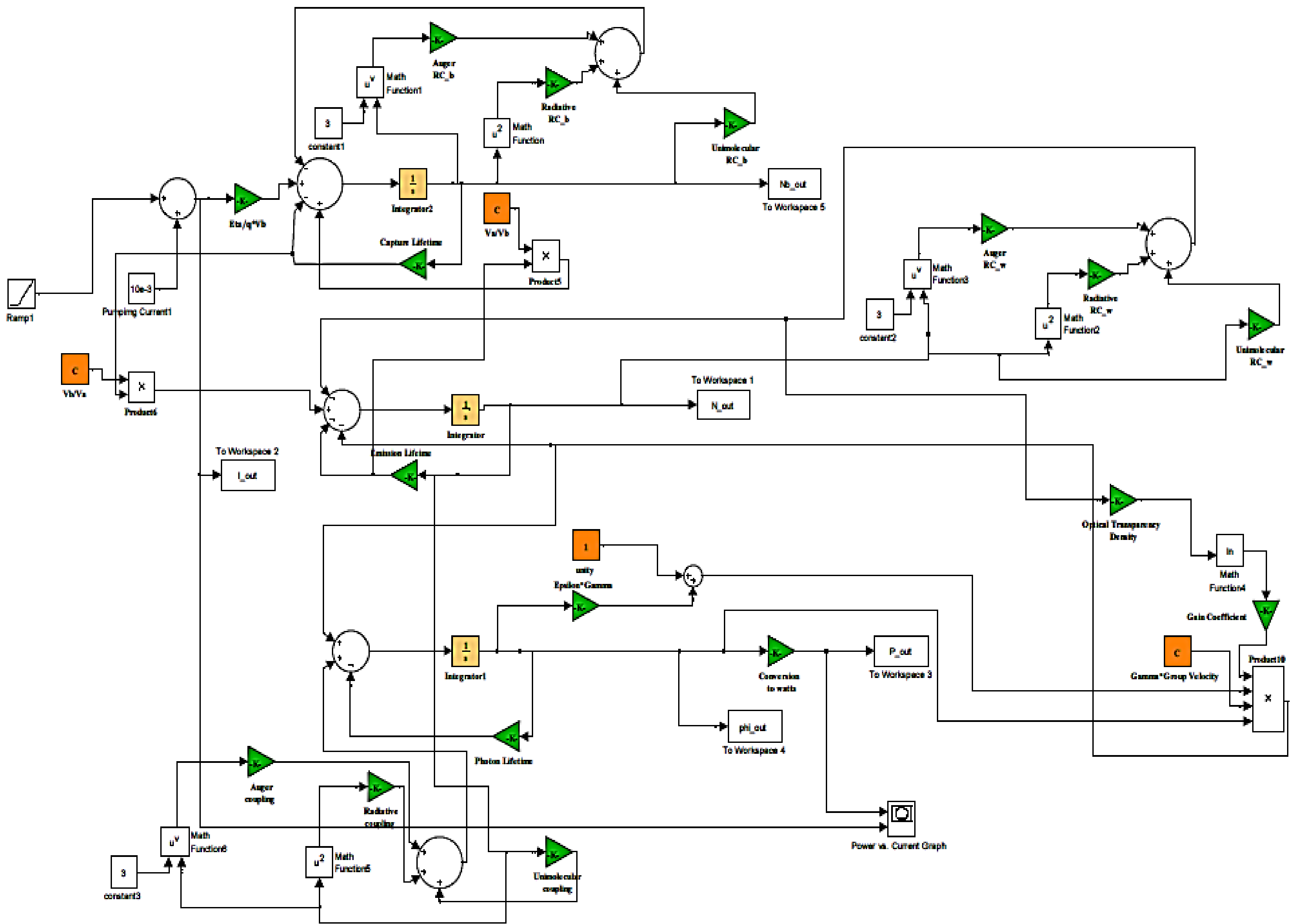

Fig 4.5: Simulink Model for Output Power-Current Response from InGaN Laser

4.5 Frequency Response Analysis

In order to obtain values to simulate the frequency response, the non-linear rate equations were linearized by taking the partial derivative of each time-dependent term with respect to photon and electron density. It is this new model that allows the results of the P-I response to be used in simulating the frequency response [102].

The process was as follows: Choose an arbitrary operating point close to the threshold, such that the gain saturation term $\phi(S)$ will approach 1. This term will have negligible effect on Equ. 4.31

And Equ. 4.32. So partial derivatives with respect to $N_b(t)$, $N(t)$, $S(t)$ can safely be taken to construct a state-space model.

$$\frac{\partial(dN_b/dt)}{\partial N_b} = \frac{-1}{\tau_{capt}} - (A_b + 2B_bN_{bop} + 3C_bN_{bop}^2)$$

$$\frac{\partial(dN_b/dt)}{\partial N} = \frac{V_{act}}{V_{barr} * \tau_{em}}$$

$$\frac{\partial(dN_b/dt)}{\partial S} = 0$$

$$\frac{\partial(dN/dt)}{\partial N_b} = \frac{V_{barr}}{V_{act} * \tau_{capt}}$$

$$\frac{\partial(dN/dt)}{\partial N} = \frac{-1}{\tau_{em}} - \left(A + 2BN_{op} + 3CN_{op}^2\right) - \Gamma_c v_{gr} Q S_{op}$$

$$\frac{\partial(dN/dt)}{\partial S} = -\Gamma_c v_{gr} G_0 \ln(\frac{AN_{op} + BN_{op}^2 + CN_{op}^3}{R_w(N_0)})$$

$$\frac{\partial(dS/dt)}{\partial N_b} = 0$$

$$\frac{\partial(dS/dt)}{\partial N} = \left(\beta_A A + 2\beta_B BN_{op} + 3\beta_C CN_{op}^2\right) + \Gamma_c v_{gr} Q S_{op}$$

$$\frac{\partial(dS/dt)}{\partial S} = \frac{-1}{\tau_p} + \Gamma_c v_{gr} G_0 \ln(\frac{AN_{op} + BN_{op}^2 + CN_{op}^3}{R_w(N_0)})$$

$$Q = \frac{G_0 S}{AN_{op} + BN_{op}^2 + CN_{op}^3}(A + 2BN_{op} + 3CN_{op}^2)$$

The final result is the following state-space model:

$$\begin{bmatrix} \dot{N}_b \\ \dot{N} \\ \dot{S} \end{bmatrix} = \begin{bmatrix} \frac{\partial\left(\frac{dN_b}{dt}\right)}{\partial N_b} & \frac{\partial\left(\frac{dN_b}{dt}\right)}{\partial N} & \frac{\partial\left(\frac{dN_b}{dt}\right)}{\partial S} \\ \frac{\partial\left(\frac{dN}{dt}\right)}{\partial N_b} & \frac{\partial\left(\frac{dN}{dt}\right)}{\partial N} & \frac{\partial\left(\frac{dN}{dt}\right)}{\partial S} \\ \frac{\partial\left(\frac{dS}{dt}\right)}{\partial N_b} & \frac{\partial\left(\frac{dS}{dt}\right)}{\partial N} & \frac{\partial\left(\frac{dS}{dt}\right)}{\partial S} \end{bmatrix} \begin{bmatrix} N_b \\ N \\ S \end{bmatrix} + \begin{bmatrix} \frac{\eta_i}{qV_{barr}} \\ N \\ S \end{bmatrix} I \tag{4.35}$$

$$y = [0\ 0\ 1]\begin{bmatrix} N_b \\ N \\ S \end{bmatrix}$$

where, S_{op}, N_{op} and N_{bop} indicate the respective steady-state photon and electron densities (QW/SCH) for an arbitrary bias current.

CHAPTER V

Simulation Results and Discussion

Following the theoretical analysis presented in chapter-4 the performances of the proposed WZ InGaN-based QW blue laser structure are evaluated as a function of strains(related PZ field) and crystal orientation using the parameters listed in table-5.1. In the present work, compressive strain is chosen because compressive strain in the well enhances the optical gain. The compositions of well materials are selected as $In_{0.15}Ga_{0.85}$ N, $In_{0.17}Ga_{0.83}$ N, $In_{0.19}Ga_{0.81}$ N and $In_{0.21}Ga_{0.79}$ N. Higher values of Indium (In) composition are neglected in this thesis as the emission wavelength shifts towards "Green" from "Blue" range and physical structure of the device degrades with higher values of strain. The optical and electrical properties of $In_{0.17}Ga_{0.83}$ N/GaN QW are investigated in (0001), $(10\bar{1}0)$, $(10\bar{1}2)$, $(11\bar{2}2)$ and $(10\bar{1}1)$ crystal orientations. The effect of piezoelectric field on the optical gain of the proposed laser structure is also investigated. Furthermore, the output power characteristics of the proposed laser are determined using SIMULINK modeling.

TABLE 5.1

Material Parameters for Blue Laser [1]

Parameters	GaN	InN
Lattice Constant(A^0)		
a	3.189	3.544
c	5.185	5.718
Refractive Index n	2.29	3.2
Energy parameters		
E_g at 300K(eV)	3.44	0.7
Δ_1(meV)	21	17
Δ_{so}(meV)	11	3
$\Delta_2 = \Delta_3 = \Delta_{so}/3$(meV)	3.67	1
Valence band effective mass parameters		
A_1	-7.24	-15.803
A_2	-0.51	-0.497
A_3	6.73	15.251
A_4	-3.36	-7.151
A_5	-3.35	-7.060
A_6	-4.72	-10.078

Deformation Potentials(eV)		
D_1	-4.08	-3.62
D_2	0.7	-4.60
D_3	2.1	2.68
D_4	1.4	1.74
D_5	-0.7	-2.07
D_6	-0.7	-2.07
Elastic Stiffness Constant (GPa)	375	225
C_{11}	140	110
C_{12}	115	95
C_{13}	385	200
C_{33}	120	45
C_{44}		
Piezoelectric Constant(C/m^2)		
e_{33}	0.65	0.43
e_{31}	-0.33	-0.22
e_{15}	-0.33	-0.22
Spontaneous Polarization (C/m^2)		
P^{sp}	-0.029	-0.032
Unimolecular recombination rate coefficient (s^{-1})		
A	1×10^8	1
Radiative recombination rate coefficient (cm^{-3} s^{-1})		
B	1.1×10^{-8}	2.0×10^{-10}
Auger recombination rate coefficient (cm^{-6} s^{-1})		
C	1.4×10^{-31}	-

[1] I. Vurgaftman, J.R.Meyer and L.R.Ram-Mohan, "Band parameters for III-V compound semiconductors and their alloys", *J. Appl. Phys. 89*, 5815 (2001).

The peak emission wavelength of laser mainly depends on the band gap energy of the material used in active region. So, the selection of composition of the semiconductor material used in the active region and barrier layer is very important. In this structure InGaN is used in the active region and GaN is used in the barrier of QW. The bandgap of InGaN is calculated using the following formulae:

$$E_g\ (In_xGa_{1-x}\ N)\ (eV)\ =\ 0.7x + 3.44(1-x) - 1.43x(1-x)$$

The other parameters such as lattice constant, deformations potentials etc. are calculated using Vagard's law.

5.1 Crystal Orientation-dependent Strain and Polarization field

The main purpose of growth on crystal planes with a different orientation than the commonly used c-plane is the reduction of the internal electric fields and related QCSE. The dominant contribution to the internal fields comes from the piezoelectric polarization of the quantum wells,

which is a function of the strain of these layers. The strain tensor depends on the inclination angle θ (crystal angle) of the growth plane to the c-plane. Figure 5.1 shows the components of the strain tensor as functions of the crystal angle for 15%, 17%, 19% and 21% Indium composition. It can be seen that, with increasing indium composition, the magnitude of strain increases. Here, the component ε_{yy} is constant (-0.016) and independent of inclination angle θ as realized from eq. 4.13. The component ε_{xz} is zero for the (0001) and $(10\bar{1}0)$ orientation (θ=0° & 90°). For 0°< θ <90°, a strong modification of the strain tensor elements is observed so that $\varepsilon_{xx} \neq \varepsilon_{yy}$. The strain components ε_{xx} and ε_{zz} show a maximum at θ=0° and θ=90°. The crystal orientation dependence of the bands is determined mainly by these strain components. The polarization discontinuity along the growth direction z' can be calculated from the strain tensors.

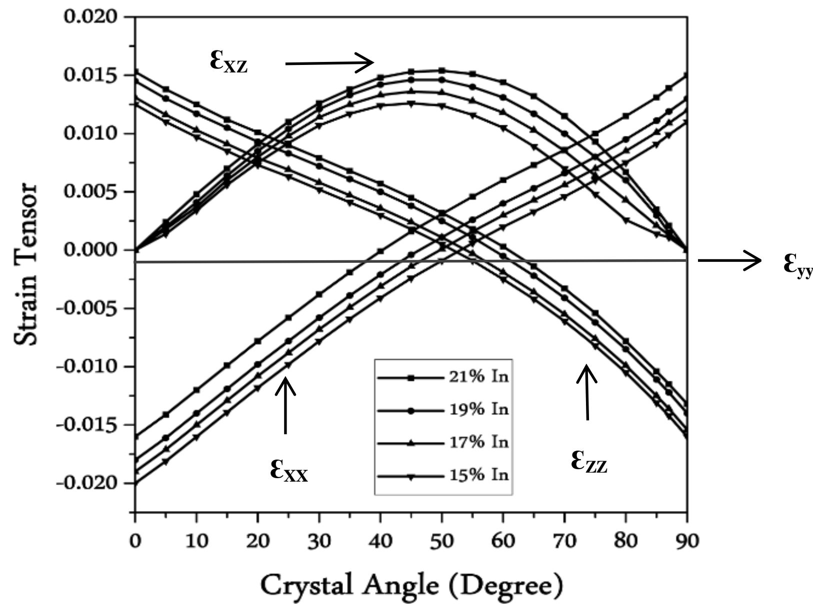

Fig. 5.1: Strain tensor components as function of crystal angle for 15%, 17%, 19% and 21% In

Figure 5.2 shows (a) the sum of the strain-induced PZ and SP polarizations normal with respect to the growth plane for the well and the barrier and (b) the internal field as a function of the angle θ between the growth direction and the c axis of $In_xGa_{1-x}N$/GaN QW structures. In case of the proposed LD structure, the well is compressively strained for the Indium composition selected here. The normal polarization is important because the QW structures have quantized energy levels along the growth direction. The normal polarization leads to the accumulation or depletion of carriers at the interfaces and creates an internal field. On which side of the interfaces the accumulation region is produced depends on the type of atomic plane at the interface (Ga or N)

in QW. The normal polarization is asymmetric with respect to the $(10\bar{1}0)$ orientation (θ=90°). The asymmetry of the normal polarization is due to the change of the atomic plane type with respect to the $(10\bar{1}0)$ orientation. The internal field is determined from the difference between the PZ and SP polarizations between the well and the barrier. From the figure, it is seen that the internal field gradually increases and changes its sign with increasing crystal angle and In composition from 15% to 21%. The internal field becomes zero for the $(10\bar{1}0)$ crystal orientation because the SP and strain-induced PZ polarizations are zero. In addition, the internal field is shown to become zero near the crystal angle of 61°, 58°, 55° and 53° with 15%, 17%, 19% and 21% In because the sum of the PZ and SP polarizations in the barrier is equal to that in the well. Thus, lasing properties for these crystal orientations (for example, $(11\bar{2}2)$ semipolar orientation corresponding to 58.4° for $In_{0.17}Ga_{0.83}$ N/GaN QW) are expected to be greatly improved due to the reduction of the internal field.

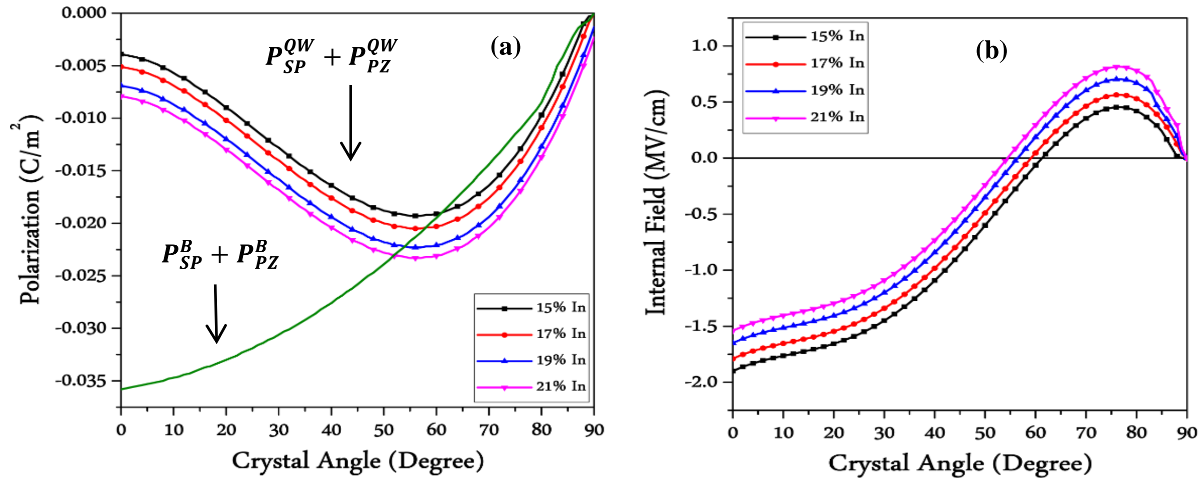

Fig. 5.2: (a) Sum of the strain-induced PZ and SP polarizations normal with respect to the growth plane for the well and the barrier and (b) Internal field as a function of the angle θ between the growth direction and the *c* axis of $In_xGa_{1-x}N$/GaN QW structure

5.2 Energy Band Dispersion Profile in (hkil) Orientation

Figure 5.3 shows calculated energy band dispersion relations obtained by solutions of the 6 × 6 **k·p** RSP Hamiltonian at Γ-point for WZ $In_{0.17}Ga_{0.83}N$/GaN QW blue laser including polarization field with the following growth planes: (a) (0001) (θ=0°), (b) $(10\bar{1}0)$ (θ=90°), $(10\bar{1}2)$ (θ=43°), $(11\bar{2}2)$ (θ=58.4°) and $(10\bar{1}1)$ (62°). Conduction Band (CB), Heavy-hole (HH), light-hole (LH)

and crystal field split-off hole (CH) band dispersions are indicated. The simulation is carried out in MATLAB environment at room temperature. The lattice mismatch between the epilayer ($In_{0.17}Ga_{0.83}N$) and the substrate (GaN) leads to a biaxial compressive strain of −0.0187, as indicated in fig. 1.To compare the orientation-dependent energies; the figures are plotted as a function of wave vector in the same scale. The conduction band is almost the same as in a c-plane QW because the electron effective mass is nearly isotropic and the wavefunction of electrons is spherically symmetric envelope function. It is demonstrated that, for nonzero value of k (wave vector in the plain direction); the increasing coupling from distant bands gives rise to strong non-parabolicities at the top valence band structure. The result for (0001) and $(10\bar{1}0)$-oriented QW structure shows small subband energy spacing between HH & LH. This strong intermixing and piezoelectric field induced strong QCSE effectively ceases quick transition of charge carriers causing reduction in lasing efficiency. On the other hand, semipolar $(11\bar{2}2)$ and $(10\bar{1}1)$ orientation shows better dispersion profile in terms of reduced interband coupling and QCSE. So, they have a reduced density-of-states near the valence band edge leading to reduced hole effective mass and improved emission characteristics.

Table 5.2 shows the energy gaps between CB to HH, LH and CH bands at the band edges as a function of the crystal orientation. It is noted that crystal orientation changes the energy splitting.

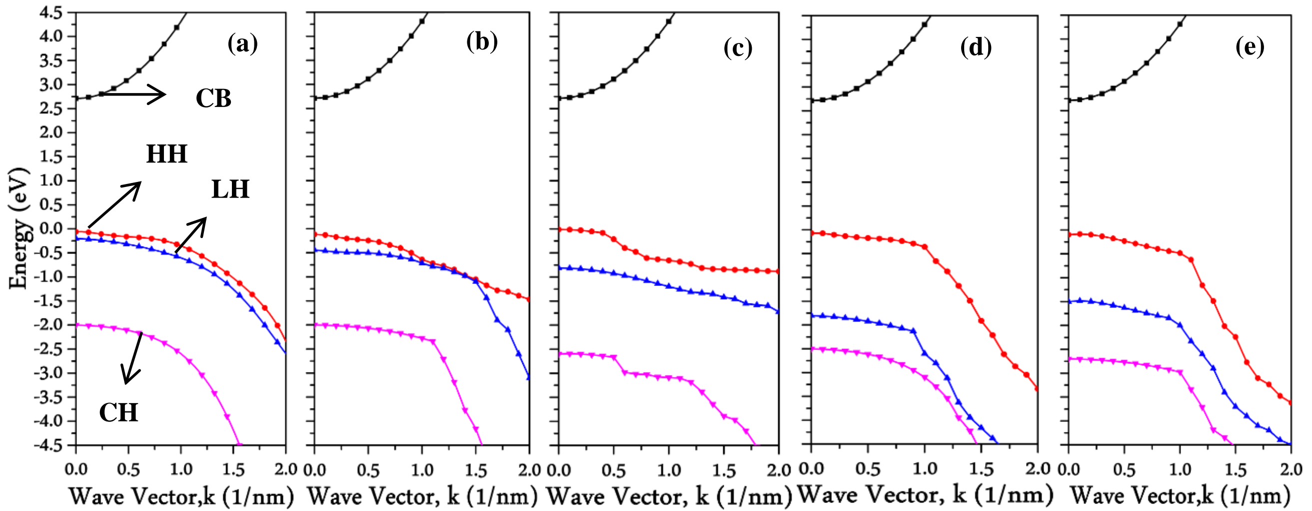

Fig 5.3: Energy Band Dispersion Profile in (a) (0001), (b) $(10\bar{1}0)$, (c) $(10\bar{1}2)$ (d) $(11\bar{2}2)$ and (e) $(10\bar{1}1)$ Crystal Orientation of InGaN/GaN QW Blue Laser

Table 5.2
Orientation-dependent Energy Separation

Crystal orientation	C-HH(eV)	C-LH(eV)	HH-LH(eV)
(0001)	2.772	2.912	0.14
$(10\bar{1}2)$	2.725	3.525	0.80
$(11\bar{2}2)$	2.780	4.512	1.732
$(10\bar{1}1)$	2.812	4.212	1.4
$(10\bar{1}0)$	2.830	3.152	0.322

The energy separation between C and HH is maximum in non-polar $(10\bar{1}0)$ crystal orientation and minimum in $(10\bar{1}2)$ orientation. The zone-center splitting between HH and LH is evaluated maximum in semipolar $(11\bar{2}2)$ orientation and minimum in (0001) orientation.

5.3 Momentum Matrix in (hkil) Orientation

As the QW is compressively strained, the maximum transition occurs between C to HH. The momentum matrix element for the transitions between C-HH, C-LH and C-CH in different orientations for the (a) TE and (b) TM polarizations is calculated from band-edge Eigen values and shown as function of θ in Fig. 5.4.

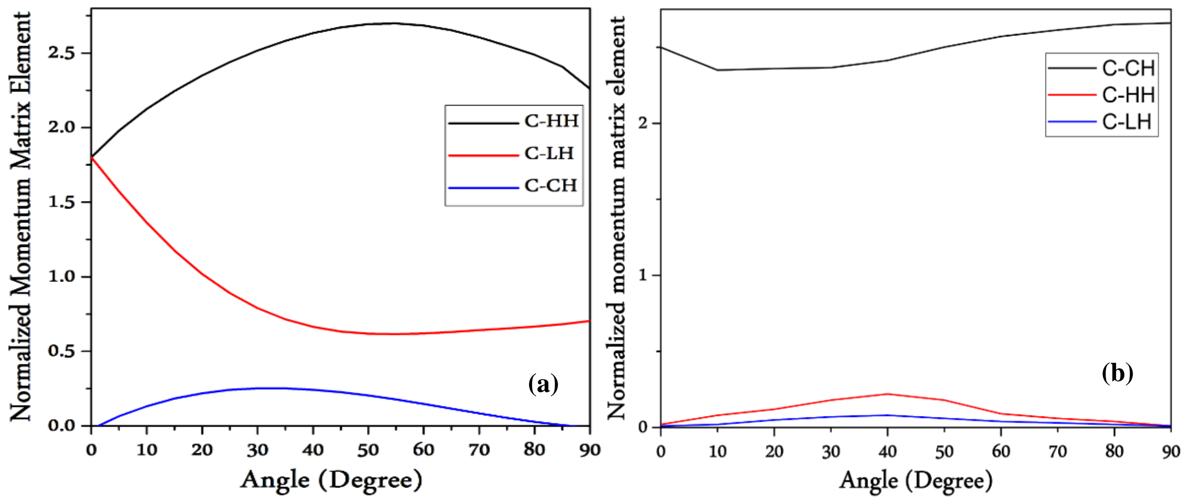

Fig 5.4: Interband optical momentum matrix elements at the band edges as a function of crystal orientation for the (a) TE and (b) TM polarizations of $In_{0.17}Ga_{0.83}N$/GaN QW blue laser

For the (0001) orientation (θ=0°), the interband optical matrix elements for the HH and LH bands to the conduction band are dominated by the TE polarization, as shown in Fig. 5.4(a), and

then interband transition between the CH band and the conduction band is dominated by the TM polarization, as shown in Fig. 5.4(b). It is found that with an increasing angle θ, the optical matrix element for the C-LH transition rapidly decreases giving a minimum at 58°, and then shows slight increase till 90° i.e. $(10\bar{1}0)$ orientation. On the other hand, the TE optical matrix element for the C-HH transition rapidly increases; approaches a maximum at 58° and then starts to decrease till 90° crystal angle. The peak value is about 1.5 times as large as that of the (0001) orientation. This can be explained by the crystal orientation-dependent energy band dispersion profile of Fig. 5.1. For (0001) and $(10\bar{1}0)$ orientation, the splitting between HH and LH bands is very small, ceasing quick carrier transition from valence band (VB) to conduction band (CB) due to strong interband coupling. On other side, since the HH-LH energy splitting is maximum at $(11\bar{2}2)$ orientation (θ=58.4°); so the momentum matrix for this orientation is near highest value.

The momentum matrix elements for C-HH and C-LH transitions in different crystal orientations for TE polarization are shown in Fig. 5.5(a) and 5.5(b).

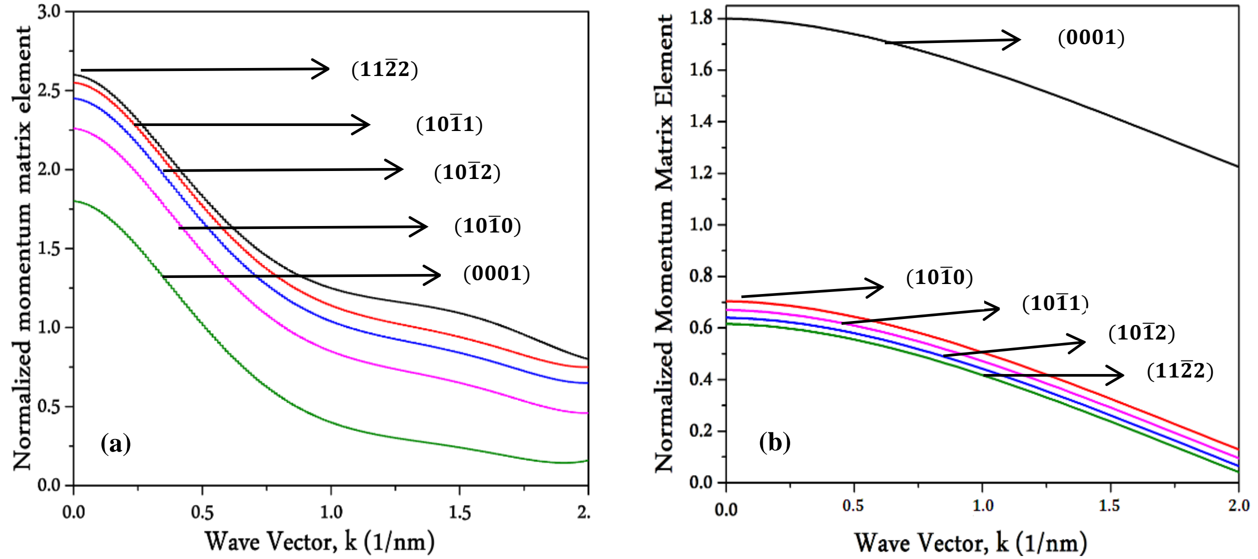

Fig. 5.5: Crystal orientation-dependent normalized momentum matrix element for (a) C-HH transition and (b) C-LH transition

The maximum value of momentum matrix element is evaluated in $(11\bar{2}2)$ orientation and minimum in (0001) orientation for C-HH transition. For C-LH transition, the maximum value of momentum matrix element is evaluated in (0001) orientation and minimum in $(11\bar{2}2)$

orientation. This fact is verified from fig. 5.3 and 5.4 as the overlapping function of electrons and holes is maximum and minimum for this two crystal orientation.

5.4 Optical Emission Profile in (hkil) Orientation

Fig. 5.6(a) and 5.6(b) shows the orientation-dependent optical emission profile of the InGaN/GaN QW blue laser structure for TE and TM polarization. The results are evaluated for the injection carrier density 3.5×10^{19} cm^{-3}. It's verified from the figure 5.6 that TE polarization is dominant for the QW laser structure. Here, peak gain and peak emission wavelength have crystal orientation dependence. The peak gains are evaluated to be 3845, 4178, 4460, 4880 and 4750 cm^{-1} with wavelength of 447.3, 438, 455, 446 and 441nm at (0001), $(10\bar{1}0)$, $(10\bar{1}2)$, $(11\bar{2}2)$ and $(10\bar{1}1)$ orientations for TE polarization. Maximum gain is evaluated in the $(11\bar{2}2)$ semipolar direction due to reduced density of states and large gap between heavy hole and light hole band, so reduced QCSE and reduced effective mass. The separation between HH and LH is also found maximum in this orientation which is also the cause of higher gain.

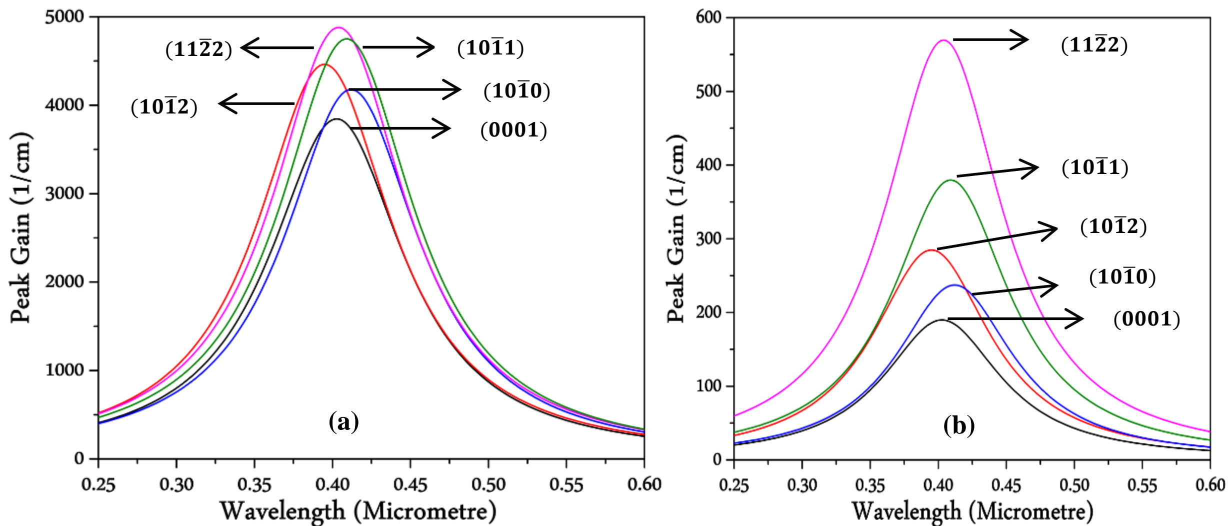

Fig 5.6: Optical emission profiles of $In_{0.17}Ga_{0.83}N/GaN$ QW Blue Laser in different orientation for (a) TE Polarization and (b) TM polarization

There is a strong correlation between the peak optical gain and injection carrier density in a particular crystal orientation. Carrier density-dependent optical gain in different crystal orientations is shown in fig. 5.7. It is found that starting of optical gain is highly dependent on the injection carrier density in a particular crystal orientation. The carrier density required to start

gain is found to be higher in (0001) orientation and smaller in $(11\bar{2}2)$ orientation. It is also found that at lower injection carrier density ($1.5\sim2\times10^{19}$ cm^{-3}), output optical power characteristics in (0001) and $(10\bar{1}0)$ crystal orientations are very much close to each other.

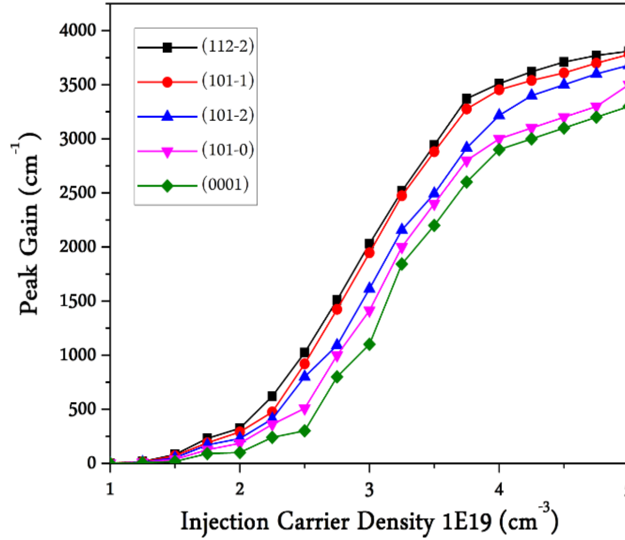

Fig 5.7: Carrier density-dependent optical gain in different crystal orientations

But, at higher injection region there is a small difference in peak gain in these orientations. As seen in fig. 5.7, the highest optical gain is obtained in $(11\bar{2}2)$ orientation and lowest in (0001) orientation with injection carrier density.

Now, in the following table, the effect of PZ field and related QCSE on the energy band dispersion profile and optical emission profile of $In_{0.17}Ga_{0.83}N/GaN$ QW blue laser is shown in details. It's seen that for $(11\bar{2}2)$ and $(10\bar{1}0)$ orientation, the effect of PZ field is null which is verified from Fig. 5.2. The shift in energy, peak gain and peak wavelength is evaluated maximum in (0001) orientation and minimum in $(10\bar{1}1)$ orientation.

Table 5.3
Effect of PZ field in different crystal orientation

Crystal Orientation	Peak Gain (cm^{-1})		Peak Wavelength (nm)		Conduction band energy shifts, ΔE^c (meV)	HH band energy shifts, ΔE^{hh} (meV)
	Without PZ field	With PZ field	Without PZ field	With PZ field		
(0001)	4245	3845	443	447.3	0.018	0.009
$(10\bar{1}2)$	4660	4460	452	455	0.013	0.0024
$(11\bar{2}2)$	4880	4880	446	446	0	0

$(10\bar{1}1)$	4800	4750	439	440.9	0.011	0.0016
$(10\bar{1}0)$	4178	4178	438	438	0	0

5.5 Output power characteristics in (hkil) Orientation

Now, to understand the performance of the proposed QW blue laser structure, it is very much important to study its output characteristics. The output optical power-input current characteristics are investigated from SIMULINK analysis of the equivalent circuit developed for the proposed laser structure. The procedures of converting mathematical model into equivalent model for the proposed laser structure and parameters used have been discussed in chapter 4, section 4.4. The optical power-injection current characteristics determined for compressive strained $In_{0.17}Ga_{0.83}N$/GaN SQW blue laser in different crystal orientations are shown in fig. 5.8. It is found that the maximum optical power of 4.35mW and minimum threshold current of 0.74mA are obtained in $(11\bar{2}2)$ oriented QW structure because of highest gain, momentum matrix element and lowest interband coupling between HH and LH is obtained in this orientation. Maximum threshold current is evaluated to be 1.3 mA in (0001) crystal orientation. As seen in fig. 5.8, the differences among the optical power for different QW structures are comparatively smaller at lower input currents than of those at higher input currents.

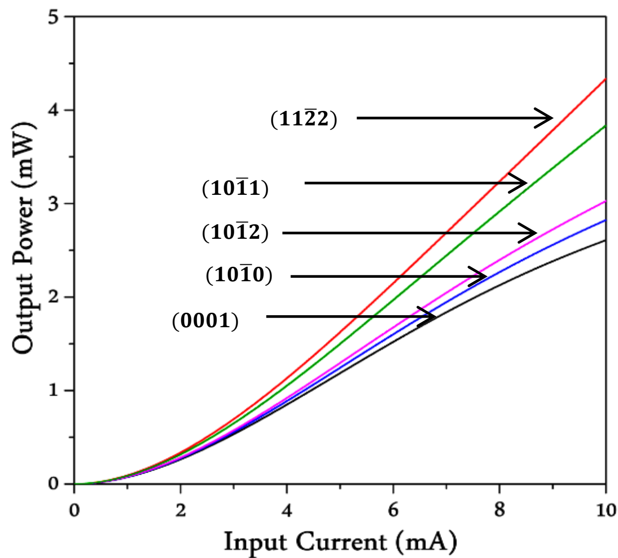

Fig 5.8: Orientation-dependent Output Power Curve of InGaN/GaN QW Blue Laser Diode

5.6 Frequency Response Analysis in (hkil) Orientation

Fig. 5.9 depicts the bode diagram in order to show magnitude (dB) and phase response of InGaN/GaN QW Blue laser in different crystal orientation. The results of the P-I response is used in order to obtain operating points of table 5.4 to simulate the frequency response. The detail procedure is discussed in chapter 4, section 4.5. With the operating points from this table, a third-order state-space model is generated for each crystal orientation. Then it was converted to bode plot using "bode" function in MATLAB.

Table 5.4

Operating point close to Threshold

Crystal Orientation	Pumping Current(mA)	QW Electron Density N_{op} (cm^{-3})	SCH Electron Density N_{bop} (cm^{-3})	Photon Density S_{op} (cm^{-3})
$(11\bar{2}2)$	1.10	1.90×10^{19}	1.42×10^{17}	1.10×10^{15}
$(10\bar{1}1)$	1.32	1.81×10^{19}	1.37×10^{17}	1.05×10^{14}
$(10\bar{1}2)$	1.54	1.74×10^{19}	1.32×10^{17}	1.22×10^{13}
$(10\bar{1}0)$	1.68	1.62×10^{19}	1.29×10^{17}	1.33×10^{12}
(0001)	1.77	1.58×10^{19}	1.27×10^{17}	1.60×10^{11}

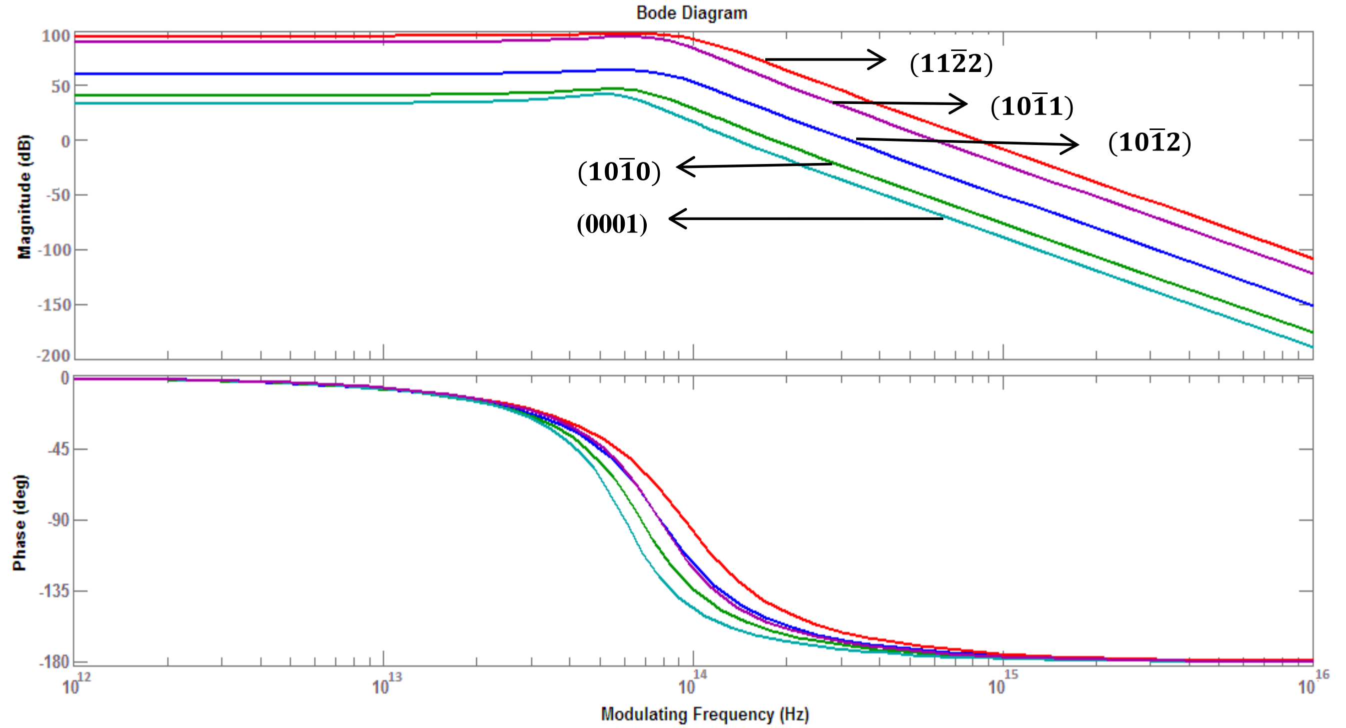

Fig 5.9: Frequency Response of InGaN/GaN QW Blue LD in different crystal orientation using operating points from Table 5.5

Since InGaN/GaN QW blue laser structure in each orientation shows positive gain and phase margin in the above Bode plot, the laser system for all orientations is stable. Highest and lowest magnitude (dB) response in obtained in semipolar $(11\bar{2}2)$ and polar (0001) crystal orientation because highest and lowest peak gain and optical power output is found in these two orientations. As seen from the figure, frequency response for $(10\bar{1}0)$ and (0001) orientation is close to each other because the gain characteristics of the above mentioned QW structures are almost same. Phase response at lower frequencies is seen to be closer to each other for all crystal orientations. At intermediate frequencies the laser system is somewhat resonant. As frequency increases further, the decibel gain decreases. It's obvious from the fig. 5.9 that phase response starts at 0° and then decreases to -180°.

From the magnitude (dB) response; we can calculate electrical bandwidth (Frequency range in which the magnitudes of the closed loop gain does not drop -3 dB) of the system using "bandwidth" function in MATLAB which is listed in table 5.5.

Table 5.5
Bandwidth of InGaN/GaN QW Blue LD in different crystal orientation

Crystal Orientation	Bandwidth (THz)
$(11\bar{2}2)$	5
$(10\bar{1}1)$	4.62
$(10\bar{1}2)$	2.21
$(10\bar{1}0)$	0.83
(0001)	0.76

The bandwidth (BW) indicates the frequency where the gain starts to fall off from its low-frequency value. Thus, the bandwidth indicates how well the system will track an input sinusoid. From the table, it's seen that highest BW of 5THz is achieved for $(11\bar{2}2)$ orientation. Since a large bandwidth corresponds to a small rise time, or fast response, it can be said that topmost speed of response for InGaN/GaN QW blue laser system can be found in semipolar $(11\bar{2}2)$ orientation (Crystal growth angle of 58.4° w.r.t c-plane).

5.7 Comparison of Strain-dependent Optoelectronic Performance in $(11\bar{2}2)$, $(10\bar{1}2)$ and (0001) Crystal Orientation

- **Strain-dependent Optoelectronic Performance in $(11\bar{2}2)$ Crystal Orientation**

Built-in strains due to lattice mismatch between active and barrier layers in SQW significantly modify the electronic band structures, especially the valence bands. Since best performance for InGaN/GaN QW blue laser is obtained in semipolar $(11\bar{2}2)$ crystal orientation (θ=58.4°), strain-dependent optoelectronic properties at 300K for this crystal orientation is discussed in this section.

Figure 5.10 shows the energy band dispersion profile in $(11\bar{2}2)$ crystal orientation for 15%, 17%, 19% and 21% Indium composition in well layer. It is found that at the band edge (k_t =0) the conduction band energy shifts towards higher energy with increasing the value of strain. The conduction band edge energies found to be shifted from 2.74 eV to 2.98 eV for changing the Indium composition from 15% to 21%. Apart from the band edge, the energy is found to increase gradually with wave vector. It is due to increasing potential level of electron (v_e in the well become more negative) in the well with increasing strain.

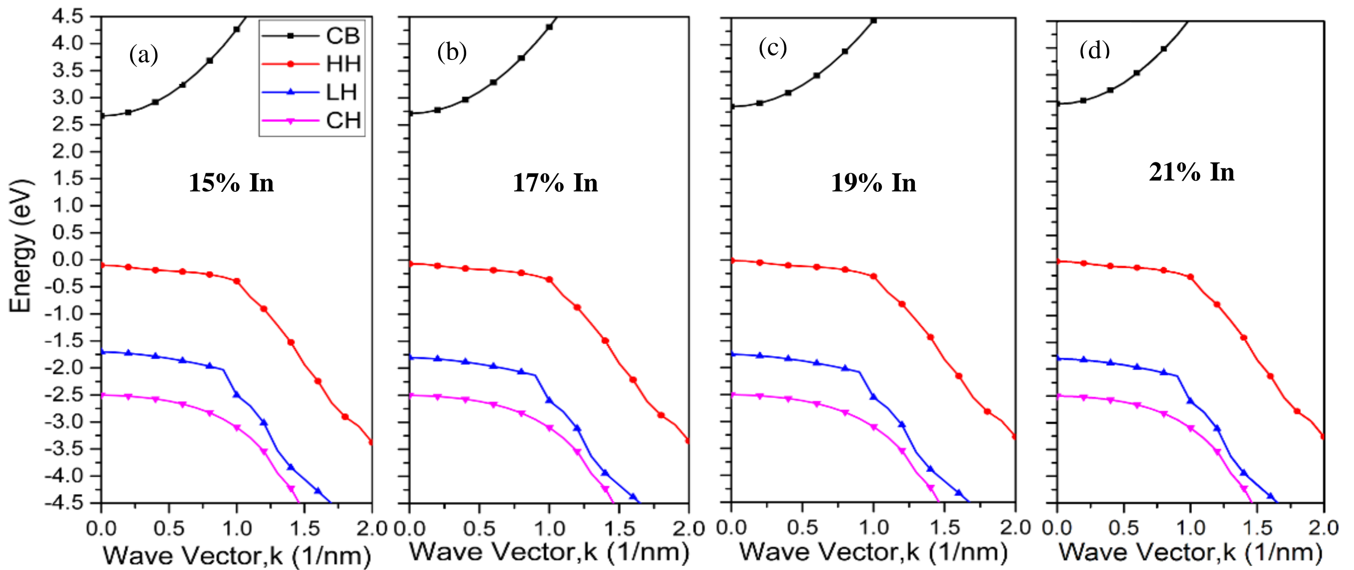

Fig 5.10: Energy Band Dispersion Profile for InGaN/GaN QW blue laser in $(11\bar{2}2)$ crystal orientation for (a) 15% Indium (b) 17% Indium (c) 19% Indium (d) 21% Indium

From the valence band dispersion profile, it's found that energy separations between valence subbands strongly depend on the state of strain. Even in unstrained condition there exists energy separation among valence subbands. The energy separations between conduction band (CB) to heavy hole (HH) and light hole (LH) at the band edge increase due to increasing Indium composition from 15% to 21%. The strain also extends the separation between HH and LH subbands as seen in Fig. 5.10. This indicates that the band-mixing effect between HH and LH is reduced with increasing strain. Table 5.6 shows the energy gaps between CB to HH, LH and CH bands at the band edges for different values of strain.

As the QW is compressively strained, the maximum transition occurs between CB to HH. The momentum matrix element (TE polarization) for the transitions between CB to HH for different values of strain is calculated using Eq. (4.25) and shown in Fig. 5.11. It is found in Fig. 5.11 that the values of wave vector-dependent momentum matrix elements increase with increasing strain. It is due to the fact that the overlapping of wave function of electrons and holes increases with increasing the magnitude of strains. The improvements can also be attributed to reduction of band mixing between HH and LH which causes reduction of the effective mass of holes. This, in turn, increases its Fermi level more quickly with respect to the increase in injected carriers, which leads to a large value of momentum matrix.

Table 5.6

Strain-dependent Energy Separation for $(11\bar{2}2)$ crystal orientation

In Composition	C-HH(eV)	C-LH(eV)	HH-LH(eV)
15%	2.742	4.562	1.6
17%	2.780	4.512	1.732
19%	2.862	4.612	1.75
21%	2.880	4.492	1.812

The optical gain spectra are calculated using equation (4.20) for different values of strain. The results are summarized in fig. 5.12 for TE and TM polarizations. For the injection carrier density 3.5×10^{19} cm^{-3} , the peak gains in TE direction are evaluated to be 5190 cm^{-1}, 4960 cm^{-1}, 4880 cm^{-1}, and 4730 cm^{-1},when the Indium composition in well is 21%, 19%, 17% and 15% respectively.

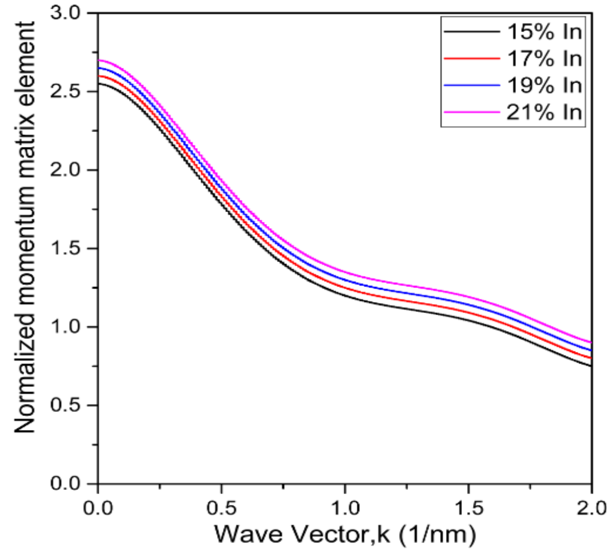

Fig. 5.11: Strain-dependent momentum matrix element for C-HH transition

The value of peak gain is shown to increase with increasing strain as the magnitude of momentum matrix element increases for CB-HH transition. The increased energy separations between HH and LH also contribute in achieving higher gain. The emission wavelength is found to change from 0.452 μm to 0.430 μm as the energy separation increases for CB-HH transition with strain values. For TM polarization, the peak gains are evaluated to be 660 cm^{-1}, 605 cm^{-1}, 540 cm^{-1}, and 430 cm^{-1}. It's seen from fig 5.12 that TE polarization is dominant for the QW laser structure.

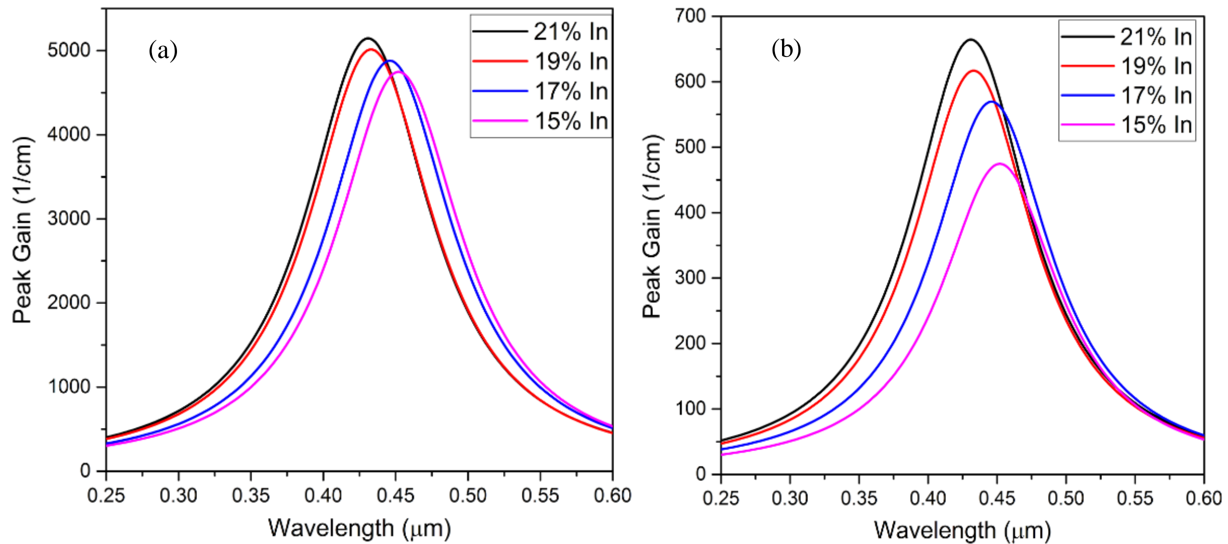

Fig. 5.12: Optical gain profile of InGaN/GaN QW blue laser for different values of compressive strain (a) TE Polarization (b) TM Polarization

The carrier density-dependent optical peak gains are calculated and shown in fig 5.13. It is found that the optical gain starts approximately at the carrier density $(1.8\sim2)\times10^{19}$cm^{-3} for all values of strain and then gradually increases with increasing carrier density as well with strain value. However, the change in optical gain is not significant with strain when the injection current density is lower than 1.5×10^{19} cm^{-3}. From fig. 5.13, it is found that the maximum optical peak gain is evaluated when indium composition in well is 21% for all values of carrier density. The optical gain also found to change significantly with carrier density when the well is compressively strained by 15% to 17% indium content. In contrast, the change in optical gain is not remarkable when the well is strained from 17% to 19% indium content with injection carrier density.

Fig. 5.14 shows the P-I response for $(11\bar{2}2)$-oriented InGaN/GaN QW blue laser by varying indium content in well layer. This result is obtained by using strain-dependent peak gain coefficient G_o and corresponding carrier density N_o values from fig. 13 and insert them in equivalent Simulink model.

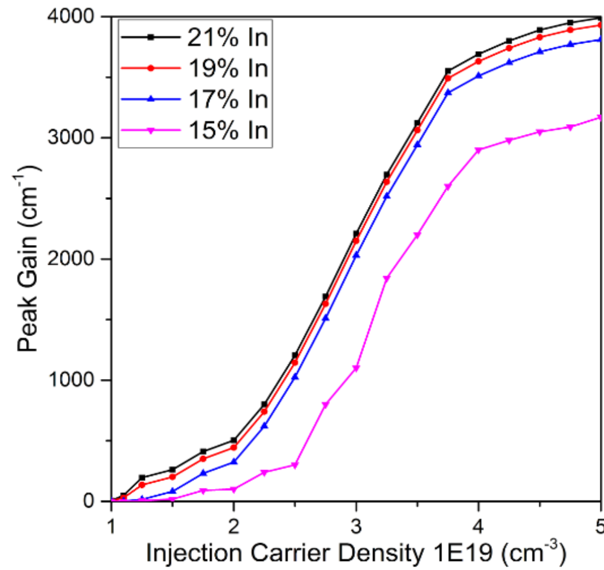

Fig. 5.13: Peak gain as a function of carrier concentrations for different compressive strained QWs

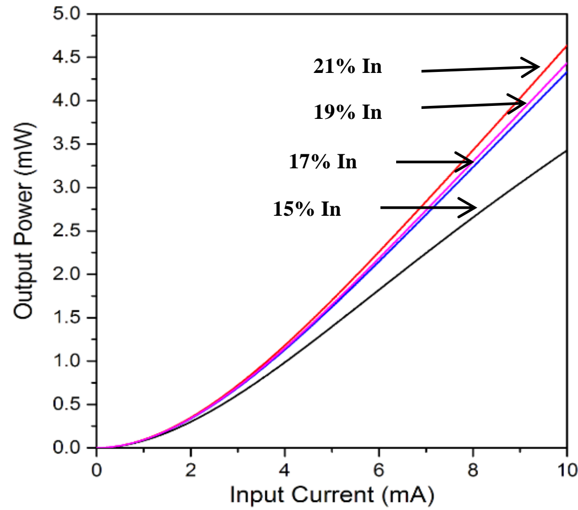

Fig. 5.14: Output optical power-input current response for different compressive strained QWs

It's noticed from fig. 5.14 that at lower injection current (< 0.8mA), the output optical power is approximately constant for all values of strains. However, the output optical power increases gradually with strain when the injection currents are higher than 1.32 mA. Here the maximum optical power is obtained for 21% indium content in well, because higher optical gain is obtained at this value.

Fig. 5.15 shows the bode diagram to analyze frequency response of $(11\bar{2}2)$-oriented InGaN/GaN QW Blue laser for different values of indium composition. The results of the P-I response is used in order to construct the 3rd order state-space model shown in Eq. 4.35.

As each value of compressive strain shows positive gain and phase margin in the above Bode plot, the laser system is stable. Highest magnitude (dB) response in obtained for 21% indium content in well because highest peak gain and optical power output is found here. From the magnitude (dB) response; we can calculate electrical bandwidth of the system which is listed in table 5.7.

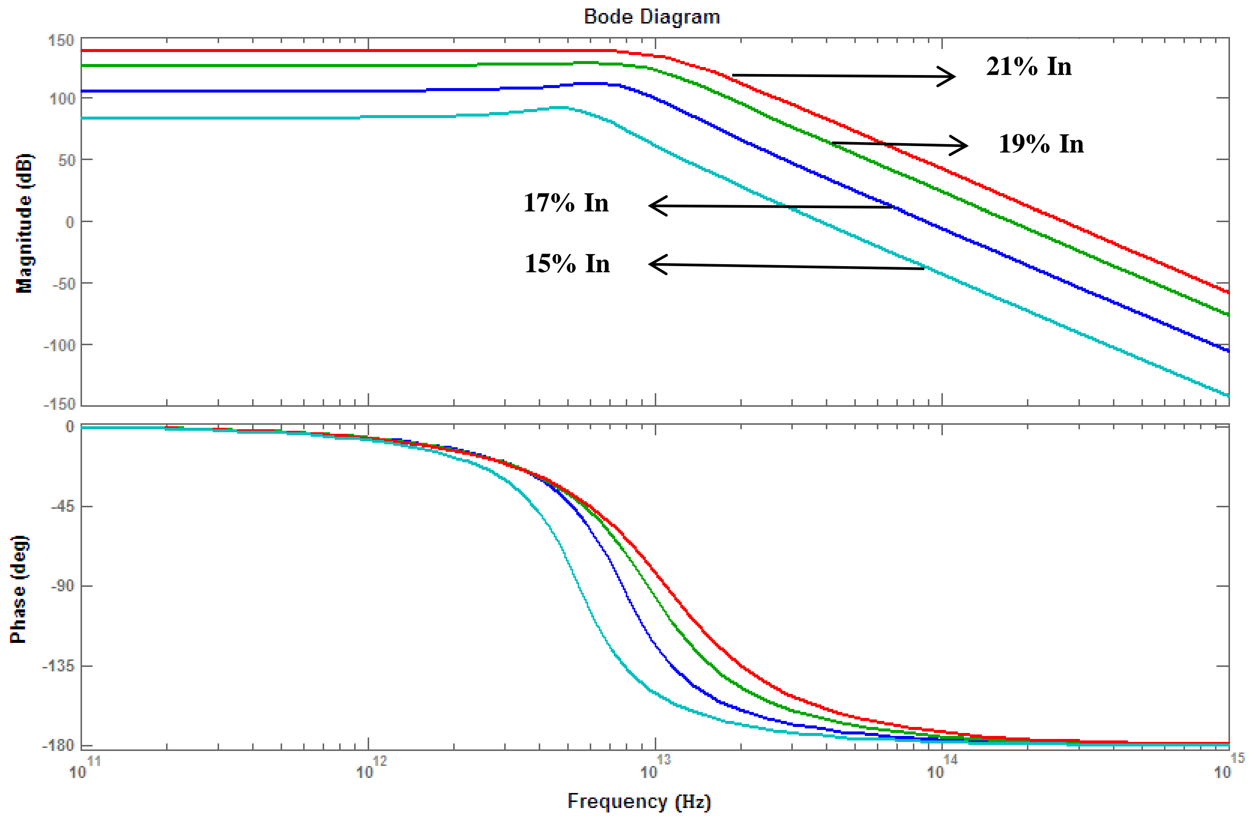

Fig. 5.15: Frequency Response in $(11\bar{2}2)$ orientation for different compressive strained QW

Table 5.7: Bandwidth of InGaN/GaN QW Blue LD for different In composition

Indium composition	Bandwidth (THz)
21%	7.8
19%	6.9
17%	5
15%	3.7

Strain-dependent optoelectronic properties like energy band dispersion profile, optical emission spectra, output P-I characteristics, magnitude and phase response, electrical bandwidth etc. for semipolar $(10\bar{1}2)$ and polar (0001) crystal orientations at room temperature will be discussed in subsequent sections.

- **Strain-dependent Optoelectronic Performance in $(10\bar{1}2)$ Crystal Orientation**

Figure 5.16 shows the energy band dispersion profiles in $(10\bar{1}2)$ crystal orientation for 15%, 17%, 19% and 21% Indium composition in the active layer. The conduction band edge energies found to be shifted from 2.70 eV to 2.76 eV for changing the Indium composition from 15% to 21%. The energy separation between HH to LH is seen to be increased from 0.53 eV to 1.25 eV with increasing strain magnitude. This change in energy separation is more prominent than semipolar $(11\bar{2}2)$ crystal orientation. Table 5.8 summarizes the energy gaps between CB to HH, LH, and CH bands at the band edges for different values of strain.

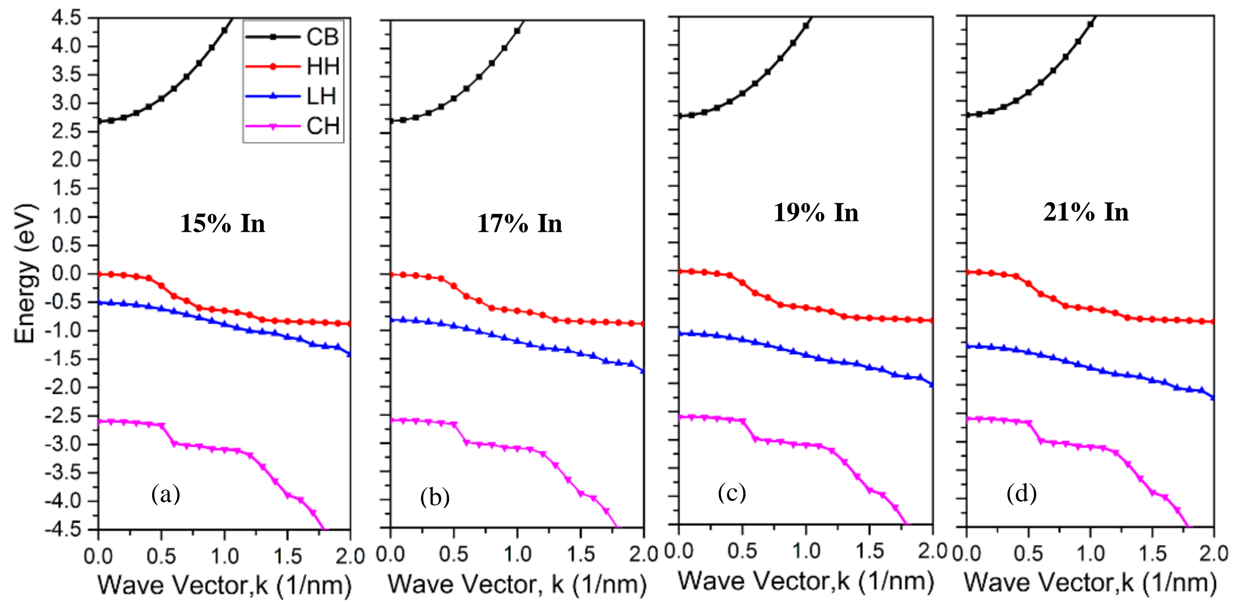

Fig. 5.16: Energy band dispersion profiles for InGaN/GaN QW blue laser in $(10\bar{1}2)$ crystal orientation for the Indium composition of (a) 15%, (b) 17%, (c) 19%, and (d) 21%

Table 5.8

Strain-dependent Energy Separation for $(10\bar{1}2)$ crystal orientation

In Composition	C-HH(eV)	C-LH(eV)	HH-LH(eV)
15%	2.700	3.230	0.53
17%	2.725	3.525	0.80
19%	2.740	3.790	1.05
21%	2.760	4.010	1.25

The momentum matrix element (TE polarization) for the transitions between CB to HH for different values of strain is calculated using Eq. (4.25) and shown in Fig. 5.17. It is found in fig. 5.17 that wave vector-dependent momentum matrix elements increase with increasing strain. But the values of momentum matrix are closer to each other than semipolar $(11\bar{2}2)$ crystal orientation.

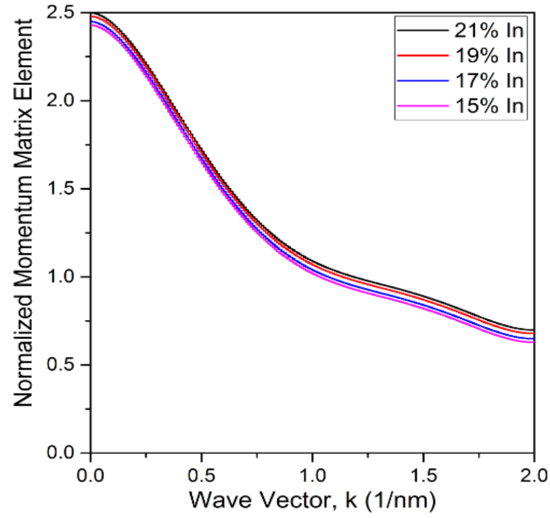

Fig. 5.17: Strain-dependent momentum matrix element for C-HH transition

The optical gain spectra for TE and TM polarization are calculated using equation (4.20) for different values of strain and summarized in fig. 5.18.

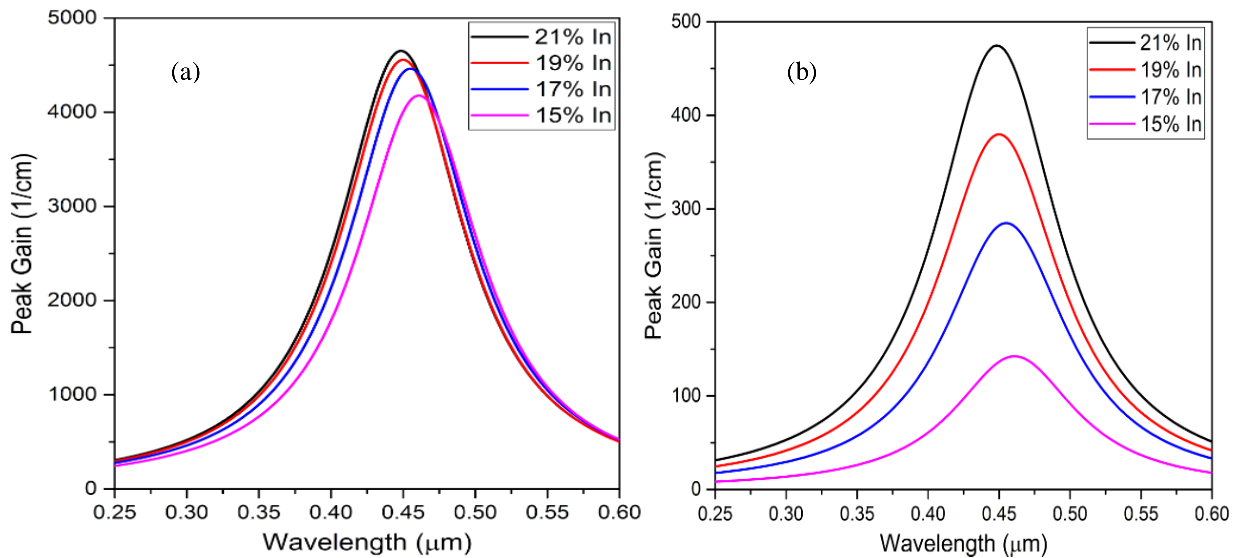

Fig. 5.18: Optical gain profile of InGaN/GaN QW blue laser for different values of compressive strain (a) TE Polarization (b) TM Polarization

For the injection carrier density 3.5×10^{19} cm^{-3}, the peak gains (TE polarization) are evaluated to be 4720 cm^{-1}, 4530 cm^{-1}, 4380 cm^{-1}, and 4200 cm^{-1}, when the Indium compositions in the active region are 21%, 19%, 17% and 15%, respectively. The emission wavelength is found to vary from 0.449 μm to 0.459 μm due to strain. For TM polarization, the peak gains are evaluated to be 460 cm^{-1}, 352 cm^{-1}, 262 cm^{-1}, and 140 cm^{-1}.

The carrier density-dependent optical peak gains are calculated for TE polarization and shown in fig 5.19. It is found that the optical gain starts approximately at the carrier density $(1.5\text{~}2.2)\times10^{19}$cm^{-3} for all values of strain and then gradually increases with increasing carrier density as well as with magnitude of strain. It is found that the maximum value of peak gain is evaluated when indium composition in the well is 21% for all values of carrier density.

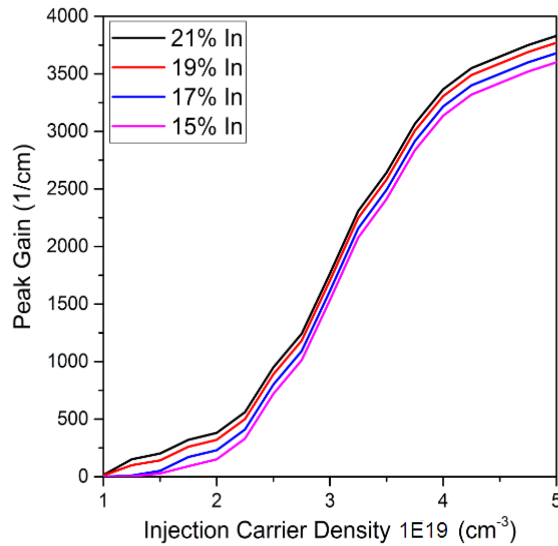

Fig. 5.19: Peak gain as a function of carrier concentrations for compressively strained QWs

Fig. 5.20 shows the P-I response for $(10\bar{1}2)$-oriented InGaN/GaN QW blue laser with the variation of Indium composition in the active layer. Maximum optical power of 3.32mW and minimum threshold current of 0.87mA is obtained when the indium content in well is 21%. It's also noticed from fig. 5.20 that change in output optical power isn't so obvious when injection current is below 2.2 mA.

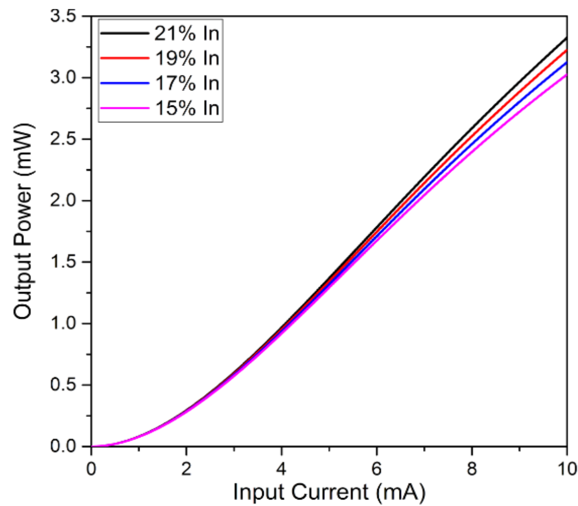

Fig. 5.20: Output optical power-input current response for compressively strained QWs

From Bode plot of fig. 5.21, it's noticed that positive gain and phase margin is achieved for each compressively strained QW structure. Highest magnitude (dB) response in obtained for 21% Indium content in the well because highest peak gain and optical power output is found here.

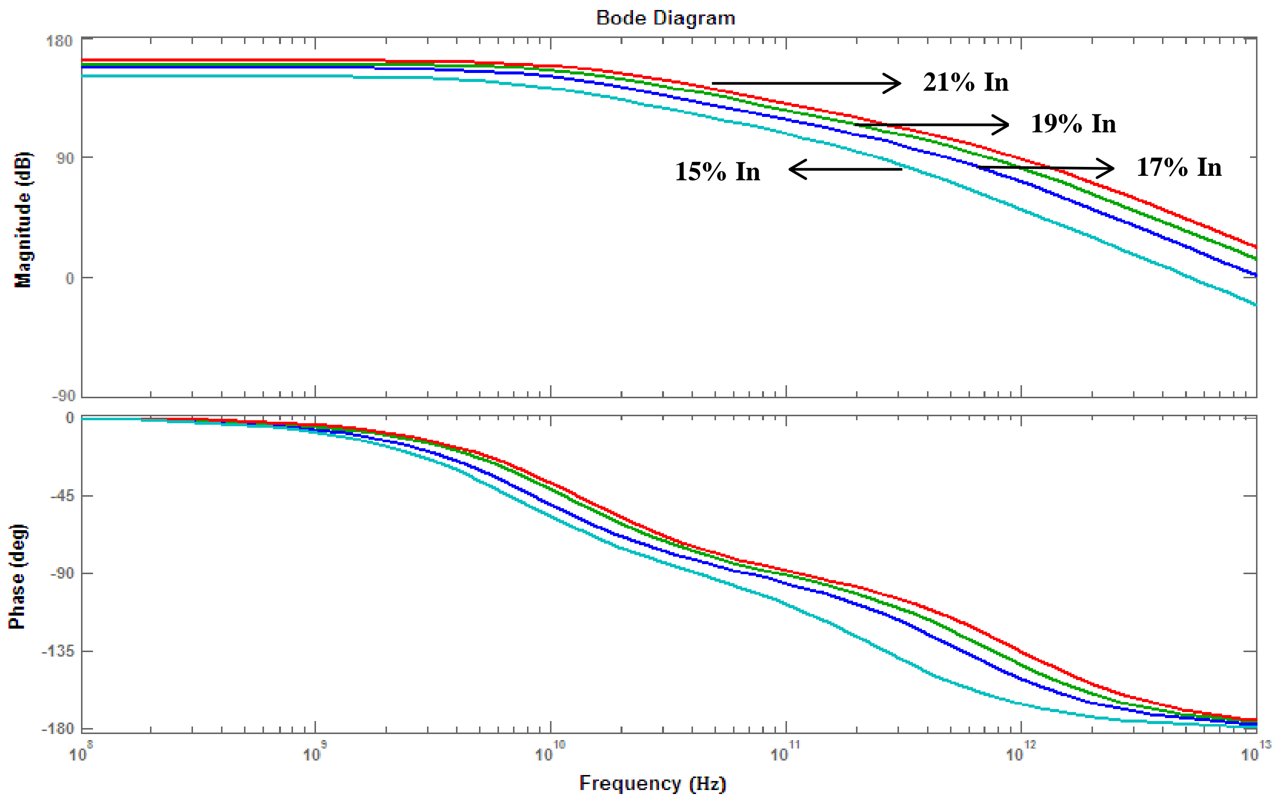

Fig. 5.21: Frequency response evaluated in $(10\bar{1}2)$ oriented compressively strained QWs

From the magnitude (dB) response, electrical bandwidth has been calculated and listed in Table 5.9.

Table 5.9: Bandwidth of InGaN/GaN QW Blue LD for different Indium composition

Indium composition	Bandwidth (THz)
21%	4.2
19%	3.3
17%	2.21
15%	1.7

- **Strain-dependent Optoelectronic Performance in (0001) Crystal Orientation**

Figure 5.22 shows the energy band dispersion profiles in (0001) crystal orientation for 15%, 17%, 19% and 21% Indium composition in the active layer. The conduction band edge energies found to be shifted from 2.65 eV to 2.83 eV for changing the Indium composition from 15% to 21%. The energy separation between HH to LH is seen to be increased from 0.10 eV to 0.38 eV with increasing strain magnitude. This change in energy separation is less prominent than semipolar $(10\bar{1}2)$ crystal orientation. Table 5.10 summarizes the energy gaps between CB to HH, LH, and CH bands at the band edges for different values of strain.

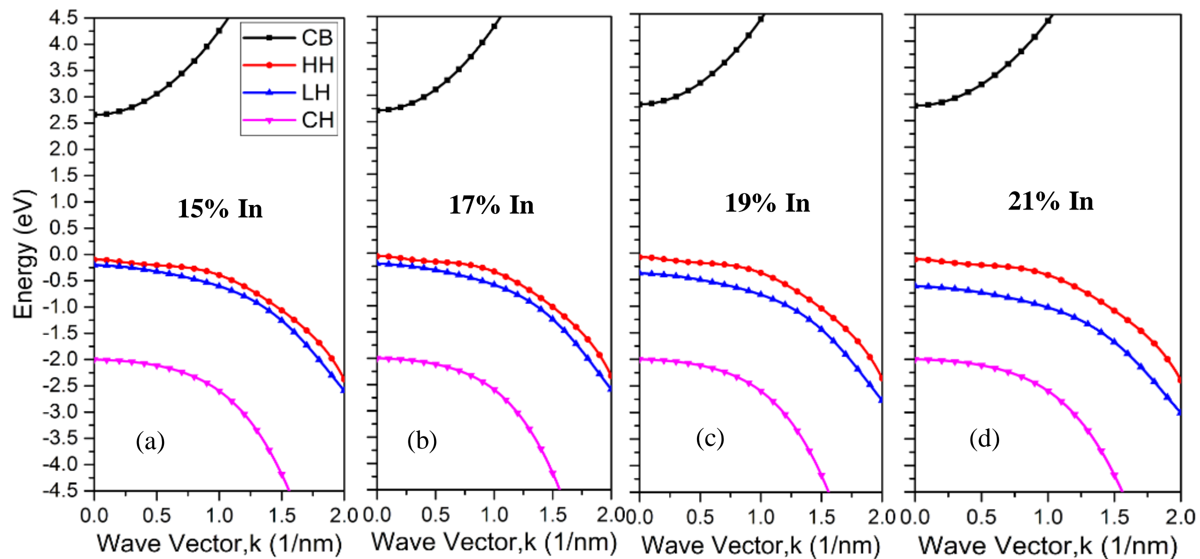

Fig. 5.22: Energy band dispersion profiles for InGaN/GaN QW blue laser in (0001) crystal orientation for the Indium composition of (a) 15%, (b) 17%, (c) 19%, and (d) 21%.

Table 5.10

Strain-dependent Energy Separation for (0001) crystal orientation

In Composition	C-HH(eV)	C-LH(eV)	HH-LH(eV)
15%	2.683	2.783	0.10
17%	2.772	2.912	0.14
19%	2.794	3.012	0.22
21%	2.806	3.186	0.38

The momentum matrix element (TE polarization) for the transitions between CB to HH for different values of strain is calculated using Eq. (4.25) and shown in Fig. 5.23. It is found in fig. 5.23 that wave vector-dependent momentum matrix elements increase with increasing strain. But the values of momentum matrix show reduction than semipolar $(11\bar{2}2)$ and $(10\bar{1}2)$ crystal orientation.

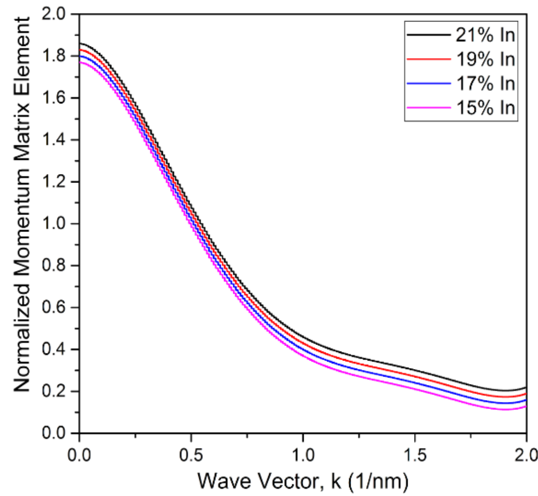

Fig. 5.23: Strain-dependent momentum matrix element for C-HH transition

The optical gain spectra for TE and TM polarization are calculated using equation (4.20) for different values of strain and summarized in fig. 5.24. For the injection carrier density 3.5×10^{19} cm^{-3}, the peak gains (TE polarization) are evaluated to be 4020 cm^{-1}, 3890 cm^{-1}, 3740 cm^{-1}, and 3610 cm^{-1}, when the Indium compositions in the active region are 21%, 19%, 17% and 15%, respectively. The emission wavelength is found to vary from 0.462 µm to 0.442 µm due to strain. For TM polarization, the peak gains are evaluated to be 285 cm^{-1}, 230 cm^{-1}, 180 cm^{-1}, and 135 cm^{-1}.

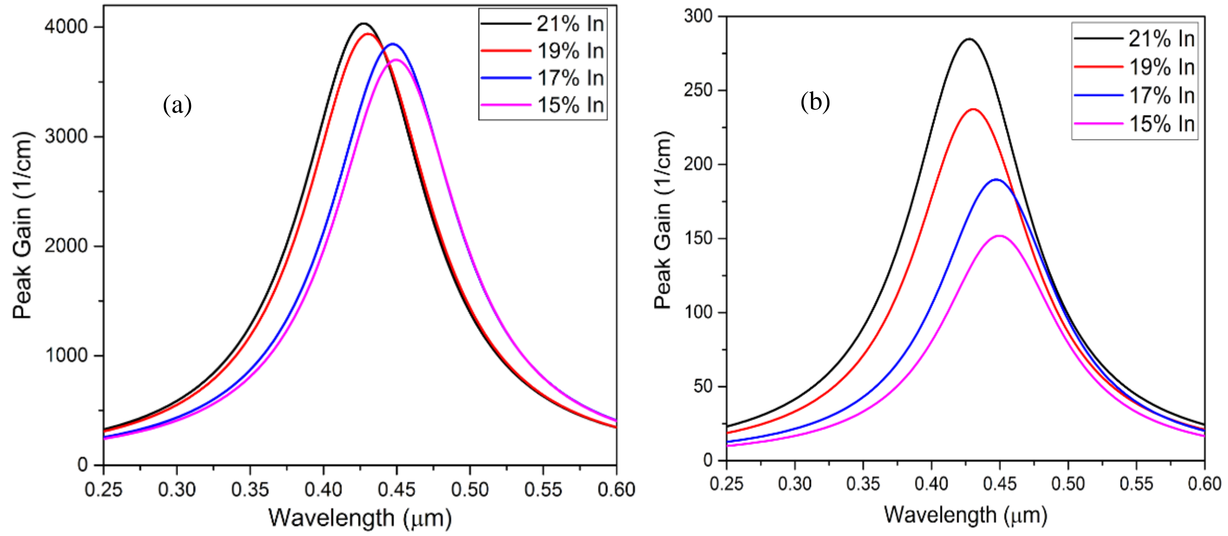

Fig. 5.24: Optical gain profile of InGaN/GaN QW blue laser for different values of compressive strain (a) TE Polarization (b) TM Polarization

The carrier density-dependent optical peak gains are calculated for TE polarization and shown in fig 5.25. It is found that the optical gain starts approximately at the carrier density $(2\sim2.5)\times10^{19}cm^{-3}$ for all values of strain and then gradually increases with increasing carrier density as well as with magnitude of strain. It is found that the maximum value of peak gain is evaluated when indium composition in the well is 21% for all values of carrier density.

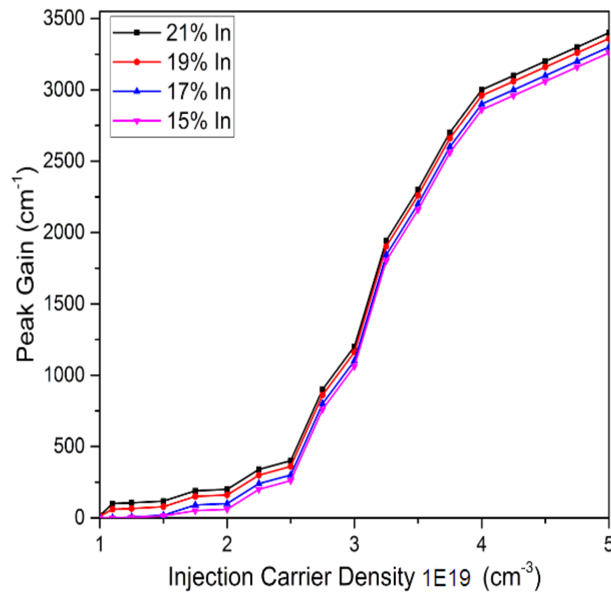

Fig. 5.25: Peak gain as a function of carrier concentrations for compressively strained QWs

Fig. 5.26 shows the P-I response for (0001)-oriented InGaN/GaN QW blue laser with the variation of Indium composition in the active layer. Maximum optical power of 3.17mW and minimum threshold current of 1.02 mA is obtained when the indium content in well is 21%. It's also noticed from fig. 5.26 that change in output optical power isn't so obvious when injection current is below 1.7 mA.

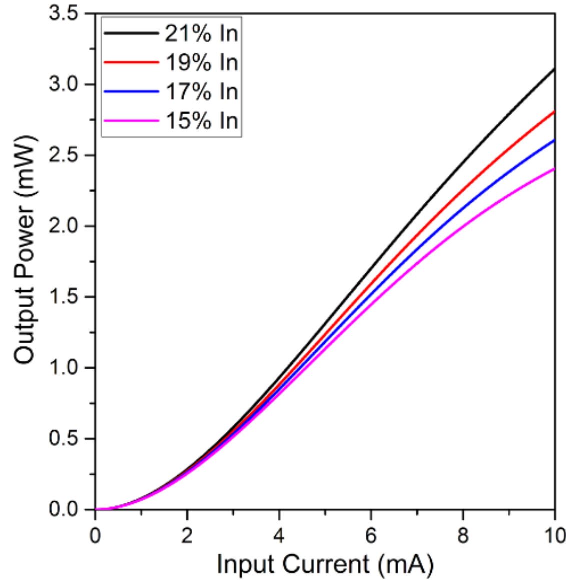

Fig. 5.26: Output optical power-input current response for compressively strained QWs

From Bode plot of fig. 5.27, it's noticed that positive gain and phase margin is achieved for each compressively strained QW structure. Highest magnitude (dB) response in obtained for 21% Indium content in the well because highest peak gain and optical power output is found here. From the magnitude (dB) response, electrical bandwidth has been calculated and listed in Table 5.11.

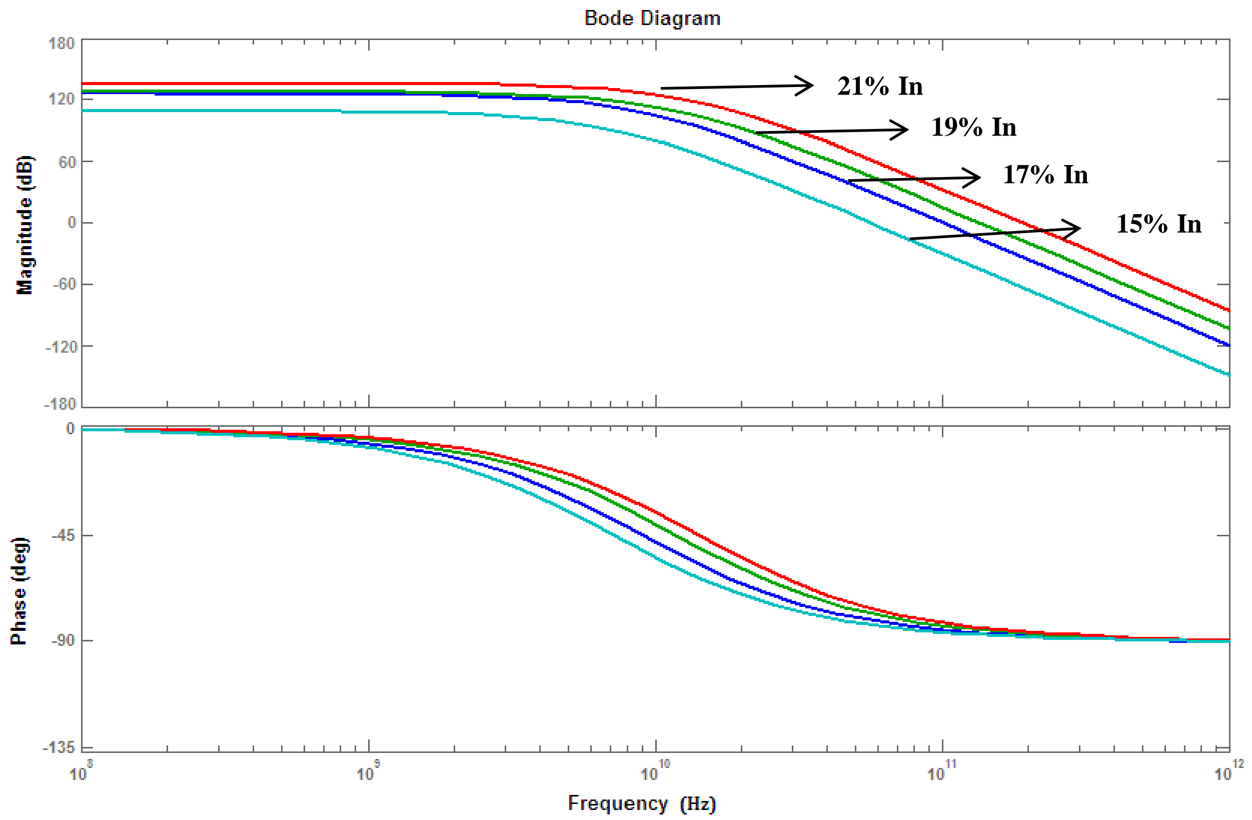

Fig. 5.27: Frequency response evaluated in (0001) oriented compressively strained QWs

Table 5.11: Bandwidth of InGaN/GaN QW Blue LD for different Indium composition

Indium composition	Bandwidth (THz)
21%	1.70
19%	1.06
17%	0.76
15%	0.51

CHAPTER VI

Conclusion

6.1 Contributions

To recapitulate, the optoelectronic performance of 445 nm InGaN/GaN QW blue laser is studied in conventional (0001) as well as non-conventional $(10\bar{1}0)$, $(10\bar{1}2)$, $(11\bar{2}2)$ and $(10\bar{1}1)$ crystal orientations at room temperature in MATLAB/Simulink environment. Mathematical model for the proposed laser is developed using Schrödinger equation taking into account of strain, change in crystal orientations and piezoelectric field. To obtain the energy band dispersion profile and optical emission profile for different values of strain and crystal orientations, Schrödinger equations for conduction and valence band are solved using finite difference method. To investigate the output P-I characteristics, the physical structure of the proposed QW laser is converted into Simulink model by using two-level rate equations. Then the rate equations are transformed to a 3rd-order state-space model in order to simulate the small-signal response of proposed laser structure. The numerical results estimated for the proposed QW Laser system demonstrate that the energy band dispersion profiles, momentum matrix elements, optical gain profile , output optical power response and frequency characteristics are strongly dependent on strain, crystal orientations and piezoelectric field. The internal electric field is shown to be zero near the crystal angle of 61°, 58°, 55° and 53° with 15%, 17%, 19% and 21% Indium composition because the sum of piezoelectric and spontaneous polarizations in the barrier is equal to that in the well. Valence band energy separation and transition momentum matrix elements are found to be higher at semipolar $(11\bar{2}2)$ orientation (growth angle θ=58.4° w.r.t z-axis) because of reduced distant band interaction and piezoelectric field induced quantum confined stark effect. For these reasons, higher optical gain of 4880 cm^{-1} is obtained in this crystal orientation for TE polarization. Due to opposite scenario, minimum optical gain of 3845 cm^{-1} is found in (0001) crystal orientation. The maximum emission wavelength (455nm) is evaluated in $(10\bar{1}0)$ orientation and minimum (438nm) in $(10\bar{1}2)$ orientation due to the maximum energy separations between conduction to heavy hole band in $(10\bar{1}0)$ orientation and minimum in $(10\bar{1}2)$ orientation. It is found that starting of optical gain is highly dependent on the injection carrier density in a particular crystal orientation. The carrier density required to start

gain is found to be higher in (0001) orientation and smaller in $(11\bar{2}2)$ orientation. Data extracted from above analysis are inserted into Simulink model to find P-I characteristics of proposed laser system. Maximum optical power of 4.35mW and minimum threshold current of 0.74mA are obtained in $(11\bar{2}2)$ oriented QW laser structure. Bode diagram is used to show frequency response in different crystal orientation for InGaN/GaN QW blue laser. Positive gain and phase margin is obtained from bode plot for each crystal oriented structure. From the magnitude (dB) response, electrical bandwidth has been calculated which shows that highest bandwidth of 5THz and lowest bandwidth of 0.76 THz is achieved for $(11\bar{2}2)$ and (0001) orientation. Since a large bandwidth corresponds to a small rise time, or fast response, it can be said that topmost speed of response for InGaN/GaN QW blue laser system can be found in semipolar $(11\bar{2}2)$ orientation.

The influence of piezoelectric field on the optical gain and peak emission wavelength is found to be significant for the proposed laser structure. The gain decreases $400cm^{-1}$ and emission wavelength shifts from 447.3nm to 443nm due to piezoelectric field in (0001) orientated compressively strained $In_{0.17}Ga_{0.83}N$/GaN QW structure. The shift in energy, peak gain and peak wavelength is found to be null in $(11\bar{2}2)$ and $(10\bar{1}0)$ orientation.

Comparison of Strain-dependent Optoelectronic Performance in $(11\bar{2}2)$, $(10\bar{1}2)$ and (0001) Crystal Orientation has been shown for 15%, 17%, 19% and 21% Indium composition in the well. The energy band separations from conduction band to heavy and light hole increases with increasing strain which leads to emission wavelength shift in shorter wavelength. The value of optical gain increases with strain as the energy band separations and magnitude of momentum matrix element for CB-HH transition are seen to be rising with strain. Emission wavelength shifts towards “Green” from “Blue” range with higher values of Indium composition and corresponding strain. Peak gain in TE direction are evaluated to be 5190 cm^{-1}, 4750 cm^{-1} and 3900 cm^{-1} for 21% In composition along $(11\bar{2}2)$, $(10\bar{1}2)$ and (0001) crystal orientation. From the injection carrier density-dependent optical gain characteristics it is found that higher gain is obtained for 21% In composition for any injection carrier density in every orientation. Maximum optical power, minimum threshold current and highest electrical bandwidth is also obtained for each crystal orientation when indium content in well layer is 21%.

6.2 Future Work

In present simulation, room temperature of 300K is considered. The work can be extended to find temperature-dependent optoelectronic performance along arbitrary-oriented QW structure and for different values of strain. This thesis estimates optical gain spectra using free-carrier gain model. To get a more realistic estimate for the emission wavelength, the bandgap renormalization that arises from the many-body effects can be included in future work by practicing Coulomb-hole self-energy and Hartree-Fock energy correction concept. Moreover, the potential level for electron and hole can be determined by self-consistent Schrödinger -Poisson's equations.

REFERENCES

[1] William T. Silfvast, Laser Fundamentals, Cambridge University Press, 1998.

[2] A. L. Schawlow and C. H. Townes, "Infrared and Optical Masers," Physical Review, vol.112, no.6, pp. 1940-1949, December 1958.

[3] Maimon, T.H., " Stimulated optical radiation in ruby", Nature, vol. 187, pp.493-494, 1960.

[4] A. Javan, W, B., Bennett, Jr., and D. R. Herriott, "Population Inversion and Continuous Optical Maser Oscillation in a Gas Discharge Containing a He-Ne Mixture", Phys. Rev. Letters, vol. 6, no.3, pp. 106-110, February 1961.

[5] L. F. Johnson, G. D. Boyd, K. Nassau, and R. R. Soden , "Continuous Operation of a Solid-State Optical Maser", Physical Review, vol.126, no.4, pp. 1406-1409, May 1962.

[6] R. N. Hall, G. E. Fenner, J. D. Kingsley, T. J. Soltys, and R. O. Carlson, "Coherent Light Emission From GaAs Junctions", Physical Review Letters, vol.9, no.9, pp. 366-368, November 1962.

[7] Pallab Batcharry, Semiconductor Optoelectronic Devices, Prentice Hall; second edition, 1996.

[8] J. P. van der Ziel, R. Dingle, R. C. Miller, W. Wiegmann, and W. A. Nordland, "Laser oscillation from quantum states in very thin GaAs-$Al_{0.2}Ga_{0.8}As$ multilayer structures," Appl.Phys. Lett., vol. 26, no. 8, pp. 463–465, Apr. 1975.

[9] J.D. Thomson, H.D. Summers, P.J. Hulyer, P.M. Smowton, and P. Blood, "Determination o f single-pass optical gain and internal loss using a multisection device. Applied Physics Letters, 1999. 75(17): p. 2527-2529.

[10] Z. Z. Chen, Z. X. Qin, Y. Z. Tong, X. D. Hu, T. J. Yu, Z. J. Yang, X. M. Ding, Z. H. Li, and G. Y. Zhang, Mater. Sci. Eng., B 100, 199 (1995).

[11] J.D. Thomson, H.D. Summers, P.J. Hulyer, P.M. Smowton, and P. Blood, "Determination of single-pass optical gain and internal loss using a multisection device", Applied Physics Letters, 1999. 75(17): p. 2527-2529.

[12] Hadis Morkoç, Handbook of Nitride Semiconductors and Devices: Materials Properties, Physics and Growth, Volume 1, John Wiley & Sons (2008)

[13] Ashraful Ghani Bhuiyan, Akihiro Hashimoto, and Akio Yamamoto, "Indium nitride (InN): A review on growth, characterization, and properties", J. Appl. Phys. 94, 2779 (2003).

[14] S. Nakamura and G. Fasol, The Blue Laser Diode, Springer, Berlin (1997).

[15] Yu Hongbo, L.K.Lee, Taeil Jung and P.C.Ku, "Photoluminescence study of semipolar InGaN/GaN multiple quantum wells grown by selective area epitaxy", Appl. Phys. Lett. 90, 141906 (2007).

[16] S. Nakamura, T. Mukai, and M. Senoh, "High-brightness InGaN/AlGaN doubleheterostructure blue-green-light-emitting diodes," J. Appl. Phys., vol. 76, no. 12, pp. 8189–8191, Dec. 1994.

[17] J. L. Weyher, H. Ashraf, and P. R. Hageman, Reduction of dislocation density in epitaxial GaN layers by overgrowth of defect-related etch pits, Appl. Phys. Lett. 95, 031913 (2009).

[18] M. Grundmann, The Physics of Semiconductors: An Introduction including Devices and Nanophysics (Springer, Berlin, 2006).

[19] J. Piprek, S. Nakamura, Physics of high-power InGaN/GaN lasers. IEE Proc. Optoelectron.149(4), 145–151 (2002).

[20] S. Bader, B. Hahn, H. Lugauer, A. Lell, A.Weimar,G.Brüderl, J.Baur, D. Eisert,M. Scheubeck,S. Heppel, A. Hangleiter, V. Härle, First european GaN-based violet laser diode. Physica Status Solidi A 180, 177–182 (2000).

[21] A. R. Stonas, P. Kozodoy, H. Marchand, P. Fini, S. P. DenBaars, U. K. Mishra, and E. L. Hu, Appl. Phys. Lett. 77, 2610 (2000).

[22] S.H.Park and S.L.Chuang, "Crystal-orientation effect on piezoelectric field and electronic properties of strained wurtzite semiconductors", PHYSICAL REVIEW B, vol.59, No. 7(1999).

[23] V. Avrutin, S. din A. Hafiz, F. Zhang, Ü. Özgür, H. Morkoç, and A. Matulionis, "InGaN light-emitting diodes: Efficiency-limiting processes at high injection," J. Vac. Sci. Technol. A, vol. 31, no. 5, p. 50809, Sep. 2013.

[24] Horino et al., "Growth of (1100) Oriented GaN on (1100) 6H-SiC by Metalorganic Vapor Phase Epitaxy", in Proc. of International Symposium on Blue Laser and Light Emitting Diodes, Chiba Univ., Japan, Mar. 5-7, 1996, pp. 530-533.

[25] J.A. Davidson, P. Dawson, T. Wang, T. Sugahara, J.W. Orton, and S. Sakai, Photoluminescence studies o f InGaN/GaN multi-quantum wells. Semicond. Sci. Technol., 2000. 15(6): p. 497-505.

[26] T. Takeuchi, C. Wetzel, S. Yamaguchi, H. Sakai, H. Amano, I. Akasaki, Y. Kaneko, S. Nakagawa, Y. Yamaoka, and N. Yamada, Determination of piezoelectric fields in strained

GalnN quantum wells using the quantum confined Stark effect. Applied Physics Letters, 1998. 73(12): p. 1691-1693.

[27] Yun Zhang, “Development of III-Nitride Bipolar Devices: Avalanche Photodiodes, Laser Diodes, and Double-Heterojunction Bipolar Transistors”, PhD Dissertion, Georgia Institute of Technology, 2011.

[28] J. W. Raring, M. C. Schmidt, C. Poblenz, B. Li, Y.-C. Chang, M. J. Mondry, Y.-D. Lin, M. R. Krames, R. Craig, J. S. Speck, S. P. DenBaars, S. Nakamura, High-performance blue and green laser diodes based on nonpolar/semipolar bulk GaN substrates. Proc. SPIE 7939, 79390Y (2011).

[29] J. E. Northrup, GaN and InGaN $(11\bar{2}2)$ surfaces: Group-III adlayers and In incorporation. Appl. Phys. Lett. 95,133107 (2009).

[30] T. Ohtoshi, T. Kuroda, A. Niwa, and S. Tsuji, “Dependence of optical gain on crystal orientation in surface-emitting lasers with strained quantum wells” , Applied Physics Letters 65, 1886 (1994).

[31] M.M.Hasan, M.R.Islam, K. Teramoto, “Crystallographic orientation-dependent optical properties of GaInSb mid-infrared quantum well laser”, Optik - Int. J. Light Electron Opt., Elsevier (2011).

[32] Yae Okuno, “Investigation on direct bonding of III–V semiconductor wafers with lattice mismatch and orientation mismatch”, Applied Physics Letters 68, 2855 (1996).

[33] M.S.Sarker, M.M.Islam, M.M.Hasan, and M.R.Islam, “Crystal orientation dependent performance of cubic InGaN QW blue-violet laser” in Proc. of ICCIT'18, 2015, pp. 167-171.

[34] H.Okumura,K.Ohta, G.Feuilleta, K.Balakrishnan, S.Chichibu, H.Hamaguchi, P.Hacke, S.Yoshida, “Growth and characterization of cubic GaN”, Journal of Crystal Growth, Volume 178, Issues 1–2, 2 June 1997.

[35] https://en.wikipedia.org/wiki/Laser_diode

[36] John M. Senior, “Optical Fiber Communications: Principles and Practice”, Prentice Hall

[37] Larry A. Coldren, Scott W. Corzine, Milan L. Mashanovitch, Diode Lasers and Photonic Integrated Circuits, 2nd Edition, Wiley

[38] Safa O. Kasap, Principles of Electronic Materials and Devices, McGraw-Hill Education

[39] Iestyn A. Pope, “The Characterisation of InGaN/GaN Quantum Well Light Emitting Diodes”, PhD Thesis, Department of Physics and Astronomy, Cardiff University

[40] S.M.Sze, “ Physics of Semiconductor Devices”, John. Wiley, 1984

[41] Rainer Michalzik, Fundamentals, Technology and Applications of Edge-Emitting Lasers, Springer, Berlin, 1994.

[42] William H. Hayt, Jr. . John A. Buck, Engineering Electromagnetics, McGraw-Hill Series

[43] Matsuoka, T., Tanaka, H., Sasaki, T. and Katsui, K., Proceedings of the 16th International Symposium on GaAs and Related Compounds, 1989, Karuizawa, Institute of Physics Conference Series,vol. 106, Institute of Physics, Bristol,p. 141.

[44] Yoshimoto, N., Matsuoka, T., Sasaki, T. and Katsui, A. (1991) Applied Physics Letters, 59, 2251.

[45] Matsuoka, T., Yoshimoto, N., Sasaki, T. and Katsui, A. (1992) Journal of Electronic Materials, 21, 157.

[46] Shimizu, M., Hiramatsu, K. and Sawaki, N. (1994) Journal of Crystal Growth, 145, 209.

[47] S. Nakamura, GaN Growth Using GaN Buffer Layer, Jpn. J. Appl. Phys. 30, L1705 (1991).

[48] T. Zhu, Non-polar GaN epilayers and heterostructures for photonic applications, PhD thesis, EPFL, n. 4563, 2009.

[49] J. L. Weyher, H. Ashraf, and P. R. Hageman, Reduction of dislocation density in epitaxial GaN layers by overgrowth of defect-related etch pits, Appl. Phys. Lett. 95, 031913 (2009).

[50] M. Grundmann, The Physics of Semiconductors: An Introduction Including Devices and Nanophysics (Springer, Berlin, 2006).

[51] A. Dussaigne, B. Damilano, J. Brault, J. Massies, E. Feltin, and N. Grandjean, High doping level in Mg-doped GaN layers grown at low temperature, J. Appl. Phys. 103, 013110 (2008).

[52] H. Amano, T. Asahi, and I. Akasaki, Stimulated Emission Near Ultraviolet at Room Temperature from a GaN Film Grown on Sapphire by MOVPE Using an AlN Buffer Layer, Jpn. J. Appl. Phys. 29, L205 (1990).

[53] B. Gil and O. Briot, Internal structure and oscillator strengths of excitons in strained GaN, Phys. Rev. B 55, 2530 (1997).

[54] J. Levrat, Physics of Polariton Condensates in GaN-based Planar Microcavities, PhD thesis, EPFL, n. 5449, 2012.

[55] http://mcaroba.dyndns.org/wiki/index.php/Group-III_nitrides

[56] O. Ambacher, J. Majewski, C. Miskys, A. Link, M. Hermann, M. Eickhoff, M. Stutzmann, F. Bernardini, V. Fiorentini, V. Tilak, B. Schaff, and L. F. Eastman, Pyroelectric properties

of Al(In)GaN/GaN hetero- and quantum well structures, J. Phys.: Condens. Matter 14, 3399 (2002).

[57] T. Whitaker, SUVOS pushes UV LEDs and lasers to shorter wavelengths, in Compound Semiconductor. 2004.

[58] J. Zhang, Crack-free thick AlGaN grown on sapphire using AlN/AlGaN superlattices for strain management. Applied Physics Letters, 2002. 80(19): p. 3542-3543.

[59] Jiang, H., Zhao, G.Y., Ishikawa, H., Egawa, T., Jimbo, T. and Umeno, M.(2001) Journal of Applied Physics, 89, 1046.

[60] Wright, A.F., Leung, K. and van Schilfgaarde, M. (2001) Effects of biaxial strain and chemical ordering on the band gap of InGaN. Applied Physics Letters, 78 (2), 189–191.

[61] Shan, W., Walukiewicz, W., Haller, E.E., Little, B.D., Song, J.J., McCluskey, M.D., Johnson, N.M., Feng, Z.C., Schurman, M. and Stall, R.A. (1998) Journal of Applied Physics, 84, 4452.

[62] Y. P. Varshni, Temperature dependence of the energy gap in semiconductors, Physica 34, 149 (1967).

[63] T. Kawashima, H. Yoshikawa, S. Adachi, S. Fuke, and K. Ohtsuka, Optical properties of hexagonal GaN, J. Appl. Phys. 82, 3528 (1997).

[64] E. Rosencher and B. Vinter, Optoelectronics (Cambridge University Press, Cambridge, 2002).

[65] B. E. A. Saleh and M. C. Teich, Fundamentals of photonics (Wiley-Interscience, Hoboken, N.J., 2007).

[66] M. J. Bergmann and H. C. Casey, Optical-field calculations for lossy multiple-layer AlGaN/InGaN laser diodes, J. Appl. Phys. 84, 1196 (1998).

[67] M. Leroux, N. Grandjean, M. Laügt, J. Massies, B. Gil, P. Lefebvre, and P. Bigenwald, Quantum confined Stark effect due to built-in internal polarization fields in (Al,Ga)N/GaN quantum wells, Phys. Rev. B 58, R13371 (1998).

[68] C. Wetzel, M. Zhu, J. Senawiratne, T. Detchprohm, P. Persans, L. Liu, E. Preble, and D. Hanser, Light-emitting diode development on polar and non-polar GaN substrates, J. Cryst. Growth 310, 3987 (2008).

[69] D. A. B. Miller, D. S. Chemla, T. C. Damen, A. C. Gossard, W. Wiegmann, T. H. Wood, and C. A. Burrus, Band-Edge Electroabsorption in Quantum Well Structures: The Quantum-Confined Stark Effect, Phys. Rev. Lett. 53, 2173 (1984).

[70] D. A. B. Miller, D. S. Chemla, T. C. Damen, A. C. Gossard, W. Wiegmann, T. H. Wood, and C. A. Burrus, Electric field dependence of optical absorption near the band gap of quantum-well structures, Phys. Rev. B 32, 1043 (1985).

[71] S. F. Chichibu, A. C. Abare, M. S. Minsky, S. Keller, S. B. Fleischer, J. E. Bowers, E. Hu, U. K. Mishra, L. A. Coldren, S. P. DenBaars, and T. Sota, Effective band gap inhomogeneity and piezoelectric field in InGaN/GaN multiquantum well structures, Appl. Phys. Lett. 73, 2006 (1998).

[72] A. E. Siegman, Lasers (University Science Books, Oxford, 1986).

[73] S. M. Sze and K. K. Ng, Physics of Semiconductor Devices (John Wiley & Sons, Hoboken, 2006).

[74] G. Y. Zhang, Y. Z. Tong, Z. J. Yang, S. X. Jin, J. Li, and Z. Z. Gan, Relationship of background carrier concentration and defects in GaN grown by metalorganic vapor phase epitaxy, Appl. Phys. Lett. 71, 3376 (1997).

[75] J. Neugebauer and C. G. Van de Walle, Gallium vacancies and the yellow luminescence in GaN, Appl. Phys. Lett. 69, 503 (1996).

[76] W. Götz, J. Walker, L. Romano, N. Johnson, and R. Molnar, Thickness Dependence of Electronic Properties of GaN Epi-layers, Mater. Res. Soc. Symp. Proc. 449, 525 (1996).

[77] S. Nakamura, T. Mukai, and M. Senoh, Si-Doped InGaN Films Grown on GaN Films, Jpn. J. Appl. Phys. 32, L16 (1993).

[78] C. Yuan, T. Salagaj, A. Gurary, A. G. Thompson, W. Kroll, R. A. Stall, C.-Y. Hwang, M. Schurman, Y. Li, W. E. Mayo, Y. Lu, S. Krishnankutty, I. K. Shmagin, R. M. Kolbas, and S. J. Pearton, Investigation of n- and p-type doping of GaN during epitaxial growth in a mass production scale multiwafer-rotating-disk reactor, J. Vac. Sci. Technol. B 13, 2075 (1995).

[79] S. Nakamura, M. Senoh, S.-i. Nagahama, N. Iwasa, T. Yamada, T. Matsushita, Y. Sugimoto, and H. Kiyoku, Room-temperature continuous-wave operation of InGaN multi-quantum-well structure laser diodes with a lifetime of 27 hours, Appl. Phys. Lett. 70, 1417 (1997).

[80] W. Götz, R. Kern, C. Chen, H. Liu, D. Steigerwald, and R. Fletcher, Hall-effect characterization of III–V nitride semiconductors for high efficiency light emitting diodes, Mater. Sci. Eng., B 59, 211 (1999).

[81] T. Schmidt, M. Siebert, J. I. Flege, S. Figge, S. Gangopadhyay, A. Pretorius, T.-L. Lee, J. Zegenhagen, L. Gregoratti, A. Barinov, A. Rosenauer, D. Hommel, and J. Falta, Mg and Si dopant incorporation and segregation in GaN, Phys. Status Solidi (b) 248, 1810 (2011).

[82] Morteza Monavarian, "Beyond conventional c-plane GaN-based light emitting diodes: A systematic exploration of LEDs on semi-polar orientations" PhD Thesis, Virginia Commonwealth University.

[83] V. Z. Tronciu, Minoru Yamada and R. A. Abram, Analysis of the dynamics of a blue-violet $In_xGa_{1-x}N$ laser with a saturable absorber, PHYSICAL REVIEW E 70, 026604 (2004)

[84] Yae Okuno et. al., "Direct Wafer Bonding of III–V Compound Semiconductors for Free-Material and Free-Orientation Integration", IEEE Journal of quantum electronics, vol. 33, no. 6, June 1997

[85] S. L. Chuang and C. S. Chang, Phys. Rev. B 54, 2491 (1996).

[86] S. L. Chuang, Physics of Optoelectronic Devices ~Wiley, New York, 1995, Chap. 4.

[87] A. Niwa, T. Ohtoshi, T. Kuroda, Orientation dependence of optical properties in long wavelength strained quantum-well lasers, IEEE J. Selected Top. Quantum Electron. 1 (1995) 211–217.

[88] Morteza Monavarian, "Beyond conventional c-plane GaN-based light emitting diodes: A systematic exploration of LEDs on semi-polar orientations" PhD Thesis, Virginia Commonwealth University.

[89] S. Park, S. Chuang, Crystal-orientation effects on the piezoelectric field and electronic properties of strained wurtzite semiconductors. Phys. Rev. B 59(7), 4725–4737 (1999)

[90] T. Ohtoshi, T. Kuroda, A. Niwa, S. Tsuji, Dependence of optical gain on crystal orientation in surface-emitting lasers with strained quantum wells, Appl. Phys. Lett. 65 (1994) 1886–1889.

[91] O. Ambacher, J. Majewski, C. Miskys, A. Link, M. Hermann, M. Eickhoff, M. Stutzmann, F. Bernardini, V. Fiorentini, V. Tilak, B. Schaff, L. F. Eastman, Pyroelectric properties of Al(In)GaN/GaN hetero- and quantum well structures. J. Phys.: Condens. Matter 14, 3399 3434 (2002)

[92] W. Scheibenzuber, U. Schwarz, R.Veprek,B.Witzigmann, A. Hangleiter, Calculation of optical eigenmodes and gain in semipolar and nonpolar InGaN/GaN laser diodes. Phys. Rev. B 80(11), 115320 (2009)

[93] S. Shokhovets, R. Goldhahn, G. Gobsch, S. Piekh, R. Lantier, A. Rizzi, V. Lebedev,W. Richter, Determination of the anisotropic dielectric function for wurtzite AlN and GaN by spectroscopic ellipsometry. J Appl. Phys. 94(1), 307 (2003)

[94] G. Bastard, E.E. Mendez, L.L. Chang, and L. Esaki, “Variational calculations on quantum well in an electric field”, Physical Review B, vol. 28, no.6, September 1983

[95] Y.K. KUO, J.R. CHEN, M.L. CHEN, B. T. LIOU, “ Numerical study on strained InGaAsP/InGaP quantum wells for 850nm vertical cavity surface emitting lasers,” Applied Physics B, DOI:10.1007/s00340-006-2567-5, 2007

[96] M.M.Hasan, M.R.Islam, K. Teramoto, “Crystallographic orientationdependent optical properties of GaInSb mid-infrared quantum well laser”, Optik - Int. J. Light Electron Opt., Elsevier (2011).

[97] Pablo V. Mena and Thomas A. DeTemple, “Rate-Equation-Based Laser Models with a Single Solution Regime”, Journal of Lightwave Technology, vol. 15, no. 4, April 1997

[98] Piprek, J., sink, R.k., Hansen, M.A., Bowers, J.E., and Denbaars, S.P.: ‘Simulation and optimization of 420 nm InGaN=GaN laser diodes’, Proc. SPIE-Int. Soc. Opt. Eng., 2000, 3944, pp. 28–39

[99] J. Piprek and S. Nakamura, “Physics of high-power InGaN-GaN lasers”, IEE Proc.-Optoelectron., Vol. 149, No. 4, August 2002

[100] W. H. Fan et al., “Carrier capture times in InGaN/GaN multiple quantum wells”, phys. stat. sol. (b) 240, No. 2, 364– 367 (2003) / DOI 10.1002/pssb.200303389

[101] J. R. Lang, N. G. Young, R. M. Farrell, Y.-R. Wu, and J. S. Speck, “Carrier escape mechanism dependence on barrier thickness and temperature in InGaN quantum well solar cells” Appl. Phys. Lett. 101, 181105 (2012); doi: 10.1063/1.4765068

[102] Toby Schaer, Robert Rusnov, Stephen Eagle, Jay Jastrebski, Steven Albanese and Xavier Fernando, “A Dynamic Simulation Model for Semiconductor Laser Diodes”, Canadian Conference on Electrical and Computer Engineering, DOI: 10.1109/CCECE.2003.1226399 (2003).